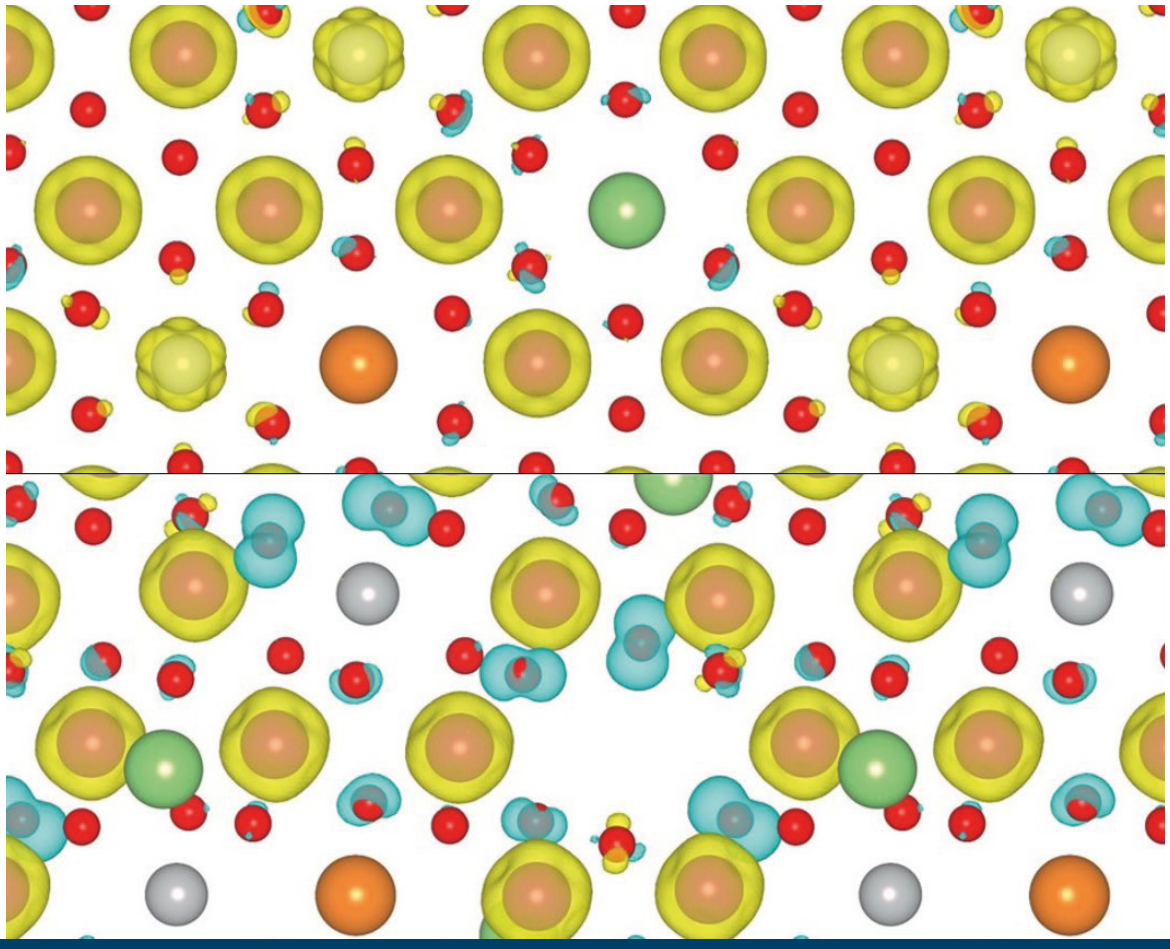

First principles study of the effect of substitution\doping on the performance of layered oxide cathode materials for secondary batteries

Najma Yaqoob

Energie & Umwelt / Energy & Environment
Band / Volume 681
ISBN 978-3-95806-864-3

UNIVERSITY OF TWENTE.

JÜLICH Forschungszentrum

Schriften des Forschungszentrums Jülich
Reihe Energie & Umwelt / Energy & Environment Band / Volume 681

Forschungszentrum Jülich GmbH
Institute of Energy Materials and Devices (IMD)
Werkstoffsynthese und Herstellungsverfahren (IMD-2)

First principles study of the effect of substitution\doping on the performance of layered oxide cathode materials for secondary batteries

Najma Yaqoob

Schriften des Forschungszentrums Jülich
Reihe Energie & Umwelt / Energy & Environment Band / Volume 681

ISSN 1866-1793 ISBN 978-3-95806-864-3

Bibliografische Information der Deutschen Nationalbibliothek.
Die Deutsche Nationalbibliothek verzeichnet diese Publikation in der
Deutschen Nationalbibliografie; detaillierte Bibliografische Daten
sind im Internet über http://dnb.d-nb.de abrufbar.

UNIVERSITY
OF TWENTE.

Herausgeber und Vertrieb:	Forschungszentrum Jülich GmbH Zentralbibliothek, Verlag 52425 Jülich Tel.: +49 2461 61-5368 Fax: +49 2461 61-6103 zb-publikation@fz-juelich.de www.fz-juelich.de/zb
Umschlaggestaltung:	Grafische Medien, Forschungszentrum Jülich GmbH
Druck:	Grafische Medien, Forschungszentrum Jülich GmbH
Copyright:	Forschungszentrum Jülich 2025

Schriften des Forschungszentrums Jülich
Reihe Energie & Umwelt / Energy & Environment, Band / Volume 681

(Diss. University of Twente, 2025)

ISSN 1866-1793
ISBN 978-3-95806-864-3

ISBN (print): 978-90-365-6965-1 (University of Twente)
ISBN (digital): 978-90-365-6966-8 (University of Twente)

Vollständig frei verfügbar über das Publikationsportal des Forschungszentrums Jülich (JuSER)
unter www.fz-juelich.de/zb/openaccess.

Graduation Committee:

Chair / secretary:	prof. dr. J.J.L.M. Cornelissen
Promotor:	prof.dr.ir. M. Huijben Universiteit Twente, TNW, Inorganic Materials Science
Co-promotor:	prof.dr. P. Kaghazchi Universiteit Twente, TNW, Inorganic Materials Science
Committee Members:	prof. dr. S. Dsoke University of Freiburg
	prof. dr. ir. M. Wagemaker TU Delft
	prof.dr. L. Leppert Universiteit Twente, TNW, Computational Chemical Physics
	prof.dr.ir. A. Brinkman Universiteit Twente, TNW, Interfaces and Correlated Electron Systems
	prof.dr.ir. J.E. ten Elshof Universiteit Twente, TNW, Inorganic Materials Science

Contents

1

Introduction

1.1 Introduction and Motivation

Energy-storage devices play an important role in the future's energy supply[1]. A battery is one of the most important energy storage devices, which can convert chemical energy into electrical energy[2]. There are two types of batteries: (i) Primary or non-rechargeable batteries and (ii) secondary or rechargeable batteries[3]. Primary batteries or alkaline batteries are designed in such a way that they can be used once and cannot be reused again. In batteries, normally, chemical reactions generate electricity, but in primary batteries, once the reactants vanish, they stop producing electricity. In general, the electrochemical reaction going on in the cell is electrochemically irreversible. It also provides high internal resistance with low cell voltages, which limits its ability to deliver high current. Therefore, they can be used only in light-load devices such as toys, portable radios, alarm clocks, and flashlights[4].

Secondary batteries, such as lithium (Li) ion and sodium (Na) ion batteries, refer to batteries that are rechargeable and are more economical than primary batteries[5]. In secondary batteries, the electrochemical reaction is reversible, and internal resistance is comparatively lower than in primary batteries[4]. The advantages of secondary batteries as it provides higher energy and power density with large cell voltage and higher current load makes them usable in small and large-scale applications, for example, in portable electronic devices[6−7] and electric vehicles respectively[8].

A battery has four main parts i.e. (i) cathode (ii) anode (iii) separator and (iv) electrolytes. Electrolytes are responsible for the charging and discharging process of a battery by transferring ions from the negative to the positive electrode of the battery and vice versa[9]. A separator keeps the positive and negative electrodes separated

in order to avoid internal short circuit, while the current collector maintains the flow of electrons between electrodes and external circuit. During charging, electrons are transferred from the positive (cathode) to the negative (anode) terminal of the battery and return back during the discharging process through an external circuit[10]. Therefore, the cathode is oxidized and the anode is reduced during charging and vice versa upon discharging to make a charge balance of the system.

With the increasing problem of climate change, the development of rechargeable and sustainable energy storage devices such as lithium-ion batteries (LIBs) and sodium-ion batteries (SIBs) are gaining extensive attention. LIBs have attracted significant attention because of their applications in electric vehicles and many kinds of portable electronic devices, such as cell phones. However, SIBs are gaining importance as promising alternatives to LIBs for grid and large-scale energy storage applications due to the high earth abundance of the elements used in SIBs, such as Na and Mn. However, such batteries still need more research and improvement to satisfy the market requirements for low cost and high-rate performance.

Moreover, it is important to enhance environmental safety and save our planet by decreasing greenhouse gas emissions[11] with the replacement of fossil fuels by rechargeable batteries. The improvement in the following parameters is highly desirable for the renewable energy generation[12–14]: power density[15–17], energy density[18–19], safety[20], cycling stability[21–22] and cost[23]. To improve the performance of secondary batteries, LIBs and SIBs need to be first discussed in detail:

1.1.1 Lithium-ion Batteries

Rechargeable Li-ion batteries work on the principle of a rocking chair that was first proposed by Armand et al. in the 1970s.[24]. This process allows back and forth movement of Li ions between the cathode and the anode during the charging and discharging process. Most of battery cells commonly utilize graphite or carbon-based anodes. However, the cathode is usually a Li metal oxide such as Lithium cobalt oxide ($LiCoO_2$) that was first proposed by Mizushima and Goodenough et al.[25], and later commercialized by Sony in 1991[26]. Since that time, these materials

have been extensively used in portable electronics devices.

The following electrode reactions that occur in a LIBs consists of graphite (anode) and a layered CoO_2 as cathode materials are:

$$\text{Cathode: } \mathrm{Li(Co)O_2} \underset{\text{discharge}}{\overset{\text{charge}}{\rightleftharpoons}} \mathrm{Li_{1-x}(Co')O_2} + x\mathrm{Li^+} + x\mathrm{e^-}$$

$$\text{Anode: } n\mathrm{C} + x\mathrm{Li^+} + xe^- \underset{\text{discharge}}{\overset{\text{charge}}{\rightleftharpoons}} \mathrm{Li_xC_n}$$

$$\text{Overall: } n\mathrm{C} + \mathrm{Li(Co)O_2} \underset{\text{discharge}}{\overset{\text{charge}}{\rightleftharpoons}} \mathrm{Li_xC_n} + \mathrm{Li_{1-x}(Co')O_2}$$

Where Co′ represents the variation in the oxidation/charge state of Co cations during the charging process.

In addition to the reaction mentioned above, there are also some other possible

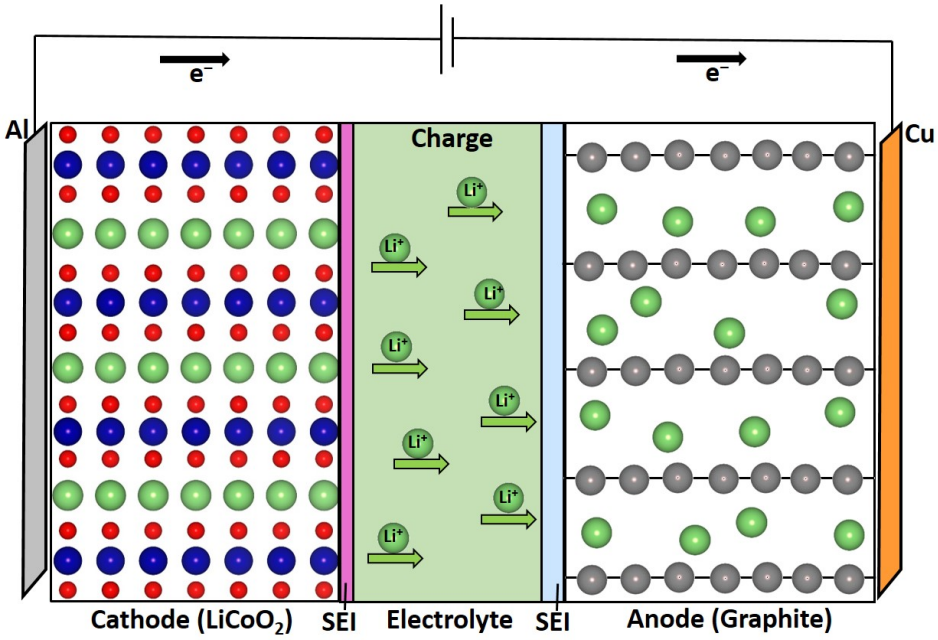

Figure 1.1: Schematic of commercially used LIBs during charging. Li, Co, O and C are in green, blue, red and grey respectively. SIBs also work following a similar mechanism.

undesirable side reactions that can occur during the charging/discharging process. For example, reaction between the electrolyte and the surface of the electrodes forms a new layer which is called the solid electrolyte interface (SEI) layer. However, the formation of SEI layer is not reversible and hence leads to large capacity fading during cycling[27].

1.1.2 Sodium-ion Batteries

Sodium-ion batteries have attracted great attention because of their potential as inexpensive and large-scale applications in next-generation energy storage technologies[28−29]. Similar to LIBs, Sodium-ion batteries also work on the principle of rocking chair, which shows a similar (de) intercalation mechanism to LIBs. SIBs had been originally studied side-by-side with LIBs in the late 1970s, however, the results were not very interesting at that time because of the lower energy density of SIBs than that of LIBs, therefore research was largely neglected for a few decades[30]. This changed from the mid-2010s on and nowadays SIBs have been gaining much attention because of their potential application in large scale energy storage[31−33].

SIBs offer the further hope for decreasing supply risks, price and improving environmental friendliness by using abundant elements such as Na, Mn, or Fe for the cathode materials[34−36]. Moreover, a great advantage of SIBs is to use abundant and environmentally friendly anode materials such as hard carbon, which can be obtained from biomass[37]. For the positive electrode side, layered transition metal (TM) oxides attracted much attention[38−39]. Layered TM oxide is maybe among the most promising cathode materials because of its low toxicity, high energy density, reasonable potential and good cycling stability[40−43]. Although the intercalation chemistry of Na and Li ions is very similar, battery characteristics of both ions can be quite different. For example, it has been found that some electrochemically inactive transition metals toward lithium ions can be an active material (involved in redox reaction) for sodium ions[44] since the size difference between the two alkali ions makes each ion have a different stability within the same structure[45]. Hence,

detailed studies on the potential cathode materials for SIBs are necessary.

Layered sodium TM oxides as cathode materials are ideal candidates and being widely studied[46–49] because they can have tunable compositions for a flexible design of new cathode materials. They potentially can provide sufficient capacity and the electrochemical performance can be easily tailored by the introduction of different dopant elements into the host structures. However, the low energy density as compared to LIBs urgently requires improvement for use in large-scale applications. Layered sodium TM oxides are crystallized into P and O structures depending on the Na-ions sitting at Prismatic and Octahedral sites respectively[50].

P2 and O3 materials are two main widely studied structures. The number 2 and 3 represents the number of TMO_2 layer per unit cell[51–53] with oxygen stacking in *ABABAB* and *ABCABC* in P2 and O3, respectively[54] as depicted in Figure 1.2. Generally, in O3 type of materials, Na-ions, due to their large ionic radius, when they are removed from the alkaline metal layer during desodiation (charging), they undergo multiple phase transitions such as O3-P3-O3′-O1, resulting in possible capacity loss[55]. However, P2-type materials offer higher capacity retention and better rate performance than O3-phase[56–59]. P2-type materials can also undergo phase transitions from P2 to O2[60–62] and from P2 to OP4[63–64] during charging but they experience less phase transitions than O3. Therefore, in our work, the main focus is to study P2-type layered sodium TM oxides cathodes, i.e. P2-Na_xMnO_2 for SIBs.

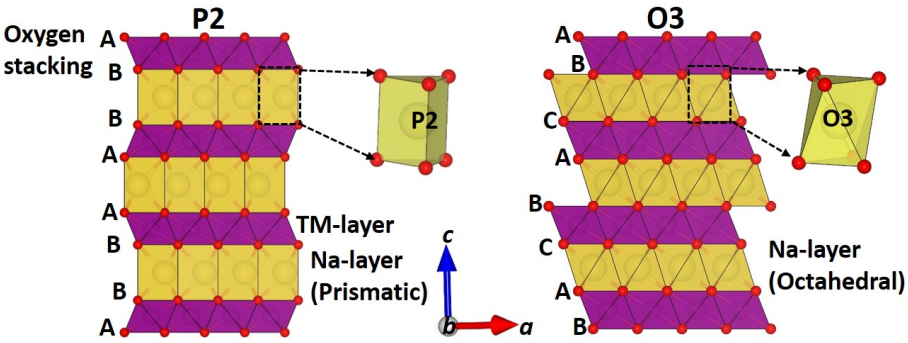

Figure 1.2: Schematic of P2 and O3 structures of Na_xMnO_2 for Sodium ion batteries.

However, layered oxide cathode materials still suffer from large lattice parameter changes and/or cation migration, which lead to mechanical cracking and/or structural instability and large capacity fade during cycling. A key factor underlying these issues is the occurrence of phase transitions during the charging/discharging process. These phase transitions involve changes in the atomistic structure, which result in lattice parameter variation, particularly along the interlayer (*c*-axis) direction. Such lattice distortions, generate significant mechanical stresses within the material during charge/discharge. These stresses may lead to microcracking, particle fracture, and ultimately, structural degradation.

Understanding the fundamental cause behind these structural changes (i.e. phase transition and/or lattice parameter), electronic changes such as variations in electron distribution and oxidation states associated with the redox mechanism and mechanical failure at the atomistic scale are important for improving the capacity of layered oxide cathode materials.

Moreover, variation in lattice parameters, particularly along the *c*-axis, undergoes significant changes during the charge/discharge process. The lattice parameter *a* decreases due to changes in the oxidation state, while the *c*-axis usually increases and then decreases with de-intercalation of alkali ions. A significant decrease in the *c*-axis due to a phase transition can lead to substantial structural instability. This significant anisotropic lattice parameters change, which is even more dramatic for Na-based layered oxides, with phase transition between P and O phases, directly influences the capacity and electrochemical performance of layered oxide cathode materials.

Electronic structure calculations provide insight into the electronic changes associated with the redox mechanism, revealing how electrons are transferred and how the oxidation states of the active materials change during charge-compensating cycling. Redox mechanism is one of the most important parameters which control the capacity and stability of cathode materials. Because redox reactions can trigger Jahn–Teller distortions (a type of atomic distortion and/or oxygen evolution), which further destabilize the structure.

The study of mechanical properties and stress-strain behaviour is an other important parameter that indicates how cathode materials respond to mechanical strain/stress that arises due to delithiation/lithiation and desodiation/sodiation. It also reveals the ability of the cathode to withstand repeated volume change (due to anisotropic variation in lattice parameters) without formation of cracks. Therefore, it is very important to compute these two quantities to find the origin behind the microcracking of layered oxide cathodes for LIBs.

Therefore, a comprehensive study that combines analysis of lattice changes, phase transitions, redox mechanisms and mechanical properties during charging/discharging is essential to fully understand the performance limitations and degradation effects of layered oxide cathodes. This understanding will guide the rational design and engineering of improved layered oxide cathode materials that are both stable and high-performing and cost-effective energy storage materials.

Computational science plays a important role in examining and gaining insights into the atomistic and electronic characteristics of layered oxide cathode materials.

This thesis employs a combination of computational approaches, such as Coulomb energy analysis, density functional theory (DFT), and ab initio molecular dynamics simulations (AIMD), to investigate changes in lattice parameters, electronic structure, charge transfer in P2-Na_xMnO_2 and mechanical stability of $LiCoO_2$. Specifically, the study focuses on the evolution of lattice dimensions and phase transitions in P2-Na_xMnO_2 during the de(sodiation) process. We also explored doping (adding small amounts of cation substitutions such as Li, Mg, Co and Ni) to stabilize the structure and enhance performance.

1.1.3 Computational approach and methods

Coulomb energy analysis: Determining the arrangement of defects (e.g., dopants or vacancies) in a crystal is challenging due to the large number of possible atomic configurations. In this thesis, the supercell program is used to explore these configurations in layered oxide cathode materials by evaluating their electrostatic interactions. The program employs Ewald summation, which provides an efficient and

accurate method for calculating the Coulomb energy in the crystal. Coulomb energy works as a brute-force calculation method, which solves a problem by systematically checking all possible solutions until the correct one is found. For example, to determine the distribution of 24 Na ions among 36 Na sites $\frac{36!}{24!12!}$ = 1251677700 possible structures in $Na_{0.67}[Li_{0.22}Mn_{0.78}]O_2$ is computationally demanding using DFT. Therefore, we first performed a preliminary screening using Coulomb energy and then selected a few of the lowest-energy structures for further DFT calculations.

Coulomb energy analysis[65−66] considers only classical electrostatic interactions, treating atoms as point charges, ignoring quantum effects and lattice relaxation. As a result, the lowest Coulomb-energy configurations may not always correspond to the true lowest-energy structures, so full DFT calculations are necessary to accurately determine the ground-state structure and other properties of materials.

Density functional theory (DFT): It has been widely used due to its balance of computational efficiency and accuracy in handling many-electron systems, since the electron density depends only on three spatial coordinates. In DFT, the electron density $\rho(r)$ is used as the central variable, rather than the many-body wavefunction, which significantly reduces the computational cost.

Hohenberg and Kohn[67] demonstrated that having the ground-state electron density, $\rho(r)$, is sufficient to determine all ground-state properties of a system.

In the first HK theorem, electron density uniquely determines the external potential (υext) to a constant. According to this Theorem, the total energy is a unique functional of the electron density.

Theorem II states that this functional achieves its minimum value if and only if the electron density is the true ground-state density.

Although the density functional theory (DFT) formulated by Hohenberg and Kohn is exact for describing the ground-state properties of any electronic system, it does not offer a practical way to perform calculations. Kohn and Sham addressed this limitation in 1965[68] by employing the variational principle of DFT to derive single-particle Schrödinger equations. They constructed a non-interacting system with the

same ground state density as the original interacting system.

However, the exact exchange–correlation (XC) functional in Kohn-sham DFT, which contains all the complex many-body effects, is unknown. As a result, Kohn–Sham DFT cannot directly yield exact solutions without employing approximations for this functional. The simplest and most widely used XC approximation is the Local Density Approximation (LDA)[69], which assumes that the exchange–correlation energy at each point depends only on the local electron density, but it is only valid for homogeneous electron gas.

The Generalized Gradient Approximation (GGA)[70] improves upon LDA by also including the local gradient of the density, allowing for better accuracy in systems. The GGA functional is valid for both homogeneous and non-homogeneous systems. We used the GGA approximation in this thesis to compute geometry optimization, atomistic structure, and lattice parameter prediction, as it is well known for layered oxide cathode materials. To further correct for the self-interaction error and to better describe localized electron effects (particularly in transition metal oxides and strongly correlated systems), the GGA+U[71] method introduces an on-site Coulomb interaction term U. However, choise of U-value is system dependent and small variations in U-value can change the results of layered oxide cathode materials.

A more advanced approach, the HSE06 hybrid functional[72], mixes a fraction of exact non-local Hartree–Fock exchange with the GGA exchange–correlation energy, significantly improving the description of electronic properties and structural properties in a wide range of materials in particular for transition metal oxides which are the studied materials in this thesis.

However, DFT only focuses on determining the ground-state properties of materials at 0 K, identifying their lowest-energy configurations under static conditions. DFT optimization can trap in local minima near the initial atomic configuration, limiting its ability to capture realistic ionic movements and lattice relaxations. To overcome this limitation and better represent temperature-dependent processes, ab initio molecular dynamics (AIMD) simulations are used, as they allow atoms to move dynamically

at finite temperatures and explore a wider range of the energy landscape beyond the static ground-state description.

Ab Initio Molecular Dynamics (AIMD) simulations: It is generally important to study a system under realistic conditions, that is a finite temperatures and/or pressure. For this purpose, a class of simulations can be employed in which the evolution of a system can be tracked in time. These classes of simulations are usually referred to as molecular dynamics (MD) simulations[73–74]. MD simulations allow for prediction of the time evolution of systems consisting of interacting particles by numerically solving the classical equations of motions.

In particular, to account for finite-temperature dynamics and possible migration of ions like Li and Mg from TM to Na-sites, ab initio molecular dynamics (AIMD) simulations were conducted. In AIMD, atomic nuclei are propagated via Newtonian dynamics, with forces computed on-the-fly from DFT within the Born–Oppenheimer approximation. This allows monitoring of thermal fluctuations, Li diffusion pathways, and structural stability under operationally relevant conditions.

AIMD simulations can be performed under different statistical ensembles using thermostats and/or barostats to control temperature and/or pressure. In the NVT ensemble[75] (canonical ensemble), the number of particles (N), volume (V), and temperature (T) are kept constant—commonly maintained via a thermostat such as the Nosé–Hoover or Langevin method. This setup is ideal for studying temperature-dependent structural and dynamical properties.

In contrast, the NPT ensemble (isothermal–isobaric ensemble)[76] allows both temperature and pressure to remain constant, using combined thermostat–barostat algorithms (e.g., Nosé–Hoover or Parrinello–Rahman)[77–78] to enable the system volume to fluctuate. This ensemble is especially useful for simulating realistic operating conditions and assessing structural stability under varying pressure.

Limitations of AIMD include high computational cost, which restricts simulations to modest supercell sizes (tens to hundreds of atoms) and short timescales (tens to hundreds of picoseconds). Additionally, the accuracy of dynamic properties depends on the DFT XC functional, pseudopotentials, and finite simulation times, and

rare events such as slow Li diffusion may require longer simulations or enhanced sampling techniques.

1.2 Objective

The main goal of the thesis is to study some issues and problems that occur in LIBs and SIBs during the charging/discharging process. The primary objective of this research is to investigate the structural changes, as well as to evaluate the impact of elemental doping in P2-Na_xMnO_2 system during cycling. For P2-$Na_{0.67}MnO_2$ studies for SIBs, the main idea is to study impact of doping, Na and TMs ordering, as well as to affirm the preservation of the P2 structure at different levels of de(sodiation). The objective is also to study redox mechanism during charging/discharging through electronic structure calculations.

In this work, an extensive Coulomb energy analysis, density functional theory (DFT) calculations and ab initio molecular dynamics (AIMD) simulation with different exchange-correlation functionals—specifically PBE, PBE-D3, PBE+U, and HSE06 functional are utilized. Different functionals are used to check their influence on the predicted structural behavior, redox mechanism and mechanical stability. The computational study includes analysis of redox mechanism (magnetic moments), spin density difference (SDD), Bader charge analysis, and bond lengths. These properties are correlated with the calculated lattice parameters to reveal the mechanisms behind phase transitions occurring during charging/discharging process. In particular, the research is also aimed to study mechanical stability by finding the origin behind the cracking of cathode materials, i.e., $LiCoO_2$, during cycling, which is a possible cause of capacity fading in LIBs.

Overall, this thesis provides a detailed understanding of mechanical and structural stability as well as redox mechanism of layered oxides cathodes. The main aim is to determine parameters controlling cyclability and capacity of these materials during charge/discharge and study the impact of substitution/doping on these quantities.

The research questions of the thesis:

I: What is the origin behind the cracking of cathode materials, i.e. Li_xCoO_2 during

1

cycling for LIBs.

II: How do lattice parameter changes, phase transition and doping impact the structural stability of P2-type cathode materials in SIBs?

III: What is the origin behind the phase stability (transition) in P2-type cathode materials (P2-Na_xMnO_2) for SIBs? How can we suppress it?

1.3 Thesis Outlines

This thesis is divided into five chapters:

The first chapter is the current introduction part. This chapter contains motivation for this work, basic components, types of batteries and importance of LIBs and SIBs.

Results and discussions of the thesis consist of four chapters and are divided into three parts. The first part, corresponding to chapter 2 is mainly about the study of mechanical stability of Li- based cathode material and the second part, corresponding to chapters 3 is study of impact of substitution/doping as well as redox mechanism, third part consists of chapters 4 and 5 and is mainly discussing the structrual stability of Na-based cathode materials.

In chapter 2, using DFT calculations and microstructural mechanical analysis the possible reason for the mechanical stability of Li_xCoO_2 is presented. We computed anisotropic changes in the lattice parameters during charging/discharging, and mechanical properties with various Li concentrations and defects are presented. To study structural phase transitions on the atomic scale, we calculated the stress as a function of strain as well as a function of total energy. We also modelled a typical microstructure comprising randomly oriented particles (created by a collaborator), sharp space charge and point defects to find the origin of microcracking of LCO cathodes.

During my Ph.D. I got the chance to work on several projects together with our international experimental cooperation partners. The results of two of these studies are summarized in the Chapter 3 with a special focus on my theory simulations to determine the redox mechanisms in Na-based layered cathode materials. This work aimed to determine the effect of co-doping of electro-inactive (Li)

and electro-active (Co/Ni) elements on the structural stability and redox mechanism of the P2-$Na_{0.67}MnO_2$ cathode. The key experimental findings were P2-$Na_{0.75}[Li_{0.14}Ni_{0.17}Mn_{0.69}]O_2$ (LNM) system showed better capacity retention as compared to P2-$Na_{0.67}[Li_{0.22}Mn_{0.78}]O_2$ (LM) system. The questions to be answered by the simulations were: why is capacity retention in Ni-doped system and what is the redox mechanism of P2-$Na_{0.67}[Li_{0.22}Mn_{0.78}]O_2$ (LM), P2-$Na_{0.75}[Li_{0.156}Co_{0.156}Mn_{0.689}]O_2$ (LCM) and P2-$Na_{0.75}[Li_{0.14}Ni_{0.17}Mn_{0.69}]O_2$ (LNM) during the charging/discharging process?

Chapter 4 is the combined study of DFT and experimental results (performed by a collaborator). This chapter presented the effect of co-doping on the structural stability of Na-based cathode materials during the charge/discharge process. We simulated pristine and charged states to determine high-performance cathode materials using multi-level optimization approaches such as Coulomb energy analysis, DFT optimization, and AIMD simulation, and also compared with experimental results. We computed the redox mechanism using DFT to clearly show which ions and how much they are oxidized during charging.

It is important to study the origin of phase transition during charging/discharging in Na-based cathodes, and the computational simulation is expected to clarify this fundamental mechanism. Therefore, in chapter 5, we study the possible reasons behind the phase transition and try to find out how to suppress it. Using different computational approaches, on bare and Li doped P2-Na_xMnO_2, which include the influence of desodiation on phase stability, lattice parameters changes, and redox mechanism, are presented. We analyzed pairwise ion-ion interactions and pair distribution function to deeply explain this phenomenon.

1.4 References

1. Ausfelder, F., Beilmann, C., Bertau, M., Bräuninger, S., Heinzel, A., Hoer, R., ... & Ziegahn, K. F., ChemBioEng Reviews, 2017, 3, 4, 144-210.
2. C. Delmas, Advanced Energy Materials, 2018, 8, 1703137.
3. Tobias, P., Richard, K., Simon, D. & Martin, W., Journal of Solid State Electrochemistry, 2017.
4. Section 2 - Rechargeable Cells and Batteries, In EDN Series for Design Engineers, Rechargeable Batteries Applications Handbook, Newnes, 1998, Pages 5-33, ISBN 9780750670067.
5. Faria, R., Marques, P., Garcia, R., Moura, P., Freire, F., Delgado, J., & de Almeida, A. T., Journal of Power Sources, 2014, 262, 169-177.
6. J.M. Tarascon and M. Armand, Nature, 2001, 6861, 414, 359−367.
7. M. Winter, B. Barnett and K. Xu, Chem. Rev., 2018, 118, 11433−11456.
8. Selvaraj, V., & Vairavasundaram, I, Journal of Energy Storage, 2023, 72, 108777.
9. W. J. Zhang, J. Power Sources, 2011, 196, 877.
10. K. T. Lee, S. Y. Jeong, J. Cho, Account of Chemical Research, 2013, 46, 1161.
11. Bolin, B., & Kheshgi, H. S., Proceedings of the National Academy of Sciences, 2001, 9, 98, 4850-4854.
12. X. Shen, H. Liu, X. B. Cheng, C. Yana , J. Q. Huang, Energy Storage Material, 2018, 12, 161.
13. B. Babu, P. Simon, A. Balducci, Advance Energy Material, 2020, 10, 2001128.
14. H. P. Wu, H. Jia, C. M. Wang, J. G. Zhang, W. Xu, Advance Energy Material, 2021, 11, 2003092.
15. C. Choi, D. S. Ashby, D. M. Butts, R. H. DeBlock, Q. Wei, J. Lau, B. Dunn, Nat. Rev. Mater. 2020, 5, 5.
16. V. Augustyn, P. Simon, B. Dunn, Energy Environmental Science, 2014, 7, 1597.

17. Y. Y. Liu, Y. Y. Zhu, Y. Cui, Nature Energy, 2019, 4, 540.

18. F. Duffner, N. Kronemeyer, J. Tübke, J. Leker, M. Winter, R. Schmuch, Nature Energy, 2021, 6, 123.

19. Y. H. Zhu, X. Yang, D. Bao, X. F. Bie, T. Sun, S. Wang, Y. S. Jiang, X. B. Zhang, J. M. Yan, Q. Jiang, Joule, 2018, 2, 736.

20. K. Liu, Y. Y. Liu, D. C. Lin, A. Pei, Y. Cui, Science Advances, 2018, 4, eaas9820.

21. Y. Qiao, K. Z. Jiang, H. Deng, H. S. Zhou, Nature Catalysis, 2019, 2, 1035.

22. T. Devic, B. Lestriez, L. Roue, ACS Energy Letter, 2019, 4, 550.

23. D. L. Wood III, J. L. Li, C. Daniel, Journal of Power Sources, 2015, 275, 234.

24. Armand, M. B. Intercalation Electrodes, 145–161 (Springer US, Boston, MA, 1980).

25. Mizushima, K., Jones, P., Wiseman, P. & Goodenough, J., Materials Research Bulletin, 1980, 15, 783–789.

26. Nishi, Y. The dawn of lithium-ion batteries. Interface magazine 25, 71–74 (2016).

27. Peled, E. & Menkin, S. Sei, Journal of The Electrochemical Society, 2017, 164, A1703–A1719.

28. HS. Hirsh, Y. Li, DHS. Tan, M. Zhang, E. Zhao, YS. Meng, Advance Energy Material, 2020, 10, 2001274.

29. A. Rudola, R. Sayers, C.J. Wright, J. Barker, Nature Energy, 2023, 8, 215-218.

30. C. Delmas, Advanced Energy Materials, 2018, 8, 1703137.

31. P. K. Nayak, L. Yang, W. Brehm, P. Adelhelm, Angewandte Chemie International Edition, 2018, 57, 102-120;

32. Q. Liu, Z. Hu, W. Li, C. Zou, H. Jin, S. Wang, S. Chou, S. X. Dou, Energy and Environmental Science 2021, 14, 158-179.

33. A. Rudola, A. J. R. Rennie, R. Heap, S. S. Meysami, A. Lowbridge, F. Mazzali, R. Sayers, C. J. Wright, J. Barker, Journal of Materials Chemistry A 2021, 9, 8279-8302.

34. G. Rousse, M. E. Arroyo-de Dompablo, P. Senguttuvan, A. Ponrouch, J.-M. Tarascon, M. R. Palacín, Chemistry of Materials 2013, 25, 4946-4956.

35. O. Lenchuk, P. Adelhelm, D. Mollenhauer, Phys Chem Chem Phys, 2019, 21, 19378-19390.

36. S. P. Ong, V. L. Chevrier, G. Hautier, A. Jain, C. Moore, S. Kim, X. Ma, G. Ceder, Energy & Environmental Science 2011, 4, 3680-3688.

37. L. F. Zhao, Z. Hu, W. H. Lai, Y. Tao, J. Peng, Z. C. Miao, Y. X. Wang, S. L. Chou, H. K. Liu, S. X. Dou, Adv. Energy Mater. 2021, 11, 2002704.

38. P. K. Nayak, L. Yang, K. Pollok, F. Langenhorst, L. Wondraczek, P. Adelhelm, Batteries Supercaps 2018, 2, 104.

39. P. K. Nayak, L. Yang, W. Brehm, P. Adelhelm, Angew. Chem., Int. Ed. 2018, 57, 102.

40. M. H. Han, E. Gonzalo, G. Singh, T. Rojo, Energy Environ. Sci. 2015, 8, 81.

41. K. Kubota, S. Kumakura, Y. Yoda, K. Kuroki, S. Komaba, Adv. Energy Mater. 2018, 8, 1703415;

42. N. Sabi, A. Sarapulova, S. Indris, S. Dsoke, V. Trouillet, L. Mereacre, H. Ehrenberg, I. Saadoune, J. Power Sources 2021, 481, 229120.

43. N. Ortiz-Vitoriano, N. E. Drewett, E. Gonzalo, T. Rojo, Energy Environ. Sci. 2017, 10, 1051.

44. Komaba, S.; Takei, C.; Nakayama, T.; Ogata, A.; Yabuuchi, N. Electrochem. Commun. 2010, 12, 355.

45. Pauling, L. J. Am. Chem. Soc. 1929, 51, 1010.

46. X. Xiang, K. Zhang, J. Chen, Adv. Mater. 27 (2015) 5343–5364.

47. M.H. Han, E. Gonzalo, G. Singh, T. Rojo, Energy Environ. Sci. 8 (2015) 81–102.

48. R.J. Clément, P.G. Bruce, C.P. Grey, J. Electrochem. Soc. 162 (2015) A2589–A2604.

49. N. Ortiz-Vitoriano, N.E. Drewett, E. Gonzalo, T. Rojo, Energy Environ. Sci. 10 (2017) 1051–1074.

50. Clément, R. J., Bruce, P. G., & Grey, C. P., Journal of The Electrochemical Society, 2015, 14, 162, A2589.

51. T. Wang, D. Su, D. Shanmukaraj, T. Rojo, M. Armand, G. Wang, Electrochem. Energy Rev. 2018, 1, 200.

52. C. Delmas, C. Fouassier, P. Hagenmuller, Physica B+C 1980, 99B, 81.

53. C. Delmas, J.-J. Braconnier, C. Fouassier, P. Hagenmuller, Solid State Ionics 1981, 4, 165.

54. Zhao, C., Yao, Z., Wang, Q., Li, H., Wang, J., Liu, M., & Hu, Y. S., Journal of the American Chemical Society, 2020, 12, 142, 5742-5750.

55. X. Ma, H. Chen, G. Ceder, Journal of Electrochemical Society, 2011, 12, 158, A1307.

56. N. Voronina, H. J. Kim, H. M. Shin, S.T. Myung, Journal of power Sources, 2021, 514, 230581.

57. L. Zhang, T. Yuan, L. Soule, H. Sun, Y. Pang, J. Yang, S. Zheng, ACS Applied Energy Material, 2020, 3, 3770-3778.

58. N. Voronina, H. J. Kim, A. Konarov, N. Yaqoob, K.S. Lee, P. Kaghazchi, S.T. Myung, Advance Energy Material, 2021, 11, 2003399.

59. Z. Lu, J.R. Dahn, Journal of Electrochemical Society, 2001, 148, A1225.

60. N. Yabuuchi, R. Hara, K. Kubota, J. Paulsen, S. Kumakura, and S. Komaba, J. Mater. Chem. A, 2, 16851 (2014).

61. Z. Lu and J. R. Dahn, J. Electrochem. Soc., 148, A1225 (2001).

62. D. H. Lee, J. Xu, and Y. S. Meng, Phys. Chem. Chem. Phys., 15, 3304 (2013)

63. N. Yabuuchi, M. Kajiyama, J. Iwatate, H. Nishikawa, S. Hitomi, R. Okuyama, R. Usui, Y. Yamada, and S. Komaba, Nat. Mater., 11, 512 (2012).

64. G. Singh, J. M. L. del Amo, M. Galceran, S. Perez-Villar, and T. Rojo, ´ J. Mater. Chem. A, 3, 6954 (2015).

65. Ewald, P. P, Annalen der Physik 369, 253–287 (1921).

66. de Leeuw, S. W., Perram, J. W., Smith, E. R. & Rowlinson, J. S, A. Mathematical and Physical Sciences 373, 57–66 (1980).

67. Hohenberg, P. & Kohn, W. Inhomogeneous electron gas. Phys. Rev. 136, B864–B871 (1964).

68. W. Kohn, & J.L. Sham, Phys. Rev. 140, A1133–A1138 (1965).

69. J.P. Perdew, K. Schmidt, V. Van Doren, C. Van Alsenoy, & P. Geerlings, AIP Conference Proceedings 577, 1–20 (2001).

70. J.P. Perdew, J. P. & W. Yue, Phys. Rev. B 33, 8800–8802 (1986).

71. S.L. Dudarev, G.A. Botton, S.Y. Savrasov, C.J. Humphreys, and A.P. Sutton, Physical Review. B, 1998, 57, 1505.

72. J. Heyd, G.E. Scuseria, & M. Ernzerhof, The Journal of Chemical Physics, 2003, 18, 8207-8215.

73. D.C. Rapaport, R.L. Blumberg, S.R. McKay, W. Christian, et al, Computers in Physics 10, 456–456 (1996).

74. M. Tuckerman, Statistical mechanics: theory and molecular simulation (Oxford University Press, 2010).

75. H. A. Posch, Iliam G. Hoover, F. J. Vesely, *Phys. rev. A.* **1986,** 33, 4253 .

76. M. P. Allen, D. J. Tildesley, Computer Simulation of Liquids, Oxford University Press, 2017.

77. M. Parrinello, A. Rahman, *Phys. Rev. Lett.* **1980,** 45, 1196.

78. M. Parrinello, A. Rahman, *J. Appl. Phys.* **1981,** 52, 7182.

2

Delithiation-induced oxygen vacancy formation increases microcracking of $LiCoO_2$ cathodes

Abstract: Cracking of cathode materials during cycling is a main cause of capacity fading in Li-ion batteries. In this work, by performing atomistic and microscale simulations, we study the possible reason behind the cracking of Li_xCoO_2 $(Lix\mathrm{CO})$ microstructures. It is shown that tensile uniaxial lattice strains larger than 2% along the c-direction ($\varepsilon_{\mathfrak{c}}$) can cause displacement of Li ions and a yield drop in the stress-strain $\sigma_{\mathfrak{c}}$ ($\varepsilon_{\mathfrak{c}}$) plot in $(Lix\mathrm{CO})$. By modelling a typical microstructure consisting of packed microparticles and performing continuum mechanical analysis on the mesoscale we found that the electrochemically-induced (L1.00CO $\rightarrow$ L0.50CO) mechanical $\varepsilon_{\mathfrak{c}}$ in the microstructure is, however, only $-2.5\% \leq \varepsilon_{\mathfrak{c}} \leq +0.5\%$. Moreover, we found that even a sharp space charge region cannot cause any significant local tensile strain. However, a small amount of oxygen vacancy (V_O^x) introduces a large local strain of $\varepsilon_{\mathfrak{c}} = 3\%$ leading to the displacements of Li ions. Furthermore, we found that the formation of V_O^x becomes more favorable with delithiation (L1.00CO $\rightarrow$ L0.50CO). The results of this work, thus, indicate that the delithiation-induced formation of V_O^x, which is a well-known phenomenon observed experimentally in operating cathode materials, can be a reason of microcracking of Li-based layered cathodes.

This chapter is based on the publication:
N. Yaqoob, R. Mücke, O. Guillon, P. Kaghazchi, Journal of Power Sources, 2022, 533, 231316.

2.1 Introduction

$LiCoO_2$(LCO) as a cathode material for Li-ion batteries was proposed in 1980 by Mizushima and Goodenough[1]. It is still one of the most popular and widely used compound for energy storages in electronic devices. LCO has a layered crystal structure (with a rhombohedral space group: R-3m) in which Li-ions deintercalate/intercalate from/into Li sites between slabs of CoO_6 octahedra during charge/discharge[2]. In principle, it can provide a long cycle life. A main drawback of this system is its low practical energy density due to a structural instability occurring when more than 0.5 Li is extracted.

In practice, only about a 0.5 Li content can be removed from LCO which gives a specific capacity of about 140 mAh/g with an upper cutoff voltage of about 4.2 V[3]. Wang et al.[4] performed a Transmission Electron Microscopy (TEM) study on LCO and reported that after 50 cycles, 20% of the particles were indeed fractured between 2.5 V and 4.35 V at a 0.2 C rate. Yoon et al.[5] studied this system and found that the capacity experiences fading by 2.2% and 6.5% for a delithiation of 0.5 Li per CoO_2 after 10 and 50 charge-discharge cycles, respectively. It is believed that the changes in lattice parameters cause an irreversible damage of LCO structure, in particular the collapse of structure along the c direction [6], leading to cracking and failure, and thereby the capacity fading.

Zhou et al.[6] performed an *in situ*-XRD experiment to determine the variation of lattice parameters of LCO during delithiation i.e. Li_xCoO_2 (L*x*CO, x = 1.0 and 0.5). They observed a contraction of 0.2% (a = 2.82 Å $\rightarrow$ 2.81 Å) along the *a*-axis, while an expansion of 1.99% (c = 14.09 Å $\rightarrow$ 14.37 Å) along the *c*-axis when x = 1.0 $\rightarrow$ 0.5. A similar experiment by Amatucci et al.[7] indicates that the lattice parameter *a* contracts by ~ 0.18% when x = 1.0 $\rightarrow$ 0.6 followed by a subsequent increase of 0.24% when x = 0.4$\rightarrow$ 0.0. However, the *c* parameter experiences an expansion of 1.8% for x = 1.0 $\rightarrow$ 0.5 followed by a contraction of -1.8% for x = 0.5$\rightarrow$ 0.2 [7].

Ex situ X-Ray Diffraction (XRD) studies by Chen et al.,[3] Amatucci et al.,[7] and Ohzuku et al.[8] on L_xCO showed that when x = 1.0 $\rightarrow$ 0.25, i.e. V= 4.2 $\rightarrow$ 4.8 V, a phase transition from the initial as synthesized O3 phase (oxygen stacking

of ···ABCABC···) to a stage-two phase (H1-3) occurs. Chen et al.[3] measured the composition of H1-3 phase to be $Li_{0.12}CoO_2$ (*a* = 2.82 Å and *c* = 13.54 Å). Finally, Amatucci et al.[7] observed a further phase transition from O3-L*x*CO to O1 $-$ CoO_2 (oxygen stacking of ···ABAB···) for *U*= 5.2 V. Qu et al.[9] and Cheng et al.[10] performed nanomechanical measurement of plastic, fracture, and elastic properties of LCO using a nanoindentation test. They measured Young's modulus to be in the range of 151–236 GPa [9,10]. Feng et al.[11] studied the effect of electrochemical cycling on the strength of LCO using a TEM–based nanopillar compression experiment. They estimated that this system can withstand an ultimate strength in the range of 5.62 $\pm$ 0.22 GPa, 3.91$\pm$1.22 GPa, and 2.27$\pm$1.07 GPa for pristine and after 1 and 11 cycles, respectively.

First principles density functional theory (DFT) has also been applied to compute phase transition, lattice parameters, and the mechanical properties of L_xCO cathode materials[11−14]. For example, using DFT-LDA, Ceder et al.[12] calculated formation energies to simulate the staging phase transitions (O3-phase$\rightarrow$ H1-3-phase $\rightarrow$ O1-phase) in L_xCO that were proposed by experimental works of Ohzuku et al.[8] and Amatucci et al[7]. Arup et al.[15] calculated (with DFT-PBE) changes in the lattice parameters of L*x*CO to be *a* = 2.85 Å $\rightarrow$ 2.82 Å $\rightarrow$ 2.83 Å and *c* = 14.05 Å $\rightarrow$ 14.42 Å $\rightarrow$ 14.21 Å for *x* = 1.0 $\rightarrow$ 0.5 $\rightarrow$ 0.0. Qi et al.[13] using HSE06, while Feng et al.[11] and Wu et al.[14] using DFT-PBE computed the mechanical properties of L_xCO during Li insertion/deinsertion. They found that Young's modulus decreases dramatically from 264 GPa to 59.8 GPa during the deintercalation of *x* = 1.0 $\rightarrow$ 0.0[13]. The bulk modulus B and shear modulus G decrease significantly from 166.74 GPa to 68.69 GPa and from 111.38 GPa to 41.71 GPa respectively[14]. Feng et al.[11] calculated (with DFT-PBE) the ultimate tensile strength for L_xCO by introducing Li vacancies heterogeneously on a single plane in the crystal. They showed that the strength, defined by the maximum stress that can be generated by applying strain, decreases from 33.7 GPa 12.7 GPa when *x* = 1.0 $\rightarrow$ 0.5. They reported that the critical strain, up to which the material can accommodate the arising stress before it experiences restructuring and stress drops with applying larger strain fields, is 33% and 8% for

x =1.0 and 0.5, respectively.

However, according to the DFT-PBE study by Wu et al.[14] the strength decreases from 40 GPa to 32 GPa (and critical strains from 32% to 30%) with the delithiation of *x* =1.0 $\rightarrow$ 0.5. The previously calculated values of strengths with DFT calculation are significantly larger than the experimental ones. Moreover, the proposed critical strain values above which the layered cathode materials experience cracking are considerably higher than the delithiation-induced contraction or expansion of lattice parameters. Direction and maximum possible magnitude of electrochemically-driven strain/stress generation in a microstructure of LCO have not been modelled so far. This information is required to find out if microstructuring is the reason of cracking. Moreover, the impact of point defects has not been investigated. In this work, we address these issues by combining extensive DFT calculations as well as microstructure modelling and electrochemo-mechanical analysis on the grain level.

2.2 Method

Spin-polarized DFT calculations were performed using the projector augmented wave (PAW)[16] potential method implemented in the Vienna *Ab Initio* Simulation Package (VASP) code [17]. The Perdew–Burke–Ernzerhof (PBE)[18] form of generalized gradient approximation (GGA) was used as the exchange-correlation functional. We also checked the influence of adding a Hubbard *U* (Dudarev et al. approach[19] : *U-J* = 5.9 eV for Co[20]) and dispersion D3[21] correction on the mechanical properties. It was found that for the calculation of lattice parameters, the PBE and PBE-D3 results are in good agreement with experimental values at high and low Li-concentrations respectively. However, the PBE functional without any correction gives more reasonable data for mechanical properties. To perform electrostatic energy analysis as well as DFT calculations for discharged and charged systems, we modelled the L*x*CO structure with a space group of R-3m crystal and a unit cell of 2×2×1 ($Li_{12}Co_{12}O_{24}$). A Gamma-centered k-point mesh of 4×4×1 and an energy cut-off of 800 eV were applied. Electronic and force convergence criteria of 10^{-5} eV and 10^{-3} eV/Å, respectively, were considered for DFT calculations.

For the calculation of elastic constants C_{ij}, we kept fixed the magnetic moment and atomic coordinates to the optimized ones. C_{ij} matrix was computed using the strain values of 0, $\pm$0.5%, and $\pm$1% (see Table 2.1 and Figure 2.1). After computing C_{ij}, we obtained the mechanical properties such as Young's, bulk, and shear modulus as well as Poisson's ratio by using the Voigt-Reuss-Hill (VRH) homogenization scheme[22]. To find the most favourable occupation of Li sites by Li ions in L0.50CO, $Li_6Co_{12}O_{24}$, we modelled all possible atomic configurations with various combinations of 6 Li ions in 12 Li sites. We created a total number of $12!/6!6! = 924$ structures. For charge balancing, we used elementary charges of 1+ for Li, 3.5+ for Co, and 2$-$ for O, respectively. Afterwards, we performed DFT-PBE calculations on 5 distinguishable electrostatically favourable structures and obtained the lowest total energy structure. Total Coulomb energy calculations were carried out using the so-called supercell code[23].

Atomistic structures were visualized with the VESTA program[24]. The mechanical response inside the polycrystalline microstructure of LCO was simulated using the grid based solver ElastoDict FeelMath-LD in the software package GeoDict (Math2Market GmbH, Kaiserslautern, Germany)[25–27]. To model the LCO microstructure, an experimental microstructure from a FIB- SEM image of a mixed LLZO-LCO cathode from our previous study on solid state batteries[25,28] was used and all LLZO particles were replaced by LCO. The microstructure was segmented into grains using the watershed method (GrainFind module of GeoDict) yielding a median diameter of 2.4 µm. A random set of Euler angles was assigned to each grain resulting in a uniform distribution of orientations. The uncharged (i.e. fully lithiated) particles were assumed to be in the stress-free state. No external forces were applied during the simulation.

2.3 Results and discussion

2.3.1 Lattice parameters

We first computed the lattice parameters of L_xCO with *x* = 1.0, 0.5, 0.12, and 0.0. We found that the parameter *a* contracts from 2.85 Å to 2.82 Å and *c* (hereafter it

is defined to be 3 intralayer + 3 interlayer separations) expands from 14.01 Å to 14.46 Å for *x* = 1.0 → 0.5. With further delithiations, namely *x* = 0.5 → 0.12 → 0.0, *a* does not change much, while *c* decreases significantly: *a* = 2.82 Å → 2.83 Å → 2.82 Å and *c* = 14.46 Å → 14.35 Å → 14.16 Å. Our results for *x* = 1.0 → 0.5 → 0.12 → 0.0 are in fair agreement with the reported experimental values of *a* = 2.82 Å → 2.81 Å → 2.82 Å → 2.82 Å and *c* = 14.05 Å → 14.37 Å → 13.54 Å → 12.87 Å with delithiation reported by Wang et al.[31], Zhou et al.[6], Chen et al.[3] and Amatucci et al[7]. Afterwards, the mechanical properties of L*x*CO with various Li concentrations *x* and defects were calculated.

2.3.2 Mechanical properties

The computed values of *v* for L_xCO with various Li concentrations and defects (Table 2.2) are $0.24 - 0.25$, which agree well with the experimental value of 0.23 and 0.24 reported by Meng et al.[29] and Cheng et al[30]. We calculated B to be 159.43 GPa for L1.00CO which is slightly higher than the experimental value of 149 GPa reported by Wang et al[31].

A previous DFT-PBE study on a defect-free L1.00CO crystal by Wu et al.[14] computed Y, B and G to be 252.09 GPa, 166.74 GPa, and 111.38 GPa, respectively, which are even higher than our calculated values for L1.00CO (Table 2.2) as well as reported experimental ones[9,28,32]. Yamakawa et al.[32] computed the B value for LCO to be 146.44 GPa which agrees with the experimental value of 149 GPa[32], but they assumed $v = 0.32$ in their calculation which is very large compared to the experimental value of 0.23[29] and 0.24[30].

Table 2.1: Calculated Stiffness matrix for L1.00CO without (a) and with Li-vacancy (b), Co-vacancy (c), and O-vacancy (d) as well as defect-free L0.50CO,(e) Li0.12CO, and (f) CoO_2 (g).

(a)

$$C=\begin{bmatrix} 342.91 & 107.64 & 70.07 & 0 & 0 & 0 \\ 0 & 342.91 & 70.07 & 0 & 0 & 0 \\ 0 & 0 & 270.51 & 0 & 0 & 0 \\ 0 & 0 & 0 & 77.85 & 0 & 0 \\ 0 & 0 & 0 & 0 & 77.85 & 0 \\ 0 & 0 & 0 & 0 & 0 & 117.64 \end{bmatrix} \text{GPa}$$

(b)

$$C=\begin{bmatrix} 320.85 & 62.80 & 110.56 & 0 & 0 & 0 \\ 0 & 320.85 & 110.56 & 0 & 0 & 0 \\ 0 & 0 & 190.80 & 0 & 0 & 0 \\ 0 & 0 & 0 & 99.71 & 0 & 0 \\ 0 & 0 & 0 & 0 & 99.71 & 0 \\ 0 & 0 & 0 & 0 & 0 & 129.03 \end{bmatrix} \text{GPa}$$

(c)

$$C=\begin{bmatrix} 324.65 & 68.55 & 103.83 & 0 & 0 & 0 \\ 0 & 324.65 & 103.83 & 0 & 0 & 0 \\ 0 & 0 & 170.66 & 0 & 0 & 0 \\ 0 & 0 & 0 & 86.21 & 0 & 0 \\ 0 & 0 & 0 & 0 & 86.21 & 0 \\ 0 & 0 & 0 & 0 & 0 & 128.05 \end{bmatrix} \text{GPa}$$

(d)

$$C=\begin{bmatrix} 324.13 & 72.54 & 107.20 & 0 & 0 & 0 \\ 0 & 324.13 & 107.20 & 0 & 0 & 0 \\ 0 & 0 & 157.63 & 0 & 0 & 0 \\ 0 & 0 & 0 & 98.26 & 0 & 0 \\ 0 & 0 & 0 & 0 & 98.26 & 0 \\ 0 & 0 & 0 & 0 & 0 & 125.80 \end{bmatrix} \text{GPa}$$

(e)

$$C=\begin{bmatrix} 308.62 & 78.33 & 84.94 & 0 & 0 & 0 \\ 0 & 308.62 & 84.94 & 0 & 0 & 0 \\ 0 & 0 & 187.89 & 0 & 0 & 0 \\ 0 & 0 & 0 & 64.09 & 0 & 0 \\ 0 & 0 & 0 & 0 & 64.09 & 0 \\ 0 & 0 & 0 & 0 & 0 & 115.15 \end{bmatrix} \text{GPa}$$

(f)

$$C=\begin{bmatrix} 318.81 & 69.60 & 93.44 & 0 & 0 & 0 \\ 0 & 318.81 & 93.44 & 0 & 0 & 0 \\ 0 & 0 & 129.28 & 0 & 0 & 0 \\ 0 & 0 & 0 & 73.39 & 0 & 0 \\ 0 & 0 & 0 & 0 & 73.39 & 0 \\ 0 & 0 & 0 & 0 & 0 & 124.61 \end{bmatrix} \text{GPa}$$

(g)

$$C=\begin{bmatrix} 250.20 & 128.88 & 58.08 & 0 & 0 & 0 \\ 0 & 250.20 & 58.08 & 0 & 0 & 0 \\ 0 & 0 & 174.06 & 0 & 0 & 0 \\ 0 & 0 & 0 & 84.06 & 0 & 0 \\ 0 & 0 & 0 & 0 & 84.06 & 0 \\ 0 & 0 & 0 & 0 & 0 & 60.66 \end{bmatrix} \text{GPa}$$

Possible reasons for the difference between our results and those of Yamakawa et al.[32] might be due to the applied cut off energy and number of computed energy vs. strain points. The reason of overestimation of B in our calculation compared to the experiment is most likely due to the fact that a real LCO crystal contains defects at finite temperature. To address this issue, mechanical properties of L1.00CO with Li, Co, or O vacancy (V^{x}_{Li} , V^{x}_{Co}, and V^{x}_{O}) were computed. It is found that the values of mechanical properties decrease in all three defective cases in comparison to the defect-free system (Table 2.2). The obtained values of B become 147.58 GPa and 146.49 GPa for L1.00CO with V^{x}_{Co} and V^{x}_{o}, respectively, which are close to the measured value of 149 ± 2 GPa reported by Wang et al[31]. Moreover, with these atomic defects, the magnitudes of Y and G become smaller and more comparable to the corresponding experimental values (Table 2.2). In addition, the value of v re-

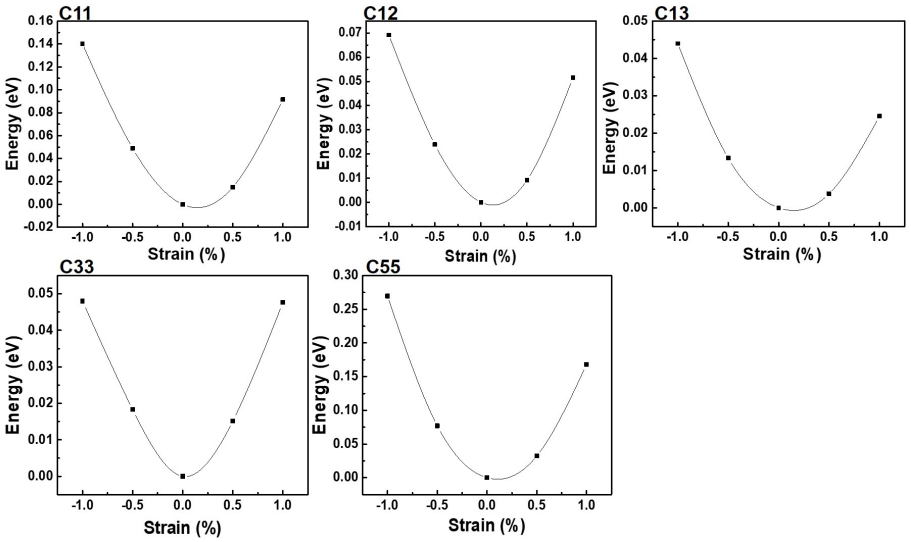

Figure 2.1: Computed changes in strain energy as function of various types of strains in L1.00CO.

Table 2.2: Calculated mechanical properties of LxCO with different defect types and Li concentrations: bulk modulus (B), shear modulus (G), and Young's modulus (Y) in GPa as well as Poisson's ratio (v). The subscripts V and R represents the results using Voigt-Reuss-Hill homogenization scheme [22]. Experimental values are listed for comparison.

	X = 1	X = 1 V^x_{Li}	X = 1 V^x_{Co}	X = 1 V^x_O	X = 0.5	X = 0.12	X = 0	Exp
B_v	161.32	155.59	152.49	153.31	144.62	142.21	129.39	
B_R	157.54	150.93	142.68	139.66	137.78	119.88	119.70	
B	159.43	153.26	147.58	146.49	141.20	131.04	124.55	149 $\pm$[31]
G_v	101.90	102.26	96.34	99.06	85.80	88.31	74.38	
G_R	97.41	91.40	84.88	84.02	78.79	72.09	71.56	
G	99.66	96.83	90.61	91.54	82.29	80.20	72.97	80 $\pm$1[30]
Y	247.43	239.96	225.65	227.27	206.72	199.84	183.15	$151 - 236$[9]
v	0.24	0.24	0.24	0.24	0.25	0.25	0.25	0.23[29], 0.24[30]

mains unchanged and, therefore, it is still comparable to the experimental value.[30] The reason of softening of L1.00CO with the presence of V^x_{Co} or V^x_O vacancies is most likely due to broken Co-O bonds or weakening of electrostatic O-Li-O interac-

tion. Furthermore, we found that the mechanical strength of L*x*CO decreases with delithiation. This is also probably because of the weakening of O-Li-O interaction, i.e. interlayer interaction, with delithiation. Our computed delithiation-induced decrease in B, G, and Y is smaller than those computed by Wu et al[14]. Nevertheless, there is no experimental data on delithiated phases to compare with our results.

2.3.3 Stress-Strain curve

Afterwards, we computed the stress σ as function of strain ϵ along *a* (σ_a, ϵ_a) and *c* (σ_c, ϵ_c) direction for L*x*CO. To distinguish the likely effect of delithiation from that of point defects on σ and ϵ, we first focus on L*x*CO without V^x_{Co} and V^x_O. For L1.00CO (Fig.2.2), it is found that both σ_a and σ_c drop above large tensile ϵ_a and ϵ_c values. The atomic structure of each case undergoes a large displacement under these conditions. Due to the structural phase transition, the σ value drops significantly. Our computed critical strains $(12\% < \epsilon_a, 18\% < \epsilon_c)$ above which system may ex-

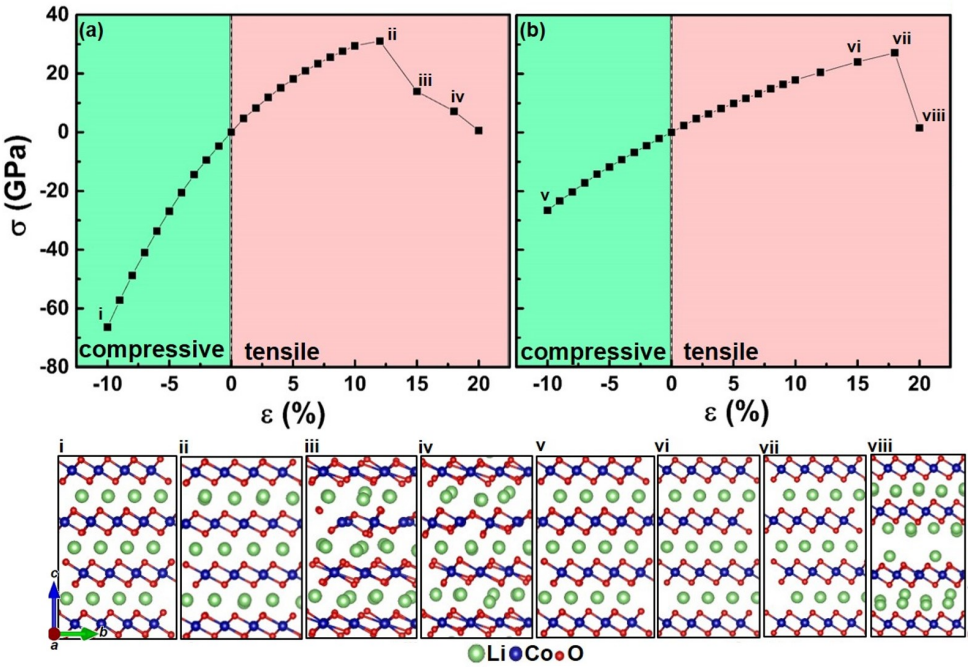

Figure 2.2: Calculated uniaxial stress versus strain in L1.00CO along the *a*-direction and *c*-direction and side views of the selected atomistic structures.

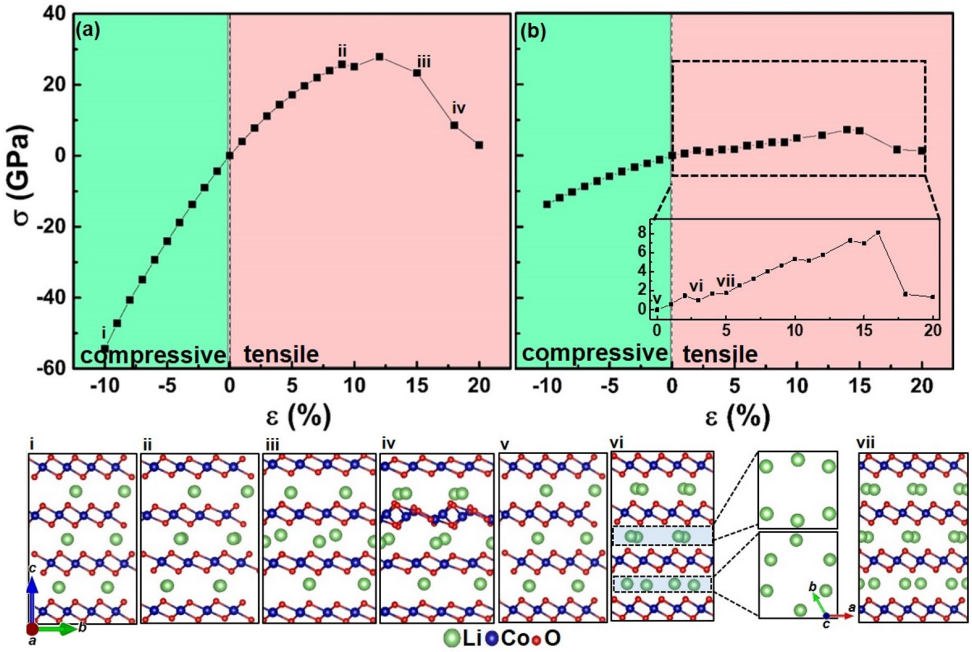

Figure 2.3: Calculated uniaxial stress versus strain in L0.50CO along the a-direction and c-direction and side views of the selected atomistic structures

perience cracking are, however, clearly much higher than expected values for ceramic materials. Previous theoretical studies by Fang et al.[11] and Wu et al.[14] have reported even larger critical tensile strains, namely > 30%. Figure 2.3 shows the computed stress as function of uniaxial strain plot along the *a* and *c* directions for the L0.50CO system. It is found that under compressive ϵ_a and ϵ_c as well as tensile ϵ_a strains the response of L0.50CO is similar to that of L1.00CO system. However, under tensile ϵ_c strains, σ_c increases linearly only up to 2% strain. Above this critical strain value, the stress magnitude drops. Previous experimental measurements using advanced scanning transmission electron microscopy (STEM) and high-angle annular dark-field (HAADF) by Yan et al.[33] also found intragranular cracking along the (001) orientation in a cycled NCM111 structure.

Moreover, we find that the stress drops at 5% and 11% strains as well. Furthermore, we computed the total energy as a function of strain (Fig. 2.4) indicating phase transitions occurring for 2% < ϵ_c < 3%, 4% < ϵ_c < 5%, and 10% < ϵ_c < 11%.

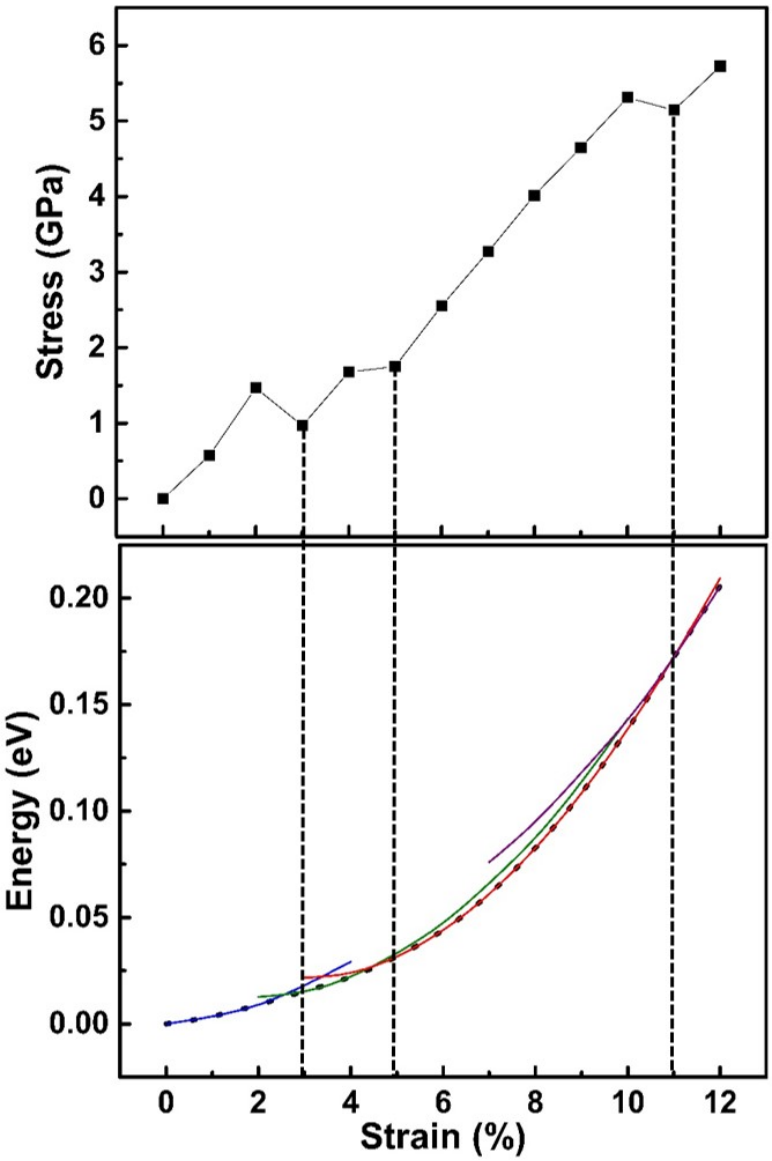

Figure 2.4: Calculated stress and total energy (per primitive unit cell and referenced to the zero-strain value) as function of strain in Li0.50CO along the *c*-direction.

The calculated atomic structures clearly show structural changes at 3%, 5%, and 11% upon which Li ions displace leading to the breaking of their symmetry. Calculated magnetic moment as a function of strain (Fig. 2.5) shows almost no variation.

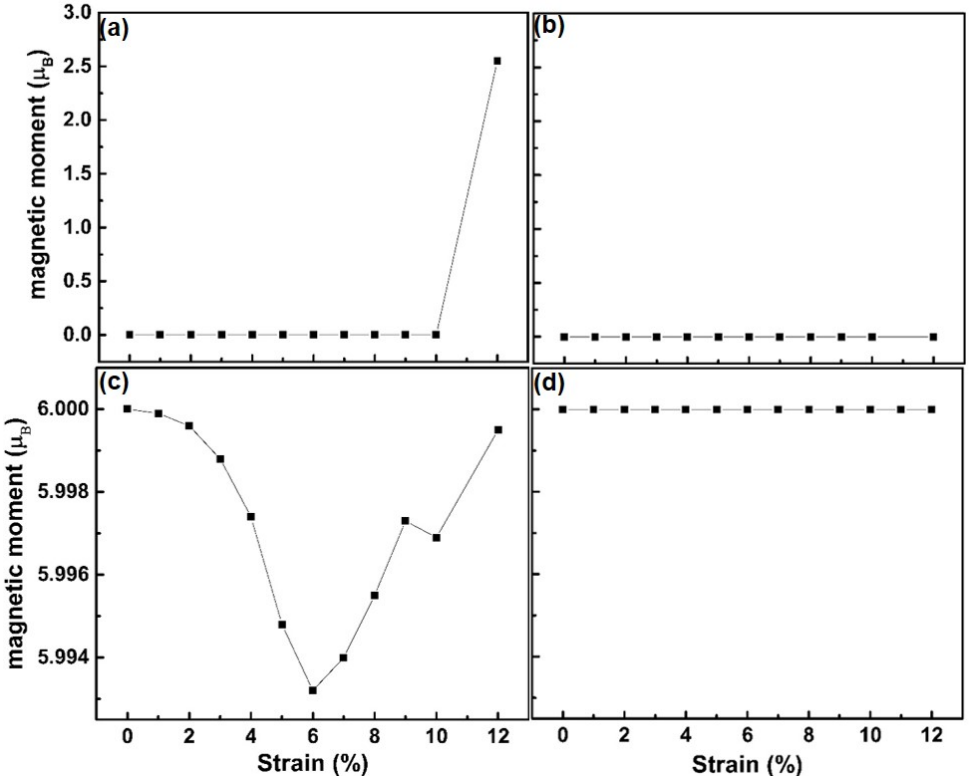

Figure 2.5: Magnetic moment versus strain for L1.00CO along the **(a)** *a*- and **(b)** *c*-direction as well as for L0.50CO along the **(c)** *a*- and **(d)** *c*-direction.

This indicates that phase transition is driven by the interlayer rather than intralayer O–TM–O interaction. The magnitude of delithiation-induced change in *c* is the determining factor for the critical strain above which restructuring occurs. For example, *c* contracts by 3.4% in L0.12CO with respect to L1.00CO. The computed stress as function of strain for $x = 0.12$ (Fig. 2.7) shows a phase transition for strain values larger than 6%.

The corresponding *c* value of this critical strain is, interestingly, very close the critical *c* value for phase transition in the case of L0.50CO. Displacement of Li-ions in L0.12CO is, however, not similar to that in L0.50CO (Fig. 2.7). This is due to the applied periodic boundary condition for the latter system. We also calculated stress as function of shearing (Fig. 2.7) in L0.50CO and found that shear strains cannot

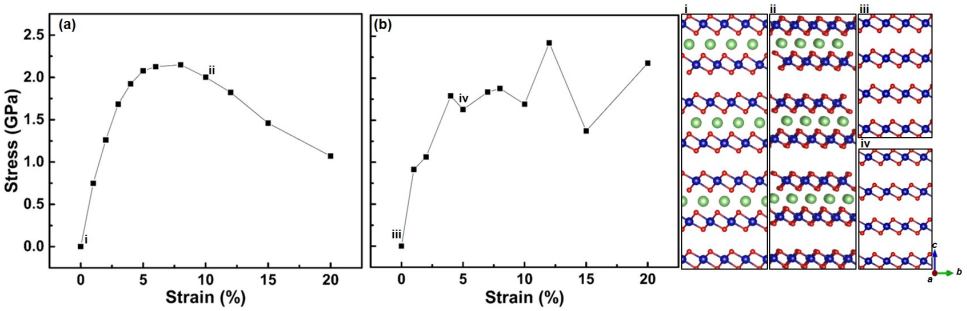

Figure 2.6: Stress versus strain for **(a)** L0.12CO and **(b)** CoO_2 along the c direction.

cause any considerable stress into the system. Hence, no displacements of Li ions are found in this case. However, the calculated stress as function of tensile strain along the c direction with an applied fixed shearing strain of 8% shows a similar behavior to the one that was found in Fig. 2.3.

The Li extraction of *x* = 1.0→0.5 leads to an electrochemically-induced tensile strain of ϵ_c = 2.39% and a compressive strain of ϵ_a = -0.23% (from the experimental data of Takahashi et al.[34]), but the Li displacement, which can lead to the cracking of a microstructure, occurs only if an additional elastic tensile strain 2% < ϵ_c is exerted along *c* in L0.50CO. This means that at least a ≈ 5% tensile strain along *c* in the L0.50CO system with respect to the equilibrium *c* of L1.00CO system is needed to form cracking in a LCO microstructure. Here, we discuss likely sources of additional

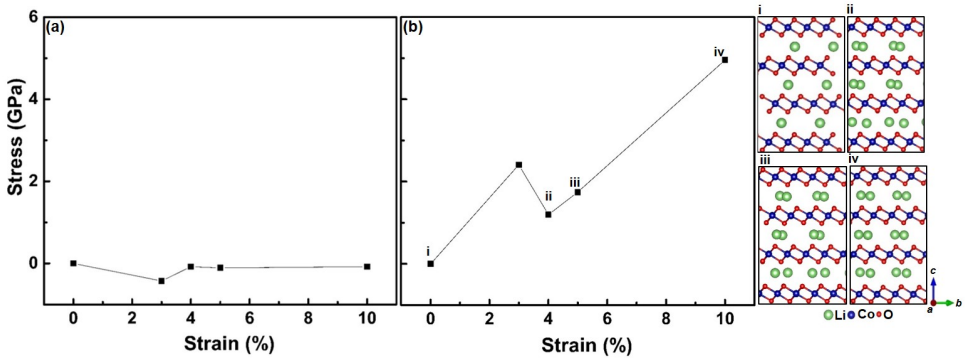

Figure 2.7: Calculated **(a)** shear as function of angle change in percentage and **(b)** tensile stress as function of strain along the *c*-direction with an applied fixed shearing strain of 8% in L0.50CO.

3% tensile strain: I) mechanical strain that arises in each particle of a microstructure from the lattice size change (expansion of *c* and contraction of *a*) of adjacent particles when *x* = 1.00→0.50, II) accumulation or depletion of Li ions in a single Li layer (i.e. sharp space charge), and III) point defects. In the following, we discuss these three possible sources of strains.

2.3.4 Microstructure

We modelled a typical microstructure with randomly oriented particles of arbitrary sizes and computed arising strain/stress due to a delithiation of *x* = 1.00→0.50 within it (see Fig. 2.8 and Fig. 2.9). The anisotropic stiffness matrix that is needed to compute stress/strain distributions in the microstructure was obtained from the DFT-PBE calculation [Tab. 2.1 and the method section for the details of our calculation]. Since our calculated lattice parameters are not much different from the experimental values, we used the corresponding experimental values from ref. 34. Our results show that elastic strains and stresses along *a* are equal to those along *b*, and they are ϵ_a= 0.36% $\pm$ 0.30 and σ_a = 0.59 $\pm$ 0.91 GPa, respectively. However, the corresponding values along the *c*-direction are ϵ_c= -0.94% $\pm$ 0.56 and σ_c =-1.2 $\pm$ 0.8 GPa, respectively. We found that maximum compressive and tensile strains along the *c*-direction are -2.22% and 0.51%, respectively. However, Fig.

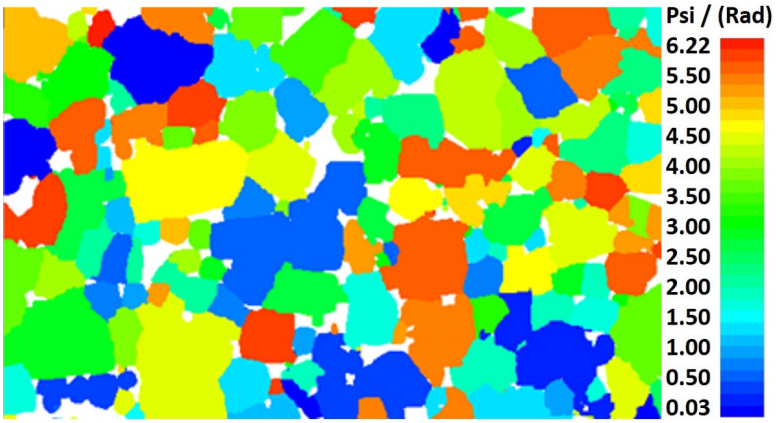

Figure 2.8: Modelled typical microstructure of LCO containing of randomly-oriented microparticles of arbitrary sizes.

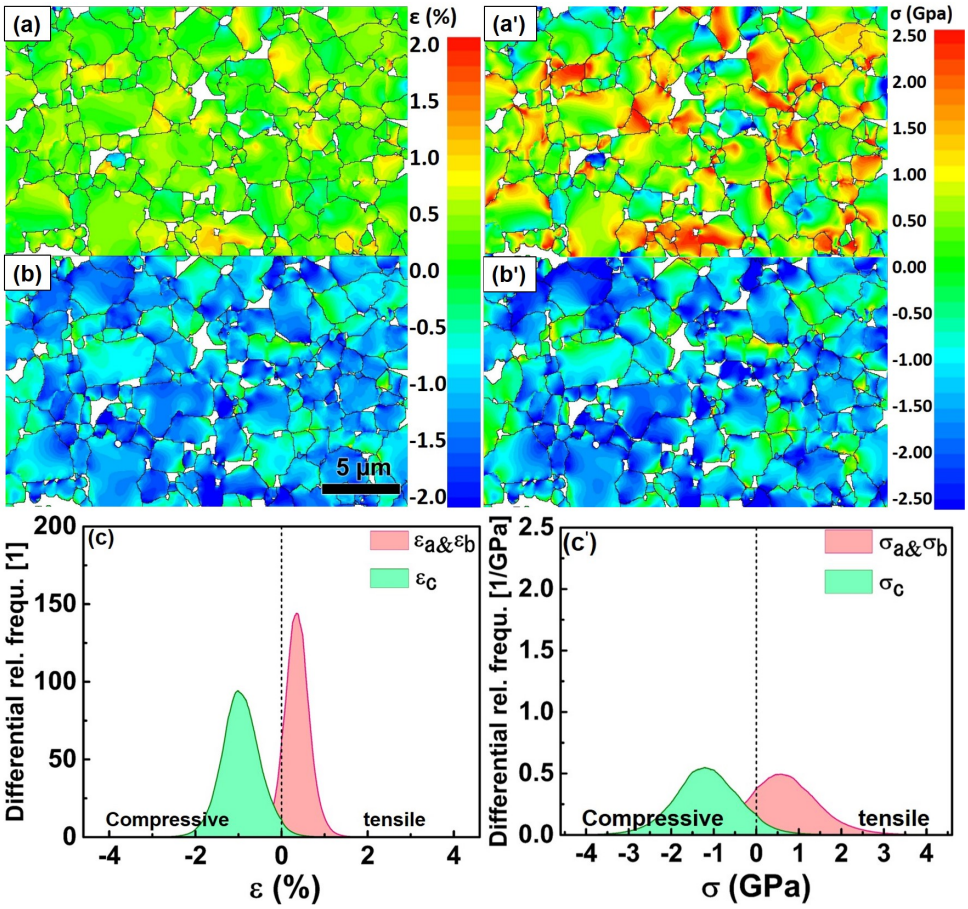

Figure 2.9: Calculated mechanical stress and strain in an arbitrary microstructure of L*x*CO induced by the delithiation of its particles from *x* = 1.00 to 0.50: strain distribution along the **(a)** *a*- and **(b)** *c*-direction as well as **(c)** strain histograms along *a*- and *c*-direction; stress distribution along the **(**$a^{'}$**)** *a*- and **(b**$^{'}$**)** *c*-direction as well as **(c**$^{'}$**)** stress histograms along the *a*- and *c*-direction. Fully lithiated particles in the microstructure were assumed to be in the stress- free state. Red and blue color in fig (a, b, a$^{'}$, b$^{'}$) represents the tensile and compressive strain, respectively. (For interpretation of the references to color in this figure legend, the reader is referred to the Web version of this article.)

2.3 indicates that tensile lattice strains ϵ_c larger than 2% can only lead to cracking. Hence, the delithiation-induced mechanical lattice strains in a microstructure cannot be responsible for an instantaneous failure but it might only cause subcritical crack growth leading to cracking over time.

2.3.5 Sharp space charge (SC)

To study extreme cases of space charge formation in grain boundaries, we considered a zero (SC0) or full occupation (SC1) of Li sites between two arbitrary adjacent O-Co-O layers. These two cases represent sharp SC areas with fully depleted and accumulated Li layers, respectively (Fig.2.10(a-b)). The interlayer separation (distance between Co layers $d_{\mathrm{Co-Co}}$) for the fully depleted part of the SC0 model is 4.75 Å, which is smaller than that for the CoO_2 system with a 1% strain (Figure 2.11). The interlayer separations for the L0.50CO layers in the SC0 model is 4.78-4.85 Å which are also smaller than those for the L0.50CO system with a homogenously distributed 0.50Li ions and 1% strain. Since the residual strains are less than 3% (i. e. the starting point of damage), no Li displacement is observed in this SC0 model. The calculated value of interlayer separation for the fully lithiated part of the SC1 system is 4.73 Å, which is very close to the computed value of 4.72 Å for the L1.00CO system with a 1% strain. The interlayer separations for the L0.50CO layer are comparable to the L0.50CO system with 0%-1% strains. Thus, no displacement

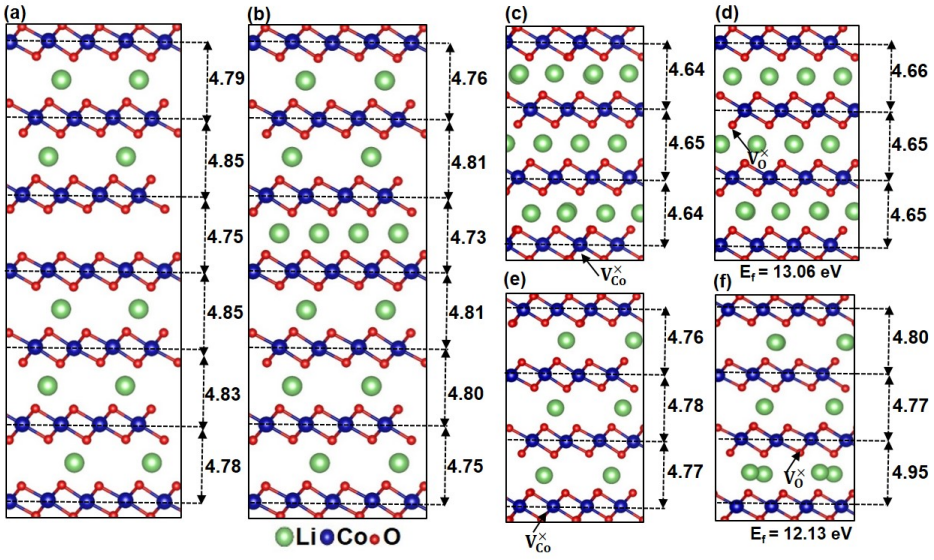

Figure 2.10: Calculated Co-Co interlayer separations in L0.50CO with a fully (a) delithiated and (b) lithiated Li layer modelling space charge regions. Calculated Co-Co interlayer separations in L1.00CO and L0.50CO with 4.17% (c,e) Co and (d,f) O vacancy.

of Li is observed for the SC1 model as well. Hence, we find that the space charge cannot be responsible for the microcracking. The calculated values of $d_{\mathrm{Co-Co}}$ in both defective d-L1.00CO systems are similar to those in the defect- free L1.00CO system with a 0% strain.

2.3.6 Point defect (Co and O vacancy)

We considered V_{Co}^{x} and V_{O}^{x} (neutral Co and O vacancy) in L1.00CO and L0.50CO, and calculated $d_{\mathrm{Co-Co}}$ (Fig. 2.10 (c-f). The calculated values of $d_{\mathrm{Co-Co}}$ in both defective d-L1.00CO systems are similar to those in the defect-free L1.00CO system with a 0% strain. The $d_{\mathrm{Co-Co}}$ distances for d-L0.50CO with V_{Co}^{x} are also comparable to those in the strain- and defect-free L0.50CO system. However, we find a 3% tensile strain in $d_{\mathrm{Co-Co}}$ in the d-L0.50CO structure in which a 4.17% V_{O}^{x} is present. Consequently, the Li ions between O–Co–O interlayers undergo displacements which are very similar to those in the defect-free L0.50CO with a 3% strain. This shows that the displacement of Li ions in the d- L0.50CO structure is only

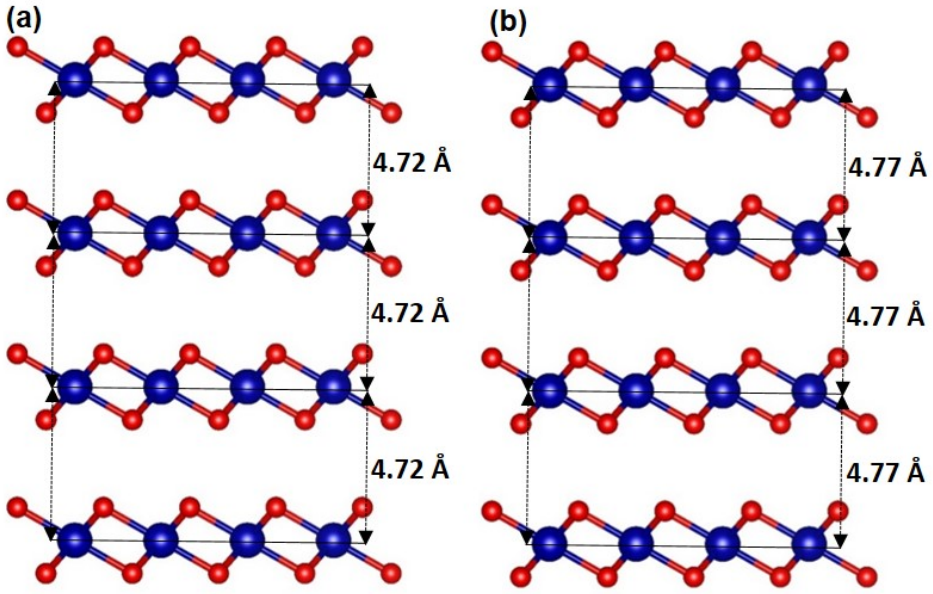

Figure 2.11: Calculated Co-Co interlayer separations in CoO_2 with (a) 0% strain and (b) 1% strain.

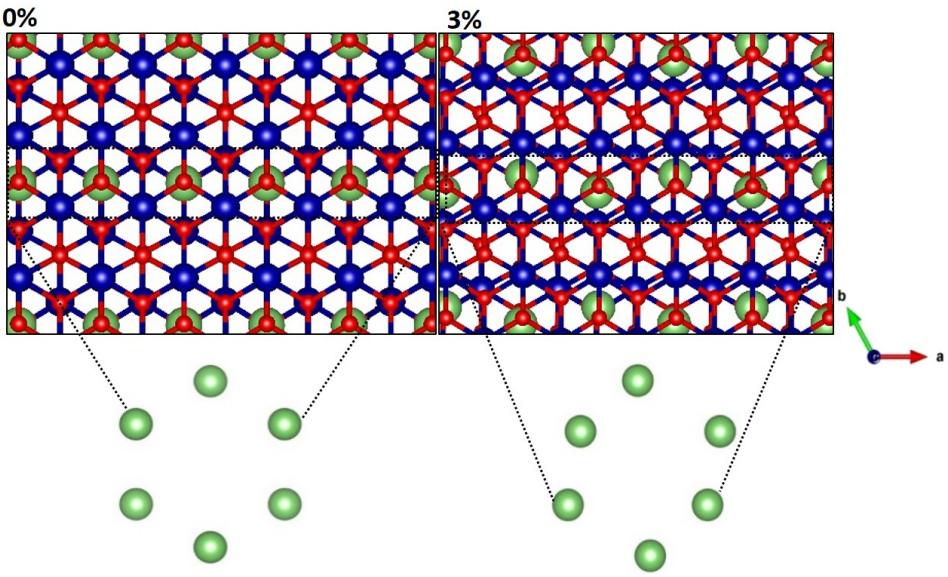

Figure 2.12: Calculated top view of atomic structures of L0.5CO for 0% strain and 3% strain.

due to the V_O^x-induced expansion of interlayer separation and not a direct V_O^x-Li interaction. The calculated formation energy of V_O^x is more favourable by 0.93 eV in d-L0.50CO compared to d-L1.00CO. This shows that an increase in the density of O vacancy in the LCO lattice by delithiation (i.e. cycling) can lead to displacements of Li ions and microcracking of LCO cathodes[35].

2.4 Conclusions

In this work, by performing DFT calculation and microstructural mechanical analysis, we investigated the origin of microcracking in LCO. It was found that the defective bulk LCO with O or Co vacancies is softer than its pristine counterpart. Consequently, the mechanical properties of former systems are closer to the experimental measurements. A structural phase transition on the atomic scale (i.e. displacements of Li ions) occurs when a tensile uniaxial strain larger than 2% along the *c*-direction (ϵ_c) is exerted on a defect-free $Li_{0.50}CoO_2$. A similar phase transition is also obtained for $Li_{0.12}CoO_2$ experiencing ϵ_c > 6% or c > 14.80 Å. The critical value of *c* above which Li movement occurs is similar in $Li_{0.12}CoO_2$ and $Li_{0.50}CoO_2$. Fur-

thermore, we performed a mechanical GeoDict simulation on an arbitrary cathode microstructure comprising of randomly-distributed L0.50CO particles. It was found that the maximum possible strain (with respect to the strain-free L1.00CO particles) along the *c*-direction arising from a half delithiation is less than 0.5%. Moreover, our DFT calculation indicates that a heterogeneous distribution of Li ions between O-Co-O layers, representing a space charge region for example at grain boundaries, cannot lead to a large local tensile strain or restructuring. However, the presence of 4.17% of O vacancy causes a large strain of ϵ_c= 3% leading to the displacements of Li ions. It is known that operating LCO cathodes experience a release of O anions from their lattices. We, therefore, proposed that the delithiation-induced O vacancy formation might be the initial stage of microcracking of LCO and most likely in the other layered cathode materials.

2.5 References

1. K.J. Mizushima, P.C. Jones, P.J. Wiseman, J.B. Goodenough, Mater. Res. Bull. 15 (1980) 783–789.
2. B. Huang, Y.I. Jang, Y.M. Chiang, D.R. Sadoway, J. Appl. Electrochem. 28 (1998) 1365–1369.
3. Z. Chen, Z. Lu, J.R. Dahn, J. Electrochem. Soc. 149 (2002), A1604.
4. H. Wang, Y. Jang, I. Huang, B. Sadoway, J. Electrochem. Soc. 146 (1999) 473–480.
5. W.S. Yoon, K.B. Kim, M.G. Kim, M.K. Lee, H.J. Shin, J.M. Lee, J.S. Lee, C.H. Yo, J. Phys. Chem. B 106 (2002) 2526–2532.
6. Y.N. Zhou, J. Ma, E. Hu, X. Yu, L. Gu, K.W. Nam, L. Chen, Z. Wang, X.Q. Yang, Nat. Commun. 5 (2014) 1–8.
7. G.G. Amatucci, J.M. Tarascon, L.C. Klein, J. Electrochem. Soc. 143 (1996) 1114.
8. T. Ohzuku, A. Ueda, J. Electrochem. Soc. 141 (1994) 2972.
9. M. Qu, W.H. Woodford, J.M. Maloney, W.C. Carter, Y.M. Chiang, V. Vliet, Adv. Energy Mater. 2 (2012) 940–944.
10. E.J. Cheng, N.J. Taylor, J. Wolfenstine, Sakamoto, J. Asian Ceram. Soc. 5 (2017) 113–117.
11. L. Feng, X. Lu, T. Zhao, Dillon, J. Am. Ceram. Soc. 102 (2019) 372–381.
12. Van der Ven, A. Aydinol, M.K. Ceder, G. Kresse, G. Hafner, Phys. Rev. B 58 (1998) 2975.
13. Y. Qi, Hector Jr., L.G. James, C. Kim, J. Electrochem. Soc. 161 (2014) F3010–F3018.
14. L. Wu, Zhang, J. Appl. Phys. 118 (2015), 225101.
15. A. Chakraborty, M. Dixit, D. Aurbach, D.T. Major, npj Comput. Mater. 4 (2018) 1–9.
16. P.E. Blochl, ¨ Phys. Rev. B 50 (1994) 17953–17979.

17. G. Kresse, J. Furthmüller, Phys. Rev. B 54 (1996) 11169–11186.

18. J.P. Perdew, K. Burke, M. Ernzerhof, Phys. Rev. Lett. 77 (1996) 3865–3868.

19. S.L. Dudarev, G.A. Botton, S.Y. Savrasov, C.J. Humphreys, A.P. Sutton, Phys. Rev. B 57 (1998) 1505–1509.

20. L.Y. Kuo, O. Guillon, P. Kaghazchi, J. Mater. Chem. 8 (2020) 13832–13841.

21. S. Grimme, J. Antony, S. Ehrlich, H. Krieg, J. Chem. Phys. 132 (2010), 154104.

22. D.H. Chung, W.R. Buessem, J. Appl. Phys. 38 (6) (1967) 2535–2540.

23. K. Okhotnikov, T. Charpentier, Cadars, J. Cheminf. 8 (2016) 1–15.

24. K. Momma, F. Izumi, J. Appl. Crystallogr. 44 (2011) 1272–1276.

25. R. Mücke, M. Finsterbusch, P. Kaghazchi, D. Fatakowa-Rohlfing, O. Guillon, J. Power Sources 489 (2021), 229430.

26. H. Moulinec, P. Suquet, Comput. Methods Appl. Mech. Eng. 157 (1998) 69–94.

27. M. Schneider, F. Ospald, M. Kabel, Int. J. Numer. Methods Eng. 105 (2016) 693–720.

28. R. Elango, A. Demorti‘ere, V. De Andrade, M. Morcrette, V. Seznec, Adv. Energy Mater. 8 (2018), 1703031.

29. M. Qu, W.H. Woodford, J.M. Maloney, W.C. Carter, Y.M. Chiang, K.J. Van Vliet, Adv. Energy Mater. 2 (2012) 940–944.

30. E.J. Cheng, N.J. Taylor, J. Wolfenstine, Sakamoto, J. Asian Ceram. Soc. 5 (2017) 113–117.

31. X. Wang, I. Loa, K. Kunc, Syassen, K. Amboage, Phys. Rev. B 72 (2005), 224102.

32. S. Yamakawa, N. Nagasako, H. Yamasaki, T. Koyama, R. Asahi, Solid State Ionics 319 (2018) 209–217.

33. P. Yan, J. Zheng, M. Gu, J. Xiao, J.G. Zhang, C.M. Wang, Nat. Commun. 8 (2017) 1–9.

34. Y. Takahashi, N. Kijima, K. Dokko, M. Nishizawa, I. Uchida, J. Akimoto, J. Solid State Chem. 180 (2007) 313–321.

35. C. Sun, X. Liao, F. Xia, Y. Zhao, L. Zhang, S. Mu, S. Shi, Y. Li, H. Peng, G. Van Tendeloo, K. Zhao, ACS Nano 5 (2020) 6181–6190.

3

Impact of co-doping of Li and Co/Ni on P2-Na_xMnO_2 cathode for sodium-ion batteries

Abstract: Oxygen-redox-based-layered cathode materials are of great importance in realizing high-energy-density sodium-ion batteries (SIBs) that can satisfy the demands of next-generation energy storage technologies. However, P2-Na_xMnO_2, an oxygen-redox cathode material, suffers from fast capacity fading and structural instability during the charging and discharging process. In this work, a combination of Coulomb energy analysis and DFT calculations was used to study the influence of Li, Co/Ni doping on the stability and redox mechanism of P2-Na_xMnO_2 cathodes. We characterized the redox mechanism by computing the magnetic moments and spin density differences. It is demonstrated that the efficacy of the co-doping of Li and Co in P2-Na_xMnO_2 i.e. $Na_{0.75}[Li_{0.156}Co_{0.156}Mn_{0.689}]O_2$ improves the structural and cycling stability despite the reversible Li migration from the transition metal layer during de-/sodiation. Moreover, it is found that the co-doping of Li and Ni in P2-Na_xMnO_2 improves structural stability by reducing Li migration from transition metal to Na layers. Our study shows that Ni suppresses the O redox, but due to the higher structural stability and Ni-redox activity, $Na_{0.75}[Li_{0.14}Ni_{0.17}Mn_{0.69}]O_2$ has a better performance in comparison to $Na_{0.67}[Li_{0.22}Mn_{0.78}]O_2$. Overall, our finding demonstrates that the presence of co-doping played important roles in the structural stability, thereby improving the electrode performance via both TM and O redox.

3.1 Introduction

Lithium-ion batteries (LIBs) are considered one of the most efficient types of rechargeable batteries for mobile electronics and electric vehicles owing to their high energy density and reasonable cyclability. As increasingly more devices require LIBs as power sources, it is necessary to search for alternatives to replace expensive lithium resources and reduce the cost of batteries. Among several candidates[1–3], the use of sodium-ion batteries (SIBs) has been shown to be particularly promising because of the even and abundant distribution of sodium resources on the earth's surface. Because of the large ionic size of sodium $(1.02$ Å$)$ relative to that of lithium $(0.76$ Å$)$, sodium transition metal (TM) oxides are typically stabilized into a layer structure[4–6]. The chemistry of sodium is particularly good with manganese in the oxide matrix, for example, Na_xMnO_2[7]; hence, the combination of earth-abundant elements is anticipated to further enhance the price merit of SIBs, provided that the performance is compatible with that of high-energy-density Ni-rich cathode materials for LIBs.

Notwithstanding, there is an intrinsic demerit of SIBs, namely, the low operation voltage stemming from the high standard electrode potential of sodium metal (Na^+/Na: -2.7 V vs. standard hydrogen electrode (SHE)) compared with that of lithium metal (Li^+/Li: -3.04 V vs. SHE). To resolve this issue and for SIBs to compete with LIBs, the inherent disadvantage should be overcome by increasing the capacity as high as possible to achieve high energy density at a similar level as that of Ni-rich cathode materials for LIBs.

The above-mentioned cathode materials are solely activated via a cationic redox process; hence, there is a capacity limit attributed to the TM elements. The role of participating anions in the electrochemical reaction to deliver additional capacity

This chapter is based on the theory part of the following publications:
N. Voronina, M.Y. Shin, H.J. Kim, N. Yaqoob, O. Guillon, S.H. Song, H. Kim,... & P. Kaghazchi, S.T. Myung, Advanced energy materials, 2022, 12, 2103939.
N. Voronina, J. H. Yu, H.J. Kim, N. Yaqoob, O. Guillon, H. Kim, ... & S.T. Myung, Advanced Functional Materials, 2023, 5, 2210423.

was thus investigated, for example, oxidation of O^{2-} to $(O_2)^{n-}$ and vice versa on reduction in oxide matrices for layered compounds. Earlier works have demonstrated the validity of oxygen-redox reactions on Li-rich cathodes such as $Li[Li_xTM_{1-x}]O_2$ in Li cells[8–10]. Interestingly, such oxygen behavior is also applicable to not only Na-rich cathodes[11–13], which are an analogue of Li-rich materials, but also Na-deficient TM oxides[14–21].

The Na-rich compounds are mainly based on noble and expensive TMs, such as 4*d* (Ru) and 5*d* (Ir) metals [22–24]; however, Na-deficient materials (P2 and P3) are represented by abundant and low-cost 3*d* (Mn)[15,16]. There is a universal notation for oxygen redox: $Na_x[A_yTM_{1-y}]O_2$, where TM is Mn[14–20], Ru[21,25,26], or Ir[23,27,28], and A is monovalent Li[14,17,18,29,30] or divalent Mg[20,31–33] or Zn[34,35]. In this case, oxygen-redox activity is usually triggered by the presence of the Na–O–A configuration that forms lone-pair electrons in the O 2*p* orbital, which allows subsequent oxidation of O^{2-} to $(O_2)^{n-}$ in the bulk of cathode materials on desodiation and vice versa on sodiation. Yabuuchi et al.[17] introduced the first work on Li substitution at the Mn site in P2 $Na_{5/6}[Li_{1/4}Mn^{3.89+}{}_{3/4}]O_2$, delivering a discharge capacity of approximately 180 mAh g^{-1} with suppressed phase transition through rearrangement of cations after extraction of oxygen on a long voltage plateau over 3.5 V. Later work by de la Llave et al.[18] demonstrated that the density of states of P2-$Na_{0.6}[Li_{0.2}Mn^{4+}{}_{0.8}]O_2$ for oxygen lying close to the Fermi-energy level indicates that oxygen is a possible redox center.

In addition, the Li in the TM layers played an important role in improving the structure stability compared with that of P2-$Na_{0.6}MnO_2$. Rong et al.[36] investigated P2-$Na_{0.72}[Li_{0.24}Mn^{4+}{}_{0.76}]O_2$, which delivered a high discharge capacity of approximately 270 mAh g^{-1}, with extraction of all the sodium from the host structure with a charge capacity of 210 mAh g^{-1}. This property was attributed to the structural stability that maintained the P2 phase, though few small O2 phase domains were formed at the nanoscale when deeply charged during electrochemical reaction enabled by Mn^{4+}/Mn^{3+} and $O^{2-}/(O_2)^{n-}$ redox pairs. Density functional theory calculation provides further insight for understanding the behavior of oxygen in these

compounds. According to the calculation on $Na_{1-x}[Li_{1/3}Mn_{2/3}{}^{4+}]O_2$ by Kim et al.[37], the O $2p$ electron is oxidized to compensate for the charge imbalance, and a vacancy was observed around the oxidized O $2p$ electron. This finding indicates a linear increase as oxidation of oxygen further progressed. The above-mentioned theoretical phenomena were experimentally confirmed in P2-$Na_{0.6}[Li_{0.2}Mn_{0.8}]O_2$[38]. Moreover, Dahn et al.[39] reported P2-$Na_{0.67}[Ni_{0.33}Mn_{0.67}]O_2$ with high capacity (173 $mAhg^{-1}$) and high operating voltage over 3.5 V in Na cells. However, the cyclability suffered as a result of the P2–O2 phase transformation, resulting in ≈23% volume change in unit cells in the highly desodiated state. Later, Konarov et al.[40] reduced the volume change to ≈13% by optimizing the Ni content in $Na_{0.67}[Ni_{0.2}Mn_{0.8}]O_2$, showing an acceptable level of capacity retention.Compared with P2-$Na_{0.7}MnO_2$, the suppression of Jahn–Teller distortion via Ni^{2+} incorporation is also worth mentioning as an approach to retain the capacity. Yabuuchi and Komaba et al.[41] stabilized the P2 layered structure by replacing half of the Mn^{3+} with Fe^{3+}, P2-$Na_{0.67}[Fe_{0.5}Mn_{0.5}]O_2$, which delivered a capacity of 190 $mAhg^{-1}$ with good reversibility assisted by both Mn^{4+}/Mn^{3+} and Fe^{4+}/Fe^{3+} redox pairs. Konarov et al.[42] also introduced Co^{3+} into P2-$Na_{0.7}MnO_2$ to dilute the Jahn–Teller effect, showing good electrode performance.

The above works highlight the importance of substituents to stabilize the structure from the existing Jahn–Teller effect in a deeply discharged state and suppression of volume change in unit cells during repetitive de/sodiation.

In this work, we studied the impact of Li and Co/Ni doping on P2-type Na_xMnO_2 cathodes for Na-ion battery. Therefore, we focused on the chemical composition of three materials: $Na_{0.67}[Li_{0.22}Mn_{0.78}]O_2$ (LM), $Na_{0.75}[Li_{0.156}Co_{0.156}Mn_{0.689}]O_2$ (LCM) and $Na_{0.75}[Li_{0.14}Ni_{0.17}Mn_{0.69}]O_2$ (LNM). These materials are crystallized into the P2-type layered structure.

3.2 Computational Details

Spin-polarized DFT calculations were performed using the projector augmented wave (PAW) potential method[43] implemented in the Vienna *Ab Initio* Simulation

Package (VASP) code.[44] Generalized gradient approximation (GGA) within the scheme of Perdew–Burke–Ernzerhof (PBE)[45] was used as the basis of the exchange-correlation (XC) functional. The Hubbard correction proposed by Dudarev et al.[46] (*U-J* is simply presented by *U* hereafter) was considered to compute the lattice parameters and electronic structures for LM and LNM systems.

We checked a variety of possible *U* values for both Ni and Mn: *U*(Ni)=5.0 eV and *U*(Mn)=4.0 eV, *U*(Ni)=6.8 eV and *U*(Mn)=2.0 eV, *U*(Ni)=6.8 eV and *U*(Mn)=2.5 eV, *U*(Ni)=6.8 eV and *U*(Mn)=3.0 eV, *U*(Ni)=6.8 eV and *U*(Mn)=4.0 eV, *U*(Ni)=6.8 eV and *U*(Mn)=5.2 eV, and *U*(Ni)=9.0 eV and *U*(Mn)=7.0 eV. The computed lattice parameters change with delithiation agrees well with our experimental data with *U*(Ni)=6.8 eV and *U*(Mn)=3.0 eV. The Hubbard *U* correction with the *U* values of 5.9 eV and 5.2 eV for Co and Mn, respectively, was considered to compute the atomistic structures for LCM. However, we used the Heyd–Scuseria–Ernzerhof (HSE06)[47] functional to compute the electronic structure (i.e. number of unpaired electrons (N_{unp}) on elements and spin density differences) for LCM.

To perform the Coulomb energy analysis and DFT calculations, we modeled LM and LNM structures with a supercell of 3×6×1 with the following number of atoms per supercell: P2-$Na_{0.67}Li_{0.22}Mn_{0.78}O_2$ ($Na_{24}Li_8Mn_{28}O_{72}$), P2-$Na_{0.11}Li_{0.22}Mn_{0.78}O_2$ ($Na_4Li_8Mn_{28}O_{72}$), P2-$Na_{0.75}Li_{0.14}Ni_{0.17}Mn_{0.69}O_2$ ($Na_{27}Li_5Ni_6Mn_{25}O_{72}$), and P2-$Na_{0.22}Li_{0.14}Ni_{0.17}Mn_{0.69}O_2$ ($Na_8Li_5Ni_6Mn_{25}O_{72}$). The discharged and charged systems were modeled by 4×4×1 supercells for LCM with the following number of atoms: $Na_{0.75}Li_{0.156}Co_{0.156}Mn_{0.689}O_2$ ($Na_{24}Li_5Co_5Mn_{22}O_{64}$), $Na_{0.125}Li_{0.156}Co_{0.156}Mn_{0.689}O_2$ ($Na_4Li_5Co_5Mn_{22}O_{64}$),.

A *k*-point mesh of 2×1×2 for LM, LNM and 2×2×2 for LCM with an energy cut-off of 500 eV and 550 eV were applied for LM, LNM and LCM respectively. Electronic and force convergence criteria of 10^{-4} eV and 10^{-3} eV/Å, respectively, were considered for all DFT calculations. Total Coulomb energy calculations on possible combinations were carried out using the so-called supercell code[48]. Atomistic structures and spin density differences SDD were visualized with the VESTA program[49].

To find the most favorable structures of P2-Na$_x$Li$_{0.22}$Mn$_{0.78}$O$_2$, P2-Na$_x$Li$_{0.156}$Co$_{0.156}$Mn$_{0.689}$O$_2$ and P2-Na$_x$Li$_{0.14}$Ni$_{0.17}$Mn$_{0.69}$O$_2$ with different *x* values, we modeled and calculated the total Coulomb energy (E_C) of a large number of likely structures. By performing DFT-PBE calculation on the electrostatically most favorable configuration, we determined the lowest total energy structure for each Na concentration and used the optimized geometries for further DFT-PBE+*U* and -HSE06 calculations. The total number of considered configurations for E_C calculation and the charge states of ions for each *x* value are as follows.

Na$_{0.67}$[Li$_{0.22}$Mn$_{0.78}$]O$_2$ (Na$_{24}$Li$_8$Mn$_{28}$O$_{72}$): To obtain the most favorable distribution of Na, Mn, and Li ions in Na$_{0.67}$[Li$_{0.22}$Mn$_{0.78}$]O$_2$ (modelled by the Na$_{24}$Li$_8$Mn$_{28}$O$_{72}$), we had to use a 3-step process since the creation of structures and calculation of their total Coulomb Energies (E_C) for all possible configurations with 24 Na ions in 36 Na sites as well as 28 Mn and 8 Li ions in 36 Mn sites, namely $\frac{36!}{24!12!} \cdot \frac{36!}{28!8!}$= 3.78762E+16, were computationally intractable. At first, we fixed 36 Mn cations at 36 TM-sites and found the distribution of 24 Na ions in 36 Na sites. We created $\frac{36!}{24!12!}$ = 1251677700 structures. For charge balancing, we used 1+ for Na, 3.333+ for Mn and 2$-$ for O. After determining the structure with the lowest E_C, we kept fixed Na-ions in the determined Na sites, and studied distribution of 28 Mn ions in 36 Mn sites by creating $\frac{36!}{28!8!}$= 30260340 structures. To find the position of 8 Li ions in Na$_{36}$Mn$_{36}$O$_{72}$, we fixed 24 Na and 28 Mn ions in their determined Na and Mn sites and studied Li distribution in the remaining unoccupied Na and Mn-sites. We performed Coulomb energy analysis on 3 possible distributions: i) all Li-ions in Mn-sites ii) all Li-ions in Na-sites, and iii) half Li-ions in Na sites and half in Mn-sites. For charge balancing, the following charge states were applied: 1+ for Na, 1+ for Li, 4.0+ for Mn, and 2$-$ for O. The first distribution type was found to be favorable based on electrostatic analysis.

Na$_{0.11}$[Li$_{0.22}$Mn$_{0.78}$]O$_2$ (Na$_4$Li$_8$Mn$_{28}$O$_{72}$): We used the Na$_{0.67}$[Li$_{0.22}$Mn$_{0.78}$]O$_2$ Na$_{24}$Li$_8$Mn$_{28}$O$_{72}$) to find Na distribution in Na$_{0.11}$[Li$_{0.22}$Mn$_{0.78}$]O$_2$ (Na$_4$Li$_8$Mn$_{28}$O$_{72}$). We considered all possible configurations for 4 Na ions in 24 Na sites and we created a total number $\frac{24!}{4!20!}$= 10626 structures. For charge balancing, we used

charges of 1+ for Na/Li, 4+ for Mn, and 1.72$-$ for O.

$Na_{0.75}[Li_{0.14}Ni_{0.17}Mn_{0.69}]O_2$ ($Na_{27}Li_5Ni_6Mn_{25}O_{72}$): To model this structure, we also had to use a 3 step process because calculation of E_C for all possible configurations with 27 Na ions in 36 Na sites as well as 25 Mn ions, 5 Li ions, and 6 Ni ions in 36 Mn sites, namely $\frac{36!}{27!9!} \cdot \frac{36!}{25!11!} \cdot \frac{11!}{6!5!}$ = 2.61315E+19, was computationally intractable. Therefore, we had to fix 36 Mn cations at 36 TM-sites and find all possible configurations with 27 Na ions in 36 Na sites, namely $\frac{36!}{27!9!}$ = 94143280 structures. The charge states of Na, Mn, and O were considered to be 1+, 3.25+, and 2$-$, respectively. We obtained the lowest E_C structure and then fixed Na-ions in their determined Na sites, and afterwards we determined the distribution of 25 Mn ions in 36 Mn sites, $\frac{36!}{25!11!}$ = 600805296 structures. To find the arrangement of 5 Li ions and 6 Ni ions in $Na_{36}Mn_{36}O_{72}$, we, then, fixed the 27 Na and 25 Mn ions in their determined sites and studied Li and Ni–arrangement in remaining Na and Mn-sites with creating $\frac{20!}{6!14!} \cdot \frac{14!}{5!9!}$ = 77597520 structures. We used the charge states of 1+ for Na/Li, 2+ for Ni, 4+ for Mn and 2$-$ for O.

$Na_{0.22}[Li_{0.14}Ni_{0.17}Mn_{0.69}]O_2$ ($Na_8Li_5Ni_6Mn_{25}O_{72}$): We used $Na_{0.75}[Li_{0.14}Ni_{0.17}Mn_{0.69}]O_2$ ($Na_{27}Li_5Ni_6Mn_{25}O_{72}$) structures to find Na arrangement in $Na_{0.22}[Li_{0.14}Ni_{0.17}Mn_{0.69}]O_2$ ($Na_8Li_5Ni_6Mn_{25}O_{72}$). We modelled all possible configurations, namely $\frac{27!}{8!19!}$ = 2220075, for 8 Na ions in 27 Na sites and calculated their E_C using charges of 1+ for Li/Na, 4+ for Mn/Ni, and 1.90$-$ for O. Then we performed DFT-PBE calculation on i) the structure with the lowest E_C value in which 5 Na occupy every second Na layer and the rest 3 Na ions occupy the other layers as well as ii) a structure with the same number of Na ions at each Na layer. We found that the latter one has a lower total energy and, finally, we focused on this structure for further DFT-PBE+*U* study.

$Na_{0.75}[Li_{0.156}Co_{0.156}Mn_{0.689}]O_2$ ($Na_{24}Li_5Co_5Mn_{22}O_{64}$): Modeling of $\frac{32!}{24!8!} \cdot \frac{32!}{27!5!} \cdot \frac{27!}{22!5!}$ = 1.71+17 structures for 24 Na ions in 32 Na sites as well as 5 Li ions, 5 Co ions, and 22 Mn ions in 32 TM sites was computationally intractable. Therefore, we first considered that all TM-sites are occupied by Mn and studied the occupation of 24 out of 32 Na sites by Na by modeling $\frac{32!}{24!8!}$ = 10518300

structures with charges of 1+ for Na, 3.25+ for Mn, and 2− for O. After determining the electrostatically most favorable structure, we fixed the position of Na ions and studied the occupation of 32 TM sites by 5 Co and 27 Mn cations by modeling $\frac{32!}{5!27!}$= 201376 structures. The charge states of Na, Co, Mn and O ions were considered to be 1+, 3+, 3.30+, and 2−, respectively. To find the position of Li ions we fixed 24 Na ions and 5 Co ions in their determined favorable sites and studied occupation of 27 TM sites by 22 Mn and 5 Li ions by modeling $\frac{27!}{5!22!}$= 80730 structures with charge states of 1+ for Na/Li, 3.0+ for Co, 3.81+ for Mn, and 2− for O.

$Na_{0.125}$[$Li_{0.156}Co_{0.156}Mn_{0.689}$]$O_2$ ($Na_4Li_5Co_5Mn_{22}O_{64}$): $\frac{24!}{4!20!}$= 80730 structures with 4 Na ions in 24 Na sites with a charge of 1+ for Li/Na, 4+ for Co/Mn, and −1.828 for O were modelled.

3.3 Results and discussions

3.3.1 Atomistic structures and lattice parameters variation

Using density functional theory (DFT) calculation, we simulated the effect of Co and Ni on the structural stability of Li ions in the lattice and redox mechanism of LM cathodes. The atomistic structures of

Table 3.1: Calculated lattice parameters and volume as well as O-TM-O intralayer ($d1$) and interlayer ($d2$) distances using DFT: unit (*a*, *c*, $d1$ and $d2$: Å)

System	*a*	*c*	d**1**	d**2**
$Na_{0.67}Li_{0.22}Mn_{0.78}O_2$	2.90	11.00	2.07	3.43
$Na_{0.11}Li_{0.11}Mn_{0.78}O_2$	2.89	10.98	2.00	3.49
$Na_{0.75}Li_{0.156}Co_{0.156}Mn_{0.689}O_2$	2.96	11.01	2.10	3.41
$Na_{0.125}Li_{0.156}Co_{0.156}Mn_{0.689}O_2$	2.89	10.70	1.98	3.18
$Na_{0.125}Co_{0.156}Mn_{0.689}O_2$	2.89	11.42	1.97	3.54
$Na_{0.75}Li_{0.14}Ni_{0.17}Mn_{0.69}O_2$	2.93	10.97	2.09	3.40
$Na_{0.22}Li_{0.14}Ni_{0.17}Mn_{0.69}O_2$	2.87	11.27	1.99	3.64

$Na_{0.67}Li_{0.22}Mn_{0.78}O_2$, $Na_{0.11}Li_{0.22}Mn_{0.78}O_2$, $Na_{0.75}Li_{0.156}Co_{0.156}Mn_{0.689}O_2$, $Na_{0.125}Li_{0.156}Co_{0.156}Mn_{0.689}O_2$, $Na_{0.75}Li_{0.14}Ni_{0.17}Mn_{0.69}O_2$ and $Na_{0.22}Li_{0.14}Ni_{0.17}Mn_{0.69}O_2$ (Fig. 3.1) were determined by performing an extensive set of Coulombic energy and DFT calculations. The computed lattice parameters indicate a very small decrease in the *a*-axis parameter (from 2.90 Å to 2.89 Å) and *c*-axis parameter (from 11.00 Å to 10.98 Å) for $Na_xLi_{0.22}Mn_{0.78}O_2$ when x=0.67 $\rightarrow$ 0.11 (Table 3.1). The former trend is most likely due to the extraction of Na+ and weakening of Na–Na repulsive interaction along the *a*-axis direction. However, the computed decrease in the c-axis value is not consistent with experiment Fig. 3.2. The reasons behind this may be as follows. i) The desodiation-induced small change in the c-axis, which is observed in experiment and computed with DFT, might lie within the uncertainty of both methods.

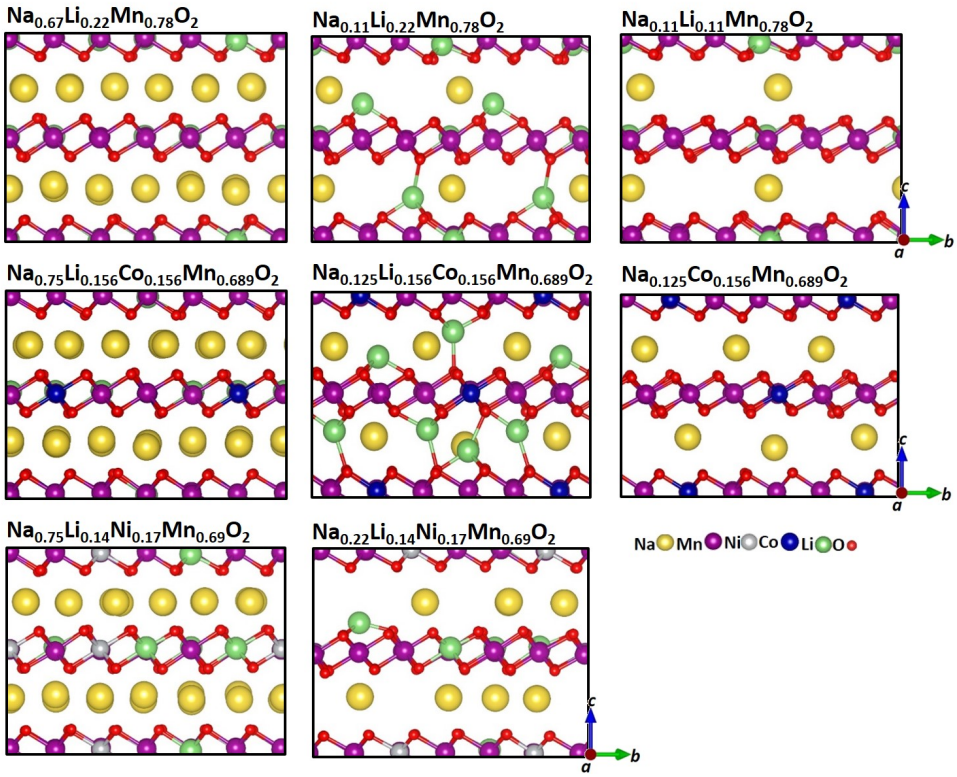

Figure 3.1: Calculated atomistic structures of LM, LCM and LNM before and after desodiation using DFT. Na, Li, Mn, Co, Ni, and O are in yellow, green, purple, blue, gray and red, respectively.

ii) The migration of Li ions from TM to Na sites followed by their segregation to the surface of the cathode, can increase the c-axis value such that the computed c-axis value becomes larger with desodiation, in line with experimental result (Fig. 3.2). Process ii) will be discussed in detail later.

For the Co-doped system, computed lattice parameters indicate that the *a*-axis parameter also decreases from 2.96 to 2.89 Å, and relatively large decrease in the *c*-axis parameter (from 11.01 to 10.70 Å). The decrease in the *a*-axis after desodiation stems from the oxidation of the TM. However, the computed decrease in the *c*-value originates from the spontaneous migration of Li ions from TM to Na sites during geometry optimization. The computed contraction of *c* agrees well with the data from our experimental project partner for the first charge (Figure 3.2).

To find whether the migrated Li ions from TM sites to Na sites move to the cathode surface or stay at Na sites after charge, we removed the Li

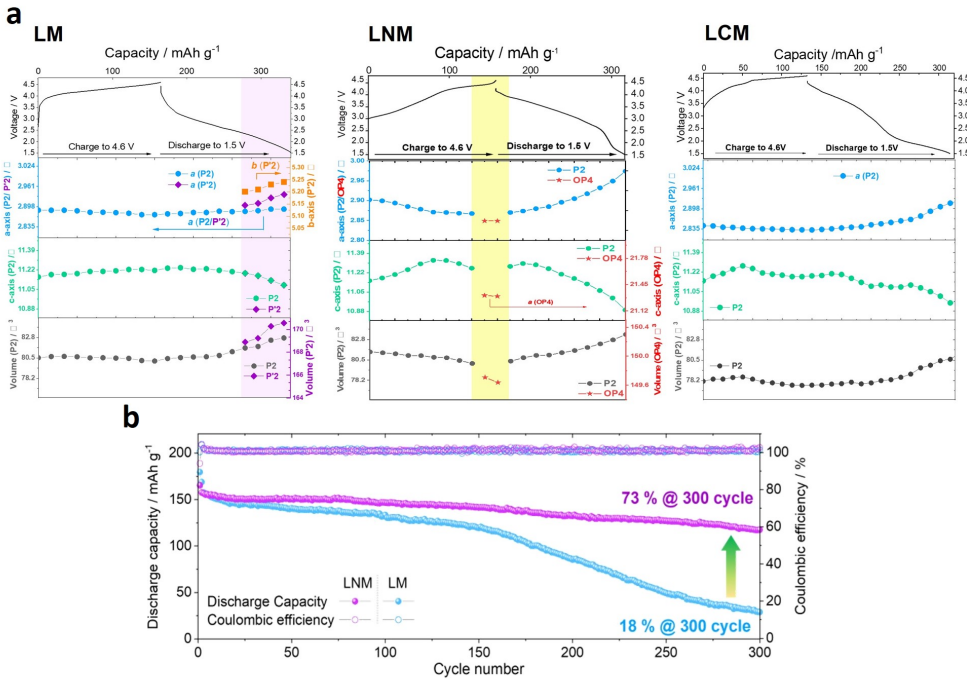

Figure 3.2: Experimental lattice parameter variations for (a) LM and (b) LNM and (c) LCM electrodes measured from the *o*-XRD patterns (c) LM and LNM compound at several C-rates (0.1 C - 5 C)

ions from the Na sites in the charged system (modelled by P2-$Na_{0.125}Co_{0.156}Mn_{0.689}O_2$) and optimized the lattice parameters. It is found that the *c*-axis value expands from 10.70 to 11.42 Å, which agrees with with the XRD data from our experimental project partner (Fig. 3.2). Therefore, we propose that the desodiation-induced expansion of the *c*-value for the charge would be due to the weakening of the electrostatic attraction between Na and O–TM–O layers because of the extraction of Na ions.

For the Ni-doped system, namely $Na_x[Li_{0.14}Ni_{0.17}Mn_{0.69}]O_2$ our DFT calculation indicates that the *a*-axis parameter decreases from 2.93 to 2.87 Å and that the *c*-axis increases considerably from 10.97 to 11.27 Å when x=0.75 $\rightarrow$ 0.22. The decrease in the *a*-axis after desodiation is most likely due to both the extraction of Na+ and the oxidation of Ni cations. To determine the reason behind the expansion of the *c*-axis, we computed the O-TM-O intralayer $d1$ and interlayer $d2$ distances, which determine the c-axis value: $c = 2(d1+d2)$. We found a similar trend for both $Na_x[Li_{0.22}Mn_{0.78}]O_2$ and $Na_x[Li_{0.14}Ni_{0.17}Mn_{0.69}]O_2$ in that $d1$ decreases while $d2$ increases with desodiation. The large expansion of the *c*-axis in the latter system is clearly due to the increase in $d2$, which is because of weakening of the electrostatic attraction between the O-TM-O layers with the extraction of Na ions. The shrinkage of $d1$ in both systems is due to the oxidation of reactive ions (i.e., Ni and/or O), which will be discussed later.

Although the $d2$ value for desodiated $Na_x[Li_{0.11}Mn_{0.78}]O_2$ expands, we do not find an increase in *c*-axis because this increase in $d2$ is smaller than the decrease in $d1$. The reason for the smaller increase in $d2$ for the system without Ni is because of Li migration. Our DFT calculation indicates that Li ions occupy TM sites in the discharged $Na_{0.67}[Li_{0.22}Mn_{0.78}]O_2$ system; however, half of them migrate spontaneously into Na sites after charging (Fig. 3.1), namely in the $Na_{0.11}[Li_{0.22}Mn_{0.78}]O_2$ system. The calculated c-axis for this system with partial Li ions in Na sites is, however, considerably shorter than that for $Na_{0.67}[Li_{0.22}Mn_{0.78}]O_2$ with all the Li ions in Mn sites. This result is not consistent with *o*-XRD data (Fig.3.2) showing the expansion of the c-axis with desodiation. However, after removing the Li ions from

the Na sites ($Na_{0.11}[Li_{0.22}Mn_{0.78}]O_2 \rightarrow Na_{0.11}[Li_{0.11}Mn_{0.78}]O_2$) and optimizing the lattice parameters, we observed that the *c*-axis value expands and becomes more comparable to the experiment. Therefore, we conclude that Li ions tend to leave the $Na_{0.11}[Li_{0.22}Mn_{0.78}]O_2$ lattice. With the migration and segregation of more Li ions, the *c*-axis value most likely becomes larger when *x* = 0.67 $\rightarrow$ 0.11. A similar result was not observed for the Ni-doped system, in which only 1/5 Li ions migrate spontaneously from TM to Na sites.

3.3.2 Redox mechanism during charging/discharging

To better understand the reason behind this phenomenon, we characterized the redox mechanism by computing the number of unpaired electrons (N_{unp}) on elements, spin density differences (SDD), and bond lengths. For $Na_{0.67}Li_{0.22}Mn_{0.78}O_2$ ($Na_{24}Li_8Mn_{28}O_{72}$), the computed average value of N_{unp}

Table 3.2: Calculated averaged number of unpaired electrons N_{unp} on cations and anions of LM and LNM using DFT-PBE+*U* and LCM using DFT-HSE06 functional in their charged and discharged states.

System	Na	Li	Mn	Ni/Co	O
$Na_{0.67}Li_{0.22}Mn_{0.78}O_2$	0.00	0.01	3.08	-	-0.05
$Na_{0.11}Li_{0.11}Mn_{0.78}O_2$	0.00	0.01	2.95	-	-0.28
$Na_{0.75}Li_{0.156}Co_{0.156}Mn_{0.689}O_2$	0.00	0.01	3.19	0.04	-0.03
$Na_{0.125}Li_{0.156}Co_{0.156}Mn_{0.689}O_2$	0.00	0.01	2.93	1.22	-0.17
$Na_{0.125}Co_{0.156}Mn_{0.689}O_2$	0.00	0.01	2.88	1.23	-0.22
$Na_{0.75}Li_{0.14}Ni_{0.17}Mn_{0.69}O_2$	0.00	0.01	$Mn_{24/25}$=3.10 $Mn_{1/25}$=3.81	$Ni_{5/6}$=1.75 $Ni_{1/6}$=1.13	-0.06
$Na_{0.22}Li_{0.14}Ni_{0.17}Mn_{0.69}O_2$	0.00	0.01	3.02	$Ni_{1/2}$=0.70 $Ni_{1/3}$=0.40 $Ni_{1/6}$=2.23	-0.11

$(\overline{N_{\text{unp}}})$ on all Mn cations is 3.08, showing a charge state of 4+ (Fig. 3.4c). Upon desodiation of x = 0.67 → 0.11, the calculated $\overline{N_{\text{unp}}}$ for all Mn cations became 2.95, indicating that Mn still remains in the charge states of 4+, as clearly observed in the SDD plot (Fig. 3.1). For $Na_{0.75}Li_{0.156}Co_{0.156}Mn_{0.689}O_2$ ($Na_{24}Li_5Co_5Mn_{22}O_{64}$), the calculated average values of N_{unp} on Mn and Co cations were 3.19 and 0.04, indicating a charge state of 3.81+ and 3+, respectively, on these cations (Figure 3.3 and Table 3.2).

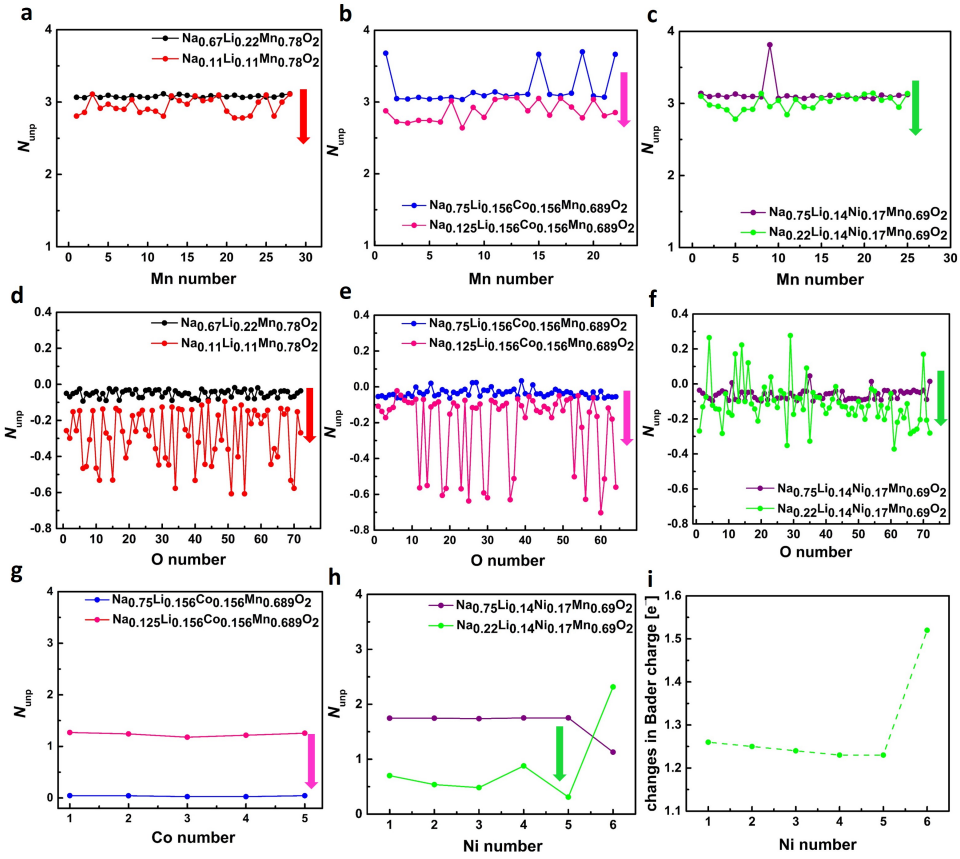

Figure 3.3: Calculated number of unpaired electrons N_{unp} on Mn for (a) LM, (b) LCM and (c) LNM and on O anions for (d) LM, (e) LCM and (f) LNM and on Co for (g) LCM and on Ni cations for (h) LNM using DFT for $Na_{0.67}[Li_{0.22}Mn_{0.78}]O_2$, $Na_{0.11}[Li_{0.11}Mn_{0.78}]O_2$, $Na_{0.75}[Li_{0.156}Co_{0.156}Mn_{0.689}]O_2$, $Na_{0.125}[Li_{0.156}Co_{0.156}Mn_{0.689}]O_2$, and $Na_{0.75}[Li_{0.14}Ni_{0.17}Mn_{0.69}]O_2$, $Na_{0.22}[Li_{0.14}Ni_{0.17}Mn_{0.69}]O_2$ (f) Bader charge on Ni for $Na_{0.22}[Li_{0.14}Ni_{0.17}Mn_{0.69}]O_2$. The applied XC functionals have been listed in Table 3.2.

The desodiation-induced oxidation of each ion was then estimated by analyzing the change in its N_{unp} with desodiation. Ions with ΔN_{unp} values smaller than 0.05 were considered to preserve their charges. To study the redox mechanism for the charge/discharge endpoints, we focused on the desodiation of *x* = 0.75 $\rightarrow$ 0.125 and considered two models for the low Na concentration: i) $Na_{0.125}Li_{0.156}Co_{0.156}Mn_{0.689}O_2$ and ii) $Na_{0.125}Co_{0.156}Mn_{0.689}O_2$. For $Na_{0.75}Li_{0.156}Co_{0.156}Mn_{0.689}O_2 \rightarrow Na_{0.125}Li_{0.156}Co_{0.156}Mn_{0.689}O_2$, the computed N_{unp} of Co cations is 1.22, indicating that each Co experiences an average oxidation of 0.78+ (considering a spin transition). The Mn cations experience an average oxidation of 0.27+. The clear increase in N_{unp} (Figure 3.3 and Table 3.2) and larger SDD (more blue features) of the oxygen anions (Figure 3.4) indicates their oxidation.

The contribution of O anions to the redox process is estimated to be ≈50%. In total, 10 oxygen anions per unit cell (O0.31) undergo a total oxidation of 5.28+ (an average oxidation of Δq = 0.53+), and 48 oxygen anions (O1.5) experience a total oxidation of 4.88+ (Δq = 0.10+). The total desodiation-induced oxidation of oxygen is then calculated to be 0.31+ per formula unit. The contribution of TM redox is estimated to be 50%. 5Co (Co0.16) and 22Mn (Mn0.69) per unit cell undergo, respectively, a total oxidation of 3.90+ (Δq = 0.78+) and 5.83+ (Δq = 0.27+).

The total desodiation-induced oxidation of TMs is 0.31+ per formula unit. For $Na_{0.75}Li_{0.156}Co_{0.156}Mn_{0.689}O_2 \rightarrow Na_{0.125}Li_{0.156}Co_{0.156}Mn_{0.689}O_2$, the computed Nunp for Co cations is 1.23, indicating that all of them experience a Δq of 0.77+ (considering a spin transition) with desodiation. Δq is computed to be 0.32+ for Mn cations. A clear increase in N_{unp} (Figure 3.3 and Table 3.2) and larger SDD (more blue features) of oxygen anions (Figure 3.4) that have lost their binding to removed Li ions indicate that they undergo a significant oxidation. Both N_{unp} and SDD indicate that the three O anions that are the nearest neighbors of each Li vacancy experience a large oxidation. Thus, 15 O anions per unit cell (O0.47) are oxidized after removing 5 Li ions.

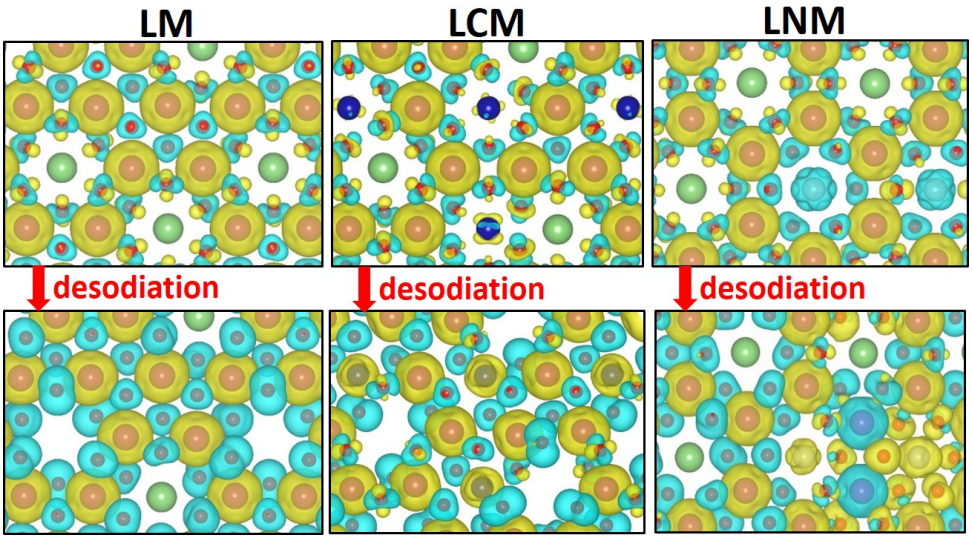

Figure 3.4: Computed spin density plots for LM, LCM and LNM at discharged and charged state with an isosurface of 0.006 $eV/Å^3$ was used for the SDD plots using DFT, the up- and down-spin electrons are in yellow and blue, respectively. The applied XC functionals have been listed in Table 3.2.

The total oxidation of these O anions is ≈9+. This means that only a total oxidation of ≈4+ (Δq = 0.27+) is due to the desodiation, and the rest is induced by the extraction of 5 Li. The rest of the 49 O per unit cell (O1.53) experience partial oxidations with a total charge of ≈5+ (Δq = 0.10+). The total desodiation induced oxidation of oxygen is then ≈0.28+ per formula unit. The contribution of oxygen to the total oxidation is estimated to be ≈45%. The rest is due to the oxidation of TMs, namely $Co_{0.16}^{0.77+}$ and $Mn_{0.69}^{0.32+}$. In the $Na_{0.75}Li_{0.14}Ni_{0.17}Mn_{0.69}O_2$ ($Na_{27}Li_5Ni_6Mn_{25}O_{72}$) system, the calculated value of $\overline{N_{\text{unp}}}$ for 24/25Mn and 1/25 Mn are 3.10 and 3.81, respectively, indicating that almost all the Mn cations have a charge state of 4+ (Fig. 3.4d).

The predicted charge states for 5/6Ni ($\overline{N_{\text{unp}}}$ = 1.75) and 1/6 Ni ($\overline{N_{\text{unp}}}$ = 1.13) cations are 2+ and 3+, respectively. With the desodiation of *x* = 0.75 → 0.22, Mn remains in the charge states of 4+ ($\overline{N_{\text{unp}}}$ = 3.01). The computed $\overline{N_{\text{unp}}}$ for Ni cations indicates that most of them experience oxidation with desodiation. $\overline{N_{\text{unp}}}$ for one of the Ni cations is 2.32 (Fig. 3.4h and Table 3.2). After analyzing the Bader charges on all the Ni cations (Fig. 3.4i), we observed that this Ni is even more oxidized than

the others. Considering a possible spin transition on this Ni, the average oxidation state of Ni cations is computed to be 3.46+. We also find that oxygen anions undergo oxidation, i.e., N_{unp} and SDD feature on some oxygen anions increase with desodiation (3.3d, 3.3e, 3.3f and 3.4 and Tab. 3.2). Nevertheless, the number of oxidized oxygen anions and their magnitude of oxidation are clearly smaller in the Ni-doped system.

3.3.3 Li migration

The reason of Li migration for $Na_{0.11}Li_{0.22}Mn_{0.78}O_2$ can now be understood in terms of bond lengths (Fig. 3.5). We observed that due to the ionic size of Li, the averaged bond length of $\bar{l}_{\text{Li-O}}$ in the Mn site cannot be shorter than 2.06 Å, as the value of $\bar{l}_{\text{Li-O}}$ was computed to be 2.08, 2.06, 2.11, and 2.06 Å, respectively, for Li ions in the TM sites of $Na_{0.67}Li_{0.22}Mn_{0.78}O_2$, $Li_{0.11}Li_{0.11}Mn_{0.78}O_2$, $Na_{0.75}Li_{0.14}Ni_{0.17}Mn_{0.69}O_2$, and $Na_{0.22}Li_{0.14}Ni_{0.17}Mn_{0.69}O_2$.

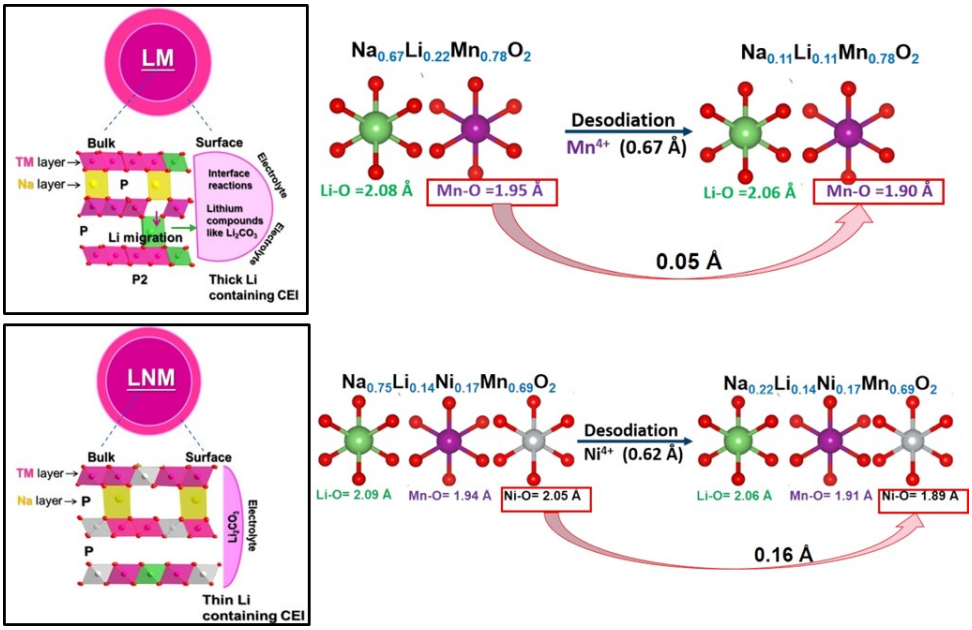

Figure 3.5: The schematic illustration of Li migration are presented and calculated averaged bond lengths between Li and O as well as TM and O in the studied cathode materials in their charged and discharged states using DFT.

Because of the oxidation of O, $\bar{l}_{\text{Mn-O}}$ = 1.95 becomes shorter by 0.05 Å for $Na_x[Li_{0.22}Mn_{0.78}]O_2$ when *x* = 0.67$\rightarrow$ 0.11.Å. This limits the space for Li ions, forcing them to leave the TM sites. However, for the Ni-doped system, $\bar{l}_{\text{Ni-O}}$ decreases from 2.05 to 1.89 Å when *x* = 0.75 $\rightarrow$ 0.22. This provides enough space for Li despite the contraction of $\bar{l}_{\text{Mn-O}}$ from 1.94 to 1.91 Å when *x* = 0.75 $\rightarrow$ 0.22 in $Na_x[Li_{0.14}Ni_{0.17}Mn_{0.69}]O_2$.

In this work, we calculated and analyzed magnetic moment (represented simply by N_{unp}) of elements to show clearly what ions and how much they are oxidized. Our calculated magnetic moments indicated relatively a lower oxygen redox activity in P2-$Na_{0.75}[Li_{0.14}Ni_{0.17}Mn_{0.69}]O_2$ compared to $Na_{0.67}[Li_{0.22}Mn_{0.78}]O_2$. Xiao et al.[50]. also found that Li substitution suppresses the oxygen redox activity in P2-$Na_{0.66}Ni_{0.25}Mn_{0.75}O_2$. Please note that we studied the effect of Ni substitution on P2-$Na_{0.67}Ni_{0.22}Mn_{0.78}O_2$ and found a mechanism that Ni substitution suppresses the migration of Li ions from TM to the Na layer (and then surface) and thereby oxidation of oxygen.

3.4 Conclusions

In this work, we simulated and studied P2-$Na_{0.67}[Li_{0.22}Mn_{0.78}]O_2$, P2-$Na_{0.75}[Li_{0.156}Co_{0.156}Mn_{0.689}]O_2$ and P2-$Na_{0.75}[Li_{0.14}Ni_{0.17}Mn_{0.69}]O_2$ as oxygen-redox-active cathode materials. Based on our results, we can conclude that co-doping of Li and Co/Ni into the TM layer positively affects the structural stability of Mn-rich oxygen redox-based P2-layered compounds. Li doping helps to activate the oxygen redox reaction and also prevents the P2-O2 phase transition, which usually leads to significant structural changes. These changes cause large lattice parameters change leading to large mechanical stress and degradation during charge/discharge (See chapter 2, where mechanical stress for Li-based material has been studied. Co and Ni substitution, gives fully Co and Ni-redox activity from Co^{3+}/Co^{4+} and Ni^{2+}/Ni^{4+} (despite reversible phase transition) during charging and anionic ($O^{2-}/(O_2)^{n-}$) redox reactions in LCM and LNM which are responsible for the high initial capacity. Furthermore, Ni-doping suppresses Li

migration to the Na alkali layer which in turn, plays the role of a stabilizer of structure and can be identified as a key point in improving the stability/electrode performance of $Na_{0.75}[Li_{0.14}Ni_{0.17}Mn_{0.69}]O_2$ compared with $Na_{0.67}[Li_{0.22}Mn_{0.78}]O_2$ and $Na_{0.75}[Li_{0.156}Co_{0.156}Mn_{0.689}]O_2$ material.

3.5 References

1. Hwang, J.Y., Myung, S.T., and Sun, Y.K. (2017). Sodium-ion batteries: Present and future. Chem. Soc. Rev. 46, 3529–3614.

2. A. Konarov, N. Voronina, J. H. Jo, Z. Bakenov, Y. K. Sun, S. T. Myung, ACS Energy Lett. 2018, 3, 2620.

3. J. Y. Hwang, S. T. Myung, Y. K. Sun, Adv. Funct. Mater. 2018, 28, 1802938.

4. Y. Li, M. Chen, B. Liu, Y. Zhang, X. Liang, X. Xia, Adv. Energy Mater. 2020, 10, 1.

5. Y. Zhang, X. Xia, B. Liu, S. Deng, D. Xie, Q. Liu, Y. Wang, J. Wu, X. Wang, J. Tu, Adv. Energy Mater. 2019, 9, 1.

6. S. Shen, R. Zhou, Y. Li, B. Liu, G. Pan, Q. Liu, Q. Xiong, X. Wang, X. Xia, J. Tu, Small Methods 2019, 3, 1.

7. A. Mendiboure, C. Delmas, P. Hagenmuller, J. Solid State Chem. 1985, 57, 323

8. A. D. Robertson, P. G. Bruce, Chem. Mater 2003, 15, 1984.

9. A. R. Armstrong, M. Holzapfel, P. Novák, C. S. Johnson, S. H. Kang, M. M. Thackeray, P. G. Bruce, J. Am. Chem. Soc. 2006, 128, 8694.

10. K. Luo, M. R. Roberts, N. Guerrini, N. Tapia-Ruiz, R. Hao, F. Massel, D. M. Pickup, S. Ramos, Y. S. Liu, J. Guo, A. V. Chadwick, L. C. Duda, P. G. Bruce, J. Am. Chem. Soc. 2016, 138, 11211.

11. N. Voronina, S. -T. Myung, Energy Mater. Adv. 2021, 2021, 1.

12. Y. Qiao, S. Guo, K. Zhu, P. Liu, X. Li, K. Jiang, C. J. Sun, M. Chen, H. Zhou, Energy Environ. Sci. 2018, 11, 299.

13. B. Mortemard De Boisse, G. Liu, J. Ma, S. I. Nishimura, S. C. Chung, H. Kiuchi, Y. Harada, J. Kikkawa, Y. Kobayashi, M. Okubo, A. Yamada, Nat. Commun. 2016, 7, 11397.

14. C. Zhao, Q. Yang, F. Geng, C. Li, N. Zhang, J. Ma, W. Tong, B. Hu, ACS Appl. Mater. Interfaces 2021, 13, 360.

15. Hwang, J.Y., Kim, J., Yu, T.Y., and Sun, Y.K. (2019).C. Zhao, Z. Yao, Q. Wang, H. Li, J. Wang, M. Liu, S. Ganapathy, Y. Lu, J. Cabana, B. Li, X. Bai, A. Aspuru-Guzik, M. Wagemaker, L. Chen, Y. S. Hu, J. Am. Chem. Soc. 2020, 142, 5742.

16. B. Xiao, X. Liu, X. Chen, G. H. Lee, M. Song, X. Yang, F. Omenya, D. M. Reed, V. Sprenkle, Y. Ren, C. J. Sun, W. Yang, K. Amine, X. Li, G. Xu, X. Li, Adv. Mater. 2021, 33, 2107141.

17. N. Yabuuchi, R. Hara, M. Kajiyama, K. Kubota, T. Ishigaki, A. Hoshikawa, S. Komaba, Adv. Energy Mater. 2014, 4, 1301453.

18. E. de La Llave, E. Talaie, E. Levi, P. K. Nayak, M. Dixit, P. T. Rao, P. Hartmann, F. Chesneau, D. T. Major, M. Greenstein, D. Aurbach, L. F. Nazar, Chem. Mater 2016, 28, 9064.

19. T. Risthaus, D. Zhou, X. Cao, X. He, B. Qiu, J. Wang, L. Zhang, Z. Liu, E. Paillard, G. Schumacher, M. Winter, J. Li, J. Power Sources 2018, 395, 16.

20. R. J. Clément, J. Billaud, A. R. Armstrong, G. Singh, T. Rojo, P. G. Bruce, C. P. Grey, Energy Environ. Sci. 2016, 9, 3240.

21. X. Cao, H. Li, Y. Qiao, X. Li, M. Jia, J. Cabana, H. Zhou, Adv. Energy Mater. 2020, 10, 1903785.

22. N. Voronina, N. Yaqoob, H. J. Kim, K. S. Lee, H. D. Lim, H. G. Jung, O. Guillon, P. Kaghazchi, S. T. Myung, Adv. Energy Mater. 2021, 11, 2100901.

23. A. J. Perez, D. Batuk, M. Saubanère, G. Rousse, D. Foix, E. McCalla, E. J. Berg, R. Dugas, K. H. W. van den Bos, M. L. Doublet, D. Gonbeau, A. M. Abakumov, G. van Tendeloo, J. M. Tarascon, Chem. Mater 2016, 28, 8278.

24. A. J. Perez, G. Rousse, J. M. Tarascon, Inorg. Chem. 2019, 58, 15644.

25. M. H. N. Assadi, M. Okubo, A. Yamada, Y. Tateyama, J. Mater. Chem. A 2018, 6, 3747.

26. K. Jiang, X. Zhang, H. Li, X. Zhang, P. He, S. Guo, H. Zhou, ACS Appl. Mater. Interfaces 2019, 11, 14848.

27. X. Zhang, Y. Qiao, S. Guo, K. Jiang, S. Xu, H. Xu, P. Wang, P. He, H. Zhou, Adv. Mater. 2019, 31, 1807770.

28. P. E. Pearce, G. Rousse, O. M. Karakulina, J. Hadermann, G. van Tendeloo, D. Foix, F. Fauth, A. M. Abakumov, J. M. Tarascon, Chem. Mater 2018, 30, 3285.

29. E. de La Llave, P. K. Nayak, E. Levi, T. R. Penki, S. Bublil, P. Hartmann, F. F. Chesneau, M. Greenstein, L. F. Nazar, D. Aurbach, J. Mater. Chem. A 2017, 5, 5858.

30. T. Jin, P. F. Wang, Q. C. Wang, K. Zhu, T. Deng, J. Zhang, W. Zhang, X. Q. Yang, L. Jiao, C. Wang, Angew. Chem., Int. Ed. 2020, 59, 14511.

31. N. Yabuuchi, R. Hara, K. Kubota, J. Paulsen, S. Kumakura, S. Komaba, J. Mater. Chem. A 2014, 2, 16851.

32. U. Maitra, R. A. House, J. W. Somerville, N. Tapia-Ruiz, J. G. Lozano, N. Guerrini, R. Hao, K. Luo, L. Jin, M. A. Pérez-Osorio, F. Massel, D. M. Pickup, S. Ramos, X. Lu, D. E. McNally, A. v. Chadwick, F. Giustino, T. Schmitt, L. C. Duda, M. R. Roberts, P. G. Bruce, Nat. Chem. 2018, 10, 288.

33. H. J. Kim, A. Konarov, J. H. Jo, J. U. Choi, K. Ihm, H. K. Lee, J. Kim, S. T. Myung, Adv. Energy Mater. 2019, 9, 1901181.

34. A. Konarov, H. J. Kim, J. H. Jo, N. Voronina, Y. Lee, Z. Bakenov, J. Kim, S. T. Myung, Adv. Energy Mater. 2020, 10, 2001111.

35. W. Zheng, Q. Liu, Z. Wang, Z. Yi, Y. Li, L. Cao, K. Zhang, Z. Lu, J. Power Sources 2019, 439, 227086.

36. X. Rong, E. Hu, Y. Lu, F. Meng, C. Zhao, X. Wang, Q. Zhang, X. Yu, L. Gu, Y. S. Hu, H. Li, X. Huang, X. Q. Yang, C. Delmas, L. Chen, Joule 2019, 3, 503.

37. D. Kim, M. Cho, K. Cho, Adv. Mater. 2017, 29, 1701788.

38. R. A. House, U. Maitra, M. A. Pérez-Osorio, J. G. Lozano, L. Jin, J. W. Somerville, L. C. Duda, A. Nag, A. Walters, K. J. Zhou, M. R. Roberts, P. G. Bruce, Nature 2020, 577, 502.

39. Z. Lu, J. R. Dahn, J. Electrochem. Soc. 2001, 148, A1225.

40. A. Konarov, J. U. Choi, Z. Bakenov, S. T. Myung, J. Mater. Chem. A 2018, 6, 8558.

41. N. Yabuuchi, M. Kajiyama, J. Iwatate, H. Nishikawa, S. Hitomi, R. Okuyama, R. Usui, Y. Yamada, S. Komaba, Nat. Mater. 2012, 11, 512.

42. A. Konarov, H. J. Kim, N. Voronina, Z. Bakenov, S. T. Myung, ACS Appl. Mater. Interfaces 2019, 11, 28928.

43. Blochl. P. E, Phys. Rev. B, 1994, 50, 17953.

44. Kresse. G, and Furthmüller. J, Phys. Rev. B, 1996, 54, 11169.

45. Perdew. J. P, Burke. K, and Ernzerhof. M, Phys. Rev. Lett, 1996, 77, 3865.

46. Dudarev. S. L, Botton. G. A, Savrasov. S.Y, Humphreys. C. J, and Sutton. A. P, Phys. 10 Rev. B, 1998, 57, 1505.

47. A. V. Kruka u, O.A. Vydrov, A.F. Izmaylov, G.E. Scuseria, The Journal of Chemical Physics, 2006, 22, 224106

48. Okhotnikov. K, Charpentier. T, and Cadars. S, J. Cheminform, 2016, 8, 17.

49. Momma, K., and Izumi, F. J. Appl. Cryst, 2011, 44, 1272–1276

50. B. Xiao, X. Liu, X. Chen, G. H. Lee, M. Song, X. Yang, F. Omenya, D. M. Reed, V. Sprenkle, Y. Ren, C. J. Sun, W. Yang, K. Amine, X. Li, G. Xu, X. Li, Adv. Mater. 2021, 33, 2107141.

4

Optimization of P2-Type Sodium-ion battery Cathodes via Li, Mg, and Ni Co-Doping: A Path to Enhanced Capacity and Stability

Abstract: Understanding the oxygen-redox reactions within Mn-rich layered cathode materials is an important strategy to improve the capacity of sodium-ion batteries (SIBs) while satisfying the demand for low cost and the use of abundant resources. Nonetheless, the P2-type $Na_y[A_xMn_{1-x}]O_2$ compositions (where A = electro-inactive elements) exhibit poor capacity retention. In addition, $Na_y[TM_xMn_{1-x}]O_2$ (where TM = transition metal) still suffers from low capacity in the absence of anion redox activity. This investigation introduces Li, Mg, and Ni into the P2-layered Na_xMnO_2 matrix to explore diverse compositional dynamics engineered by density functional theory (DFT) and *ab* initio molecular dynamics. The P2-$Na_{0.7}[Li_{0.1}Mg_{0.05}Ni_{0.15}Mn_{0.7}]O_2$ configuration was optimized, exhibiting enhanced structural stability. *Ab* initio molecular dynamics (AIMD) simulation affirmed the preservation of the P2 structure throughout de/sodiation, and comprehensive structural analyses through density functional theory unravelled the complex charge-compensation mechanisms facilitated by Ni^{2+}/Ni^{4+}, Mn^{3+}/Mn^{4+}, and $O^{2-}/(O_2)^{n-}$ redox pairs. Comprehensive analysis of both techniques elucidated the Li migration phenomena within the TM and sodium layers. This research underscores the pivotal role of Li, Mg, and Ni co-doping in the development of cathode materials.

4.1 Introduction

The battery market is being confronted with an escalating demand for large-scale applications, notably electric vehicles (EVs) and energy storage systems (ESSs). This surge in demand necessitates attributes such as cost-effectiveness, appreciable energy density, long-term sustainability, and dependable safety properties. In response to these requirements, sodium-ion batteries (SIBs) have emerged as formidable alternatives to lithium-ion batteries (LIBs), primarily due to their promising potential in meeting the aforementioned criteria. Among various cathode material structures[1–3], layered metal oxides have been identified as promising candidates. These structures maintain their original form upon the incorporation of one mole of Na per formula unit, and discharge capacities exceeding 200 mAh g^{-1} have been reported for P2-Na_xMnO_2 (where typically $x \leq 0.7$)[4]. However, the capacity retention often falls short of expectations because of Jahn–Teller distortion of MnO6 octahedra leading to the P'2 phase[5], the presence of Na^+/vacancy ordering [6], and phase transitions toward an O-based phase that induces significant changes along the *c*-axis[7]. The partial substitution of Mn with 3*d* transition metals (TMs; Ni[8,9], Fe[10,11], Cu[12,13], and Co[14,15] has been proposed as a strategy to overcome these limitations. Ni, in particular, is appealing for its two-electron redox capability (Ni^{2+}/Ni^{4+}), which is typically associated with high operation voltages.

Recent advancements in TM layer engineering have enabled an increase in achievable capacity through oxygen redox activity. A prerequisite for this enhancement is the establishment of a tetravalent Mn-rich layered structure, necessitating a specific arrangement of Na–O–A (A being Li[16–18], Mg[19–21], and Zn[22,23] in $Na_x[A_yTM_{1-y}]O_2$) to facilitate an additional reaction activated by oxygen redox. The presence of these A element in the TM layers allows charge compensation for the oxidation of TM elements to progress via the extraction of Na^+ ions from the host structure. With the

This chapter is mainly based on the theory part of publication:
M.J Cho, N. Yaqoob, J. H. Yu, K. Köster, A.Y. Kim, H.G. Jung,...& P. Kaghazchi, S.T. Myung, Advanced Energy Materials, 2025, 15, 2405112.
N.Yaqoob and M.J Cho contributed equally to this work.

Na–O–A configurations in $Na_x[A_yTM_{1-y}]O_2$, the migration of A elements to Na layers and/or the evolution of lattice oxygen can occur. This leads to the degeneration of spin in the O 2*p* orbital, accompanied by additional charge compensation through Na^+ extraction for oxygen redox[24]. Among the A elements, Li exhibits the lowest electronegativity, suggesting easier migration compared to Mg and Zn during the charge-compensation process by oxygen redox.

Our literature review underlines the significance of using A elements to enhance oxygen activity. For the Na–O–Li configuration (x = $\sim$0.7 and y = $\sim$ 0.2 for $Na_x[Li_yMn_{1-y}]O_2$[18]), the average oxidation state of Mn typically approaches 4+, with the main charge compensation occurring through the oxidation/reduction of lattice oxygen[25]. However, this system encounters challenges, such as low operating voltage on discharge and significant voltage hysteresis. The migration of Li from the TM to Na layer triggers oxygen oxidation, resulting in slow Na^+ diffusion during de/sodiation processes. This mitigates the need for the evolution of lattice oxygen during the desodiation process since the migration leads to the formation of unpaired electrons in the O 2*p* orbital. The introduction of Mg as an A element has demonstrated the potential for delivering a substantial capacity exceeding 200 mAh g^{-1} for $Na_{2/3}[Mg_{0.28}Mn_{0.72}]O_2$[26].

Although the capacity offered is impressive, the observed substantial voltage hysteresis remains a critical issue. Similarly, the Na–O–Zn configuration in $Na_{2/3}[Zn_{1/3}Mn_{2/3}]O_2$[22] exhibited comparable characteristics to $Na_{2/3}[Mg_{0.28}Mn_{0.72}]O_2$ in terms of capacity, surpassing 200 mAh g^{-1}. Nonetheless, the significant voltage hysteresis, coupled with low operation voltage on discharge and slow kinetics, detracts from the high-capacity advantage. To address these concerns, partial replacement of A elements (A = Li and Zn) with divalent Ni, such as in $Na_{0.75}[Li_{0.15}Ni_{0.15}Mn_{0.7}]O_2$ and $Na_{0.66}[Zn_{0.07}Ni_{0.26}Mn_{0.67}]O_2$, has been proposed to induce higher operating voltages through the Ni^{2+}/Ni^{4+} redox and enhance long-term cycling stability[16,27]. The electrodes mentioned typically undergo a phase transition from the P2 to OP4 phase or structural disorder by forming octahedrally coordinated Na layers within a prismatic framework during the oxygen-redox

process. In addition, recent work indicates promising cycling performance when an octahedral environment, such as the OP4 phase, emerges in the Na layers during desodiation[14]. As Li migrates to the Na layer upon desodiation, the formed octahedral surroundings effectively accommodate the migrated Li element within the Na layer of the OP4 phase. Alternatively, migrated Li tends to diffuse towards the surface, forming Li_2CO_3 and LiF, thus constituting cathode–electrolyte interphase (CEI) layers. This phenomenon leads to gradual capacity fading.

In this work, we aim to identify the determinants that facilitate oxygen redox by employing appropriate elements in the A site of the TM layer, $Na_x[A_yTM_{1-y}]O_2$. As previous studies indicate that the migration of Li from the TM to Na layer aids in the participation of lattice oxygen in the electrochemical reaction[16], it is postulated that partial replacement of Mg with Li could activate more lattice oxygen in $Na_x[A_yTM_{1-y}]O_2$, contributing to charge compensation. More crucially, we have observed that the two-electron Ni^{2+}/Ni^{4+} redox is instrumental in elevating the redox potential and enhancing the resultant capacity [28]. Hence, the engineering of the A site with Li, Mg, and Ni elements within the TM layers is anticipated to increase the operation voltage for oxygen redox, diminish voltage hysteresis, and improve the capacity with the help of the functionality of each element: specifically, P2-$Na_z[Li_xMg_{0.3-x-y}Ni_yMn_{0.7}]O_2$ (x = 0–0.15, y = 0–0.15, z = 0.6–0.75). These phenomena are explored through diverse compositional dynamics engineered by density functional theory (DFT), *ab* initio molecular dynamics (AIMD) and *Operando* X-ray diffraction (XRD) studies (data from experimental group). DFT and AIMD-studies illustrate that multiple Ni^{2+}/Ni^{4+}, Mn^{3+}/Mn^{4+}, and $O^{2-}/(O_2)^{n-}$ redox reactions are responsible for charge compensation with sodium ions and discloses the migration of both Li and Mg elements from the TM to Na layers during charge. However, the recovery of these elements to the TM layers is probably not fully reversible during discharge, resulting in gradual capacity fading as Li components are present not only on the surface of the active material as a CEI layer but also in the electrolyte after cycling.

Notably, the covalent character introduced by Ni enhances the recovery of the Li

element to the TM layers in addition to lifting the operation voltage via the Ni^{2+}/Ni^{4+} redox pair. This finding indicates that employing both Li and Ni elements in the Mg site of TM layers not only facilitates stable oxygen-redox reactions but also mitigates the irreversible migration of Li. The tetravalent Mn, fixed at 0.7 mol, cannot be further oxidized to a higher valence in the octahedral environment of the TM layer during desodiation. Therefore, it is convenient to compare the effects of Li, Mg, and Ni elements in the A site of $Na_x[A_yMn_{0.7}]O_2$ (Mn: 4+) on the oxygen redox reaction. Herein, we disclose the compositional dynamics engineered by DFT and AIMD and elucidate the effectiveness of each substituent on the structure and electrochemical activity of P2-$Na_z[Li_xMg_{0.3-x-y}Ni_yMn_{0.7}]O_2$.

4.2 Method

To find favorable atomistic structures of each system, we performed Coulomb energy (E_c) analysis, DFT, and AIMD simulations. The arrangements of the Li, Mg, Mn, and Ni ions were determined using a Coulomb-energy analysis with the help of the so-called supercell code[29]. Spin-polarized DFT calculation and AIMD simulation were performed using the projector augmented wave (PAW) potential method[30] implemented in the Vienna Ab Initio Simulation Package (VASP) code[31]. The generalized gradient approximation (GGA) within the scheme of Perdew–Burke–Ernzerhof (PBE)[32] was used to describe the exchange-correlation (XC) functional for atomistic structure calculations (DFT and AIMD). The binary, ternary, and quaternary systems were modeled using 4 × 5 × 1 supercells with the following number of atoms for each case: $Na_{0.6}Mg_{0.3}Mn_{0.7}O_2$ ($Na_{24}Mg_{12}Mn_{28}O_{80}$) $Na_{0.6}Mg_{0.15}Ni_{0.15}Mn_{0.7}O_2$ ($Na_{24}Mg_6Ni_6Mn_{28}O_{80}$), $Na_{0.75}Li_{0.15}Mg_{0.15}Mn_{0.7}O_2$ ($Na_{30}Li_6Mg_6Mn_{28}O_{80}$), $Na_{0.7}Li_{0.1}Mg_{0.1}Ni_{0.1}Mn_{0.7}O_2$ ($Na_{28}Li_4Mg_4Ni_4Mn_{28}O_{80}$), and $Na_{0.7}Li_{0.1}Mg_{0.05}Ni_{0.15}Mn_{0.7}O_2$ ($Na_{28}Li_4Mg_2Ni_6Mn_{28}O_{80}$). An energy cut-off of 520 eV as well as a gamma-centered k-point mesh of 2 × 2 × 2 and 1 × 1 × 1 were applied for DFT calculation and AIMD simulations, respectively. Electronic and force convergence criteria of 10^{-4} eV and $0.02eV/$Å, respectively, were used for DFT calculations. The AIMD simulations were performed using the

fully optimized structures of $Na_{0.1}Mg_{0.15}Ni_{0.15}Mn_{0.7}O_2$, $Na_{0.1}Li_{0.15}Mg_{0.15}Mn_{0.7}O_2$, and $Na_{0.1}Li_{0.1}Mg_{0.05}Ni_{0.15}Mn_{0.7}O_{0.2}$ from DFT- PBE calculation.

As AIMD simulations are computationally demanding, we performed AIMD simulations for the three aforementioned compositions to see how the behavior of the materials changes during desodiation/charging. An *NVT* ensemble with the Nosé–Hoover thermostat[33] as well as an *NPT* ensemble with the Langevin thermostat/Dynamics[34] at 300 K and 800 K were performed with a total run time of 20 ps and a time step of 1 fs. The first 10 ps was used to achieve equilibrium, and the last 10 ps was considered the production run. The evolution of the energy, temperature, and pressure during the total 20 ps run in the three systems for which we performed AIMD-NVT and NPT simulations at 300 K and 800 K, respectively, are presented in Fig (a-c). We used an atmospheric pressure of 1 bar using the Parinello–Rahman barostat[35,36] method in *NPT* simulations. Finally, we performed DFT-PBE calculation on an energetically favorable structure of each case determined from the last AIMD steps to analyze the atomistic structures. The electronic structures were computed with DFT-HSE06[37]. For the rest of the two structures ($Na_xMg_{0.3}Mn_{0.7}O_2$ and $Na_xLi_{0.1}Mg_{0.1}Ni_{0.1}Mn_{0.7}O_2$) for which we did not perform AIMD simulations, the optimized geometries from DFT-PBE were used to calculate DFT-HSE06 electronic structures. Atomistic structures and spin density difference (SDD) plots were visualized with the VESTA program[38].

To find the most favorable structures of $Na_xMg_{0.3}Mn_{0.7}O_2$, $Na_xMg_{0.15}Ni_{0.15}Mn_{0.7}O_2$, $Na_xLi_{0.15}Mg_{0.15}Mn_{0.7}O_2$, $Na_xLi_{0.1}Mg_{0.1}Ni_{0.1}Mn_{0.7}O_2$, $Na_xLi_{0.1}Mg_{0.05}Ni_{0.15}Mn_{0.7}O_2$ with different *x* values, we modeled and calculated the total Coulomb energy (E_C) of a large number of likely structures. By performing the DFT-PBE calculation on the electrostatically most favorable configuration, we determined the lowest total energy structure and used that structure to study the charged case. The total number of considered configurations for E_C calculation and the charge states of ions for each *x* value are as follows.

$Na_{0.6}Mg_{0.3}Mn_{0.7}O_2$ ($Na_{24}Mg_{12}Mn_{28}O_{80}$): To model this structure, we had to use a 2-step process because the calculation of E_C for all possible configurations with

24 Na ions in 40 Na sites as well as 12 Mg ions and 28 Mn ions 40 Mn sites, namely $\frac{40!}{24!16!}\cdot\ \frac{40!}{28!12!}$ = 3.51E+20, was computationally intractable. Therefore, we had to first fix TM-sites and find all possible configurations with 24 Na ions in 40 Na sites, namely $\frac{40!}{24!16!}$ = 6.3E+10 structures. The charge states of Na, Mn, and O were considered to be 1+, 3.40+, and $2-$, respectively. We obtained the lowest E_C structure and then fixed Na-ions in their determined Na sites, and afterward, we determined the distribution of 12 Mg ions and 28 Mn ions in 40 TM sites, $\frac{40!}{28!12!}$= 5.6E+09 structures. We used the charge states of 1+ for Na, 2+ for Mg, 4+ for Mn, and $2-$ for O.

Na$_{0.1}$**Mg**$_{0.3}$**Mn**$_{0.7}$**O**$_2$ ($Na_4Mg_{12}Mn_{28}O_{80}$): Modeling of $\frac{24!}{4!12!}$ = 1.06E+04 structures for 4 Na ions in 24 Na sites with charges of 1+ for Na, 2+ for Mg, 4+ for Mn, and $1.75-$ for O were performed.

Na$_{0.60}$**Mg**$_{0.15}$**Ni**$_{0.15}$**Mn**$_{0.7}$**O**$_2$ ($Na_{24}Mg_6Ni_6Mn_{28}O_{80}$): We used the $Na_{0.60}Mg_{0.3}Mn_{0.7}O_2$ structure with already determined Na-sites to model $Na_{0.60}Mg_{0.15}Ni_{0.15}Mn_{0.7}O_2$ structure and we fixed the Na-ions in their sites and calculate Mg arrangement in 40 Mn-sites with creating $\frac{40!}{6!34!}$ = 3.84E+06 structures and then Ni-arrangement with $\frac{34!}{6!28!}$ = 1.34E+06 structures with a charge of 1+ for Na,2+ for Ni, 4+ for Mn, and $2-$ for O.

Na$_{0.1}$**Mg**$_{0.15}$**Ni**$_{0.15}$**Mn**$_{0.7}$**O**$_2$ ($Na_4Mg_6Ni_6Mn_{28}O_{80}$): $\frac{24!}{4!20!}$ = 1.06E+04 structures with a charge state of 4+ for Ni and $1.90-$ for O, however, charge state of other elements remains same.

Na$_{0.75}$**Li**$_{0.15}$**Mg**$_{0.15}$**Mn**$_{0.7}$**O**$_2$ ($Na_{30}Li_6Mg_6Mn_{28}O_{80}$): $\frac{40!}{30!10!}$ = 8.48E+08 structures with 30 Na ions in 40 Na sites with a charge of 1+ for Na, 3.25+ for Mn, and $2-$ for O were modelled. To find the arrangement of 6 Li ions and 6 Mg ions in $Na_{30}Mn_{40}O_{80}$, we, then, fixed the 30 Na and studied Li arrangement in 40 Mn-sites with creating $\frac{40!}{6!34!}$ = 3.84E+06 structures and then Mg- arrangementwith $\frac{34!}{6!28!}$= 1.34E+06 structures. We used 1+ for Na/Li, 2+ for Mg, 4+ for Mn, and $2-$ for O.

Na$_{0.1}$**Li**$_{0.15}$**Mg**$_{0.15}$**Mn**$_{0.7}$**O**$_2$ ($Na_4Li_6Mg_6Mn_{28}O_{80}$): $\frac{30!}{4!26!}$ = 2.74E+04 structures with a charge state of $1.675-$ for O, however, charge state of other elements remains same.

Na$_{0.7}$**Li**$_{0.1}$**Mg**$_{0.1}$**Ni**$_{0.1}$**Mn**$_{0.7}$**O**$_2$ ($Na_{28}Li_4Mg_4Ni_4Mn_{28}O_{80}$): we modelled $\frac{40!}{28!12!}$ = 5.59E+09 structures for 28 Na ions in 40 Na-sites with elementary charge state of 1+ for Na, 3.3+ for Mn, and 2− for O. Then we find Li and Mg-arrangement in 40 Mn sites with $\frac{40!}{4!36!}\cdot\ \frac{36!}{4!32!}$ = 5.38E+09 structures. Afterward, we find Ni-arrangement in 32 remaining Mn-sites $\frac{32!}{4!28!}$= 3.60E+04 structures. Charge states of 1+ for Na/Li, 2+ for Ni/Mg, 4+ for Mn, and 2− for O were used.

Na$_{0.7}$**Li**$_{0.1}$**Mg**$_{0.05}$**Ni**$_{0.15}$**Mn**$_{0.7}$**O**$_2$ ($Na_{28}Li_4Mg_2Ni_6Mn_{28}O_{80}$): To modelled this structure we used the already determined high Na-arrangement from structures of $Na_{0.7}Li_{0.1}Mg_{0.1}Ni_{0.1}Mn_{0.7}O_2$ and then find Li, and Mg arrangement in 40 Mn- sites $\frac{40!}{4!36!}\cdot\ \frac{36!}{2!34!}$ = 5.8E+07 structures and then calculate Ni-arrangement in remaining 34-Mn sites $\frac{34!}{6!28!}$ = 1.34E+06 structures. We used the charge states of 1+ for Na/Li, 2+ for Ni, 4+ for Mn, and 2− for O.

Na$_{0.1}$**Li**$_{0.1}$**Mg**$_{0.05}$**Ni**$_{0.15}$**Mn**$_{0.7}$**O**$_2$ ($Na_4Li_4Mg_2Ni_6Mn_{28}O_{80}$): $\frac{28!}{4!24!}$ = 2.05E+04 structures with 4 Na ions in 28 Na sites with a charge of 1+ for Na/Li, 2+ for Mg, 4+ for Ni/Mn, and 1.85− for O were modelled.

4.3 Results and Discussion

To determine high-performance cathode materials (in terms of stability and capacity) among the P2-$Na_z[Li_xMg_{0.3-x-y}Ni_yMn_{0.7}]O_2$ (x = 0 — 0.15, y = 0 — 0.15, z = 0.6 — 0.75) compounds, their pristine and charged states were simulated using ab initio methods including DFT and AIMD. To maintain the charge neutrality of pristine cases, a Na concentration variation of z = 0.6 — 0.75 depending on the composition of each compound was applied. The charged cases were modelled by applying a z value of 0.10 for all cases. Because of the different values of the Na concentration of z(0.7)-z(0.09), we would expect different initial capacities at a similar applied charging voltage for the systems studied in this work.

Modelling of the pristine systems by finding likely atomistic arrangements with the help of Coulomb interaction analysis followed by full DFT optimizations is straightforward as the optimized structure is expected to be close to the non-distorted starting structure. For the charged structures, however, previous studies

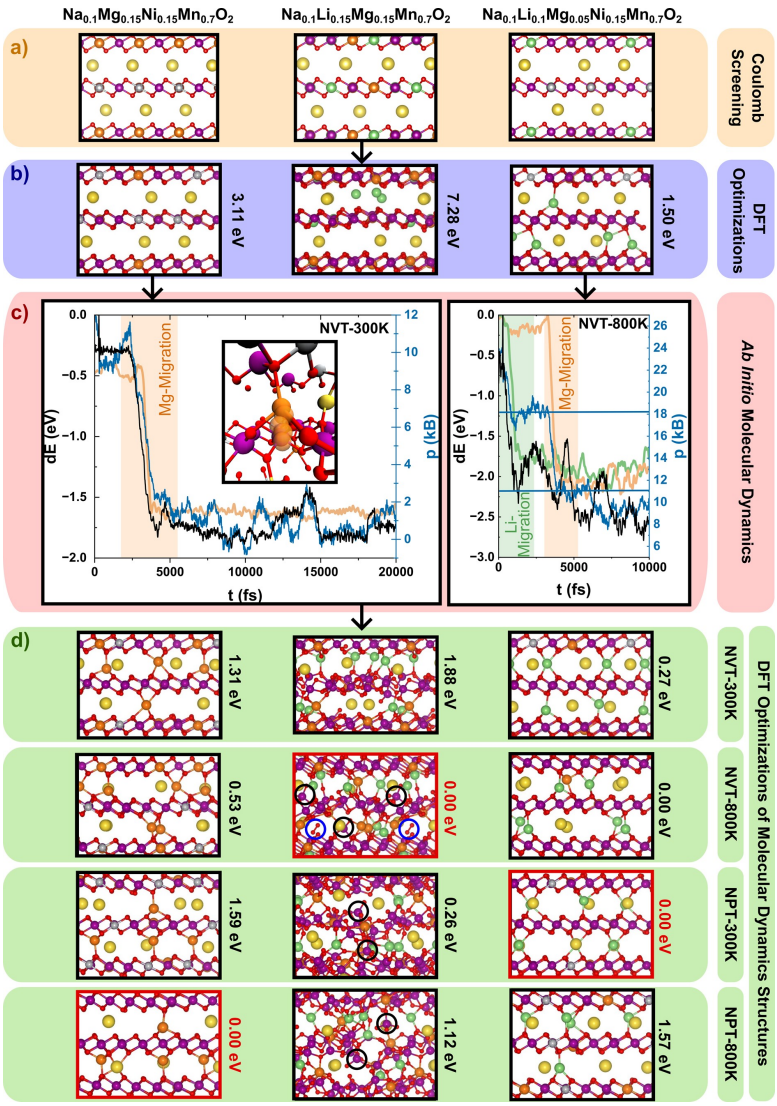

Figure 4.1: Multi-level procedure to obtain low-energy structures for discharged materials. First, Coulomb screening on an atomistic arrangement is performed (a), followed by DFT optimization (b) allowing only for limited migration of Li and Mg to the Na layers. In the next level (c), ab initio molecular dynamics simulations are performed that allow for migrations, as indicated by the mean displacements of Mg (orange) and Li (green) relative to the TM layer. The migrations are accompanied by a reduction in energy (black, left axis) and decrease of stress (blue, right axis). Finally, another DFT optimization is performed (d) on molecular dynamics structures of different ensembles at various temperatures, resulting in energetically more favorable atomistic structures. The lowest energy structures for each composition are marked in red. For $Na_{0.1}[Li_{0.15}Mg_{0.15}Mn_{0.7}]O_2$, migrated Mn cations are highlighted by black circles and oxygen dimers by blue circles (enlarged snapshot of lowest energy structure is given in Figure 4.4-4.6).

have indicated that Li and Mg ions in the TM layer are prone to migrate to the sodium sites or even to the surface of the material[14,16,29,30]. The migration process can be hindered by an energy barrier that cannot be overcome by the 0 K DFT optimization, which usually finds a minimum-energy structure biased to the starting one without Li and/or Mg migration.

Moreover, structural adjustments (e.g., lattice parameters) because of migrations are biased towards the starting structure in DFT optimizations. As a consequence, it is probable that only the lighter Li ions, which also show a more pronounced ionic-radius mismatch compared to Ni and Mn in the TM layer, might migrate after DFT optimization (Figure 4.1b) of the undistorted structures that were obtained from Coulomb energy analysis screening (Figure 4.1a). Introducing migrations of Li and/or Mg manually in the initial structures for DFT optimization can yield lower- energy structures, suggesting that a rather poor local energy minimum might be reached by optimizing the undistorted structures. To determine more realistic atomistic models of the charged states, it is therefore necessary to perform a multi-step optimization approach including Coulomb energy analysis, DFT optimization, and AIMD simulation, as depicted schematically in Figure 4.1. In

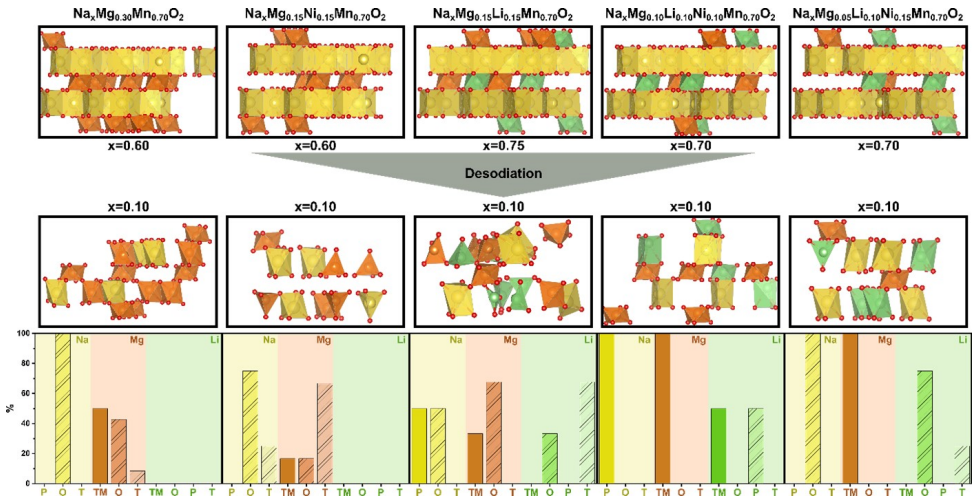

Figure 4.2: Comparison of coordination environments obtained from DFT geometries of Na, Li,and Mg before and after desodiation along with percentual occupation of octahedral (O), prismatic (P), and tetrahedral (T) sodium layer sites and octahedral TM layer sites per species after desodiation. In the sodiated state, all the sodium are in P sites and all the Li and Mg are in octahedral TM layer sites.

particular, applying a finite temperature (and thereby dynamics) to each system would help to overcome likely migration barriers. This can be effectively achieved by AIMD simulations. The mean displacements of Mg/Li relative to the TM layer prove that AIMD in a canonical (NVT) ensemble enable effective migration of Mg/Li towards the sodium layer. The left plot in Figure 4.1c shows the NVT run at 300 K for $Na_{0.1}[Mg_{0.15}Ni_{0.15}Mn_{0.7}]O_2$ where a Mg migration, as sketched in the inlet of the plot, occurs after ~ 3.10 ps of a simulation run and is completed after ~ 3.75 ps. The migration is accompanied by a significant decrease of stress (an external pressure decrease of ~ 9 kB) as well as energy of ~ 1.5 eV (per simulated supercell). Similar behavior is observed at the beginning of the AIMD simulation for $Na_{0.1}[Li_{0.1}Mg_{0.05}Ni_{0.15}Mn_{0.7}]O_2$ in NVT at 800 K. Here, a Li migration appears at the very beginning of the simulation at ~ 0.60 ps and is completed at 1.15 ps followed by a migration of Mg at ~ 3.28 to ~ 3.89 ps. The migration of Li and Mg occurs on a similar timescale despite the rather different atomic weights, which is probably caused by the high potential energy force for migration and/or the high kinetic energy at 800 K. Migration of Li and Mg also causes a step-wise decrease of stress by ~ 6 and ~ 7 kB, respectively, resulting in an overall trend of a reducing energy. Both examples for the AIMD runs indicate the importance of a multi-level optimization approach for these materials as most migrations cannot be observed in pure DFT optimizations. Using the determined structures from AIMD to perform DFT geometry optimizations again yields structures that are significantly lower in energy (Figure 4.1d) than the initial DFT calculations (Figure 4.1b). In fact, all the lowest energy structures for the studied compositions were obtained from AIMD runs leading to the migration of Li and/or Mg. For two out of three compositions, namely ($Na_{0.1}[Mg_{0.15}Ni_{0.15}Mn_{0.7}]O_2$ and $Na_{0.1}[Li_{0.15}Mg_{0.15}Mn_{0.7}]O_2$), the lowest energy structure was obtained after AIMD runs at an elaborated temperature of 800 K, which might be explained by the fact that kinetically hindered processes such as migrations are equilibrated faster at higher temperatures.

Moreover, two out of three lowest energy structures ($Na_{0.1}[Mg_{0.15}Ni_{0.15}Mn_{0.7}]O_2$ and $Na_{0.1}[Li_{0.1}Mg_{0.05}Ni_{0.15}Mn_{0.7}]O_2$) were obtained after NPT runs. The structure

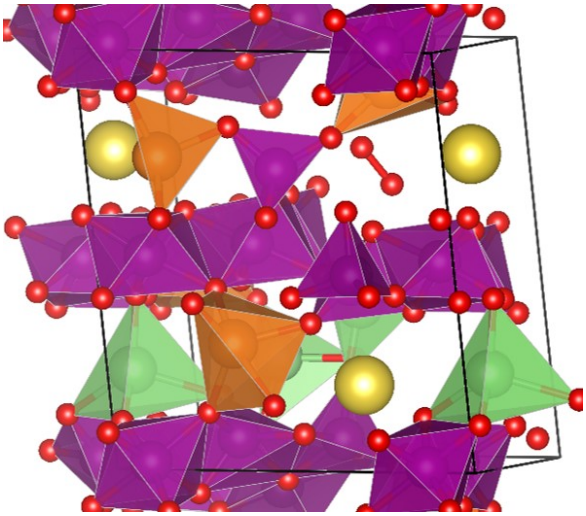

Figure 4.3: Comparison of coordination environments obtained from DFT geometries of Na, Li,and Mg before and after desodiation along with percentual occupation of octahedral (O), prismatic (P), and tetrahedral (T) sodium layer sites and octahedral TM layer sites per species after desodiation. In the sodiated state, all the sodium are in P sites and all the Li and Mg are in octahedral TM layer sites.

of $Na_{0.1}[Li_{0.15}Mg_{0.15}Mn_{0.7}]O_2$ was collapsed at a sodium concentration of 0.1 during the AIMD simulations, resulting in a strongly distorted environment for Na, Mg, and Li. This was accompanied by ion migrations including Mg (Figure 4.1d), and therefore, assignment of discrete coordination environments as in Figure 4.2 becomes difficult. The structure collapse is likely caused by the limited oxidation of manganese to 4+ in the octahedral environment, which will be discussed later.

For highly charged states (low Na concentrations), migration of Mn to different environments, e.g., tetrahedral, is required to achieve its oxidation to charges larger than 4+, resulting in migrations and collapse of the layered structure by cycling (cf. Figure 4.1d). Moreover, a strong oxygen redox is necessary for charge balancing in this compound, and oxygen dimer formation is observed in the AIMD simulation, which can be an indication of an irreversible oxygen loss that further destabilizes the structure (cf. Figure 4.1 and Figure 4.3). Although different ensembles and temperatures showed different amounts of migrated Mg and/or Li ions, still rather similar energies were obtained after DFT optimizations, e.g., for $Na_{0.1}[Li_{0.1}Mg_{0.05}Ni_{0.15}Mn_{0.7}]O_2$ at NVT-800 K and NPT-1 bar-300 K (cf. Figure

4.1d). This might suggest a shallow potential energy surface of layered oxide materials with many local minima at different degrees of migrations. Therefore, the proposed multi-level optimization approach including AIMD runs appears to be crucial to find favorable atomistic structures of this class of materials at high charge states that are prone to ion migrations between the TM and Na sites as well as sliding of O–TM–O layers with respect to each other.

Focusing on the most favorable atomistic model of pristine (z = 0.6, 0.7, and 0.75) and charged (z = 0.1) states for each case (Figure 4.2), structural changes on operation of the P2-$Na_z[Li_xMg_{0.3-x-y}Ni_yMn_{0.7}]O_2$ materials were analyzed. It should be noted that the applied multi-level optimization procedure for $Na_{0.1}[Mg_{0.15}Ni_{0.15}Mn_{0.7}]O_2$, $Na_{0.1}[Li_{0.15}Mg_{0.15}Mn_{0.7}]O_2$, and $Na_{0.1}[Li_{0.1}Mg_{0.05}Ni_{0.15}Mn_{0.7}]O_2$) was not performed for $Na_{0.1}[Mg_{0.3}Mn_{0.7}]O_2$ and $Na_{0.1}[Li_{0.1}Mg_{0.1}Ni_{0.1}Mn_{0.7}]O_2$ due to the large computational demand. For the latter two compounds, instead, the lowest energy structures from DFT optimizations, which are those with manually applied Li/Mg migration from TM to Na sites, were used for further analysis as shown in Figure 4.2. It is remarkable that only $Na_{0.1}[Li_{0.1}Mg_{0.1}Ni_{0.1}Mn_{0.7}]O_2$ shows a P2 phase with all the sodium being in prismatic coordinations after desodiation. In contrast, for the other three compounds, the sodium ions are exclusively in octahedral coordination (except for a tetrahedral coordination in $Na_{0.1}[Mg_{0.15}Ni_{0.15}Mn_{0.7}]O_2$, Figure 4.2). However, a phase transition from P2 to O2 appeared in the simulations for $Na_{0.1}[Mg_{0.30}Mn_{0.7}]O_2$, $Na_{0.1}[Mg_{0.15}Ni_{0.15}Mn_{0.7}]O_2$, and $Na_{0.1}[Li_{0.1}Mg_{0.05}Ni_{0.15}Mn_{0.7}]O_2$.

Therefore, it can be speculated that $Na_{0.1}[Li_{0.1}Mg_{0.1}Ni_{0.1}Mn_{0.7}]O_2$ did not undergo a phase transition to O2 because the multi-level optimization approach with AIMD was not performed for this compound. This finding highlights another advantage of the multi-level optimization approach as phase transitions can be studied directly without explicitly optimizing various phases through DFT optimizations. Moreover, $Na_{0.1}[Mg_{0.3}Mn_{0.7}]O_2$ underwent a phase transition to O2 without a MD step in the optimization but with manual migration of Mg in the starting structure for the DFT optimization.

The following general tendencies are found for alkali and alkaline metals: i) sodium ions occupy sites directly below TM vacancies, which can be explained by electrostatic interactions, and ii) Li and Mg avoid remaining in prismatic sites when migrated. These phenomena can be viewed as driving forces for the observed P2-to-O2 phase transition in $Na_{0.1}[Li_{0.1}Mg_{0.05}Ni_{0.15}Mn_{0.7}]O_2$, $Na_{0.1}[Mg_{0.3}Mn_{0.7}]O_2$, and $Na_{0.1}[Mg_{0.15}Ni_{0.15}Mn_{0.7}]O_2$. For the compounds containing lithium, a strong tendency for lithium migration is observed, and all lithium ions migrate with partial Li migration except for $Na_{0.1}[Li_{0.1}Mg_{0.1}Ni_{0.1}Mn_{0.7}]O_2$, which is most likely because no temperature was applied (i.e., no AIMD simulation) in the atomistic optimization procedure (Figure 4.2). These observations prove that Li is prone to migrate when introduced into the TM layer. For the $Na_{0.1}[Mg_{0.30}Mn_{0.7}]O_2$ and $Na_{0.1}[Mg_{0.15}Ni_{0.15}Mn_{0.7}]O_2$ cases, Mg appears to behave similar to Li with the difference being that a small portion appears to be stable in the TM layer. It appears that Mg cations can be stabilized in the TM layer by the vacancies created from lithium migration in $Na_{0.1}[Li_{0.1}Mg_{0.1}Ni_{0.1}Mn_{0.7}]O_2$ and $Na_{0.1}[Li_{0.1}Mg_{0.05}Ni_{0.15}Mn_{0.7}]O_2$. This is especially remarkable for $Na_{0.1}[Li_{0.1}Mg_{0.05}Ni_{0.15}Mn_{0.7}]O_2$, where during the AIMD simulations, only one Mg migration (out of two) was observed in one run at a high temperature of 800 K.

In contrast, in all the other runs, the Mg remained completely in the TM layer, indicating that Mg can be stabilized in the TM layer by vacancies. This may lead to improved long-term cycling performance of $Na_x[Li_{0.1}Mg_{0.05}Ni_{0.15}Mn_{0.7}]O_2$ and $Na_x[Li_{0.1}Mg_{0.1}Ni_{0.1}Mn_{0.7}]O_2$, in particular in the former case with less Mg migration. As the predicted desodiation-induced P2$\rightarrow$ O2 phase transition from our calculation does not lead to a large change in the *c* lattice parameter (*c* = 10.97 Å $\rightarrow$ 11.15 Å), we believe that $Na_x[Li_{0.1}Mg_{0.05}Ni_{0.15}Mn_{0.7}]O_2$ can be a promising cathode material that is even stable at highly charged states.

As the atomistic structure is from the AIMD simulation (Figure 4.1d), we already have a large number of vacancies in the TM layers as almost all (5 out of 6) Mg undergo migration from the TM to the Na layer during the AIMD run. Similar to the case of $Na_x[Mg_{0.3}Mn_{0.7}]O_2$, we also have oxidation of O anions close

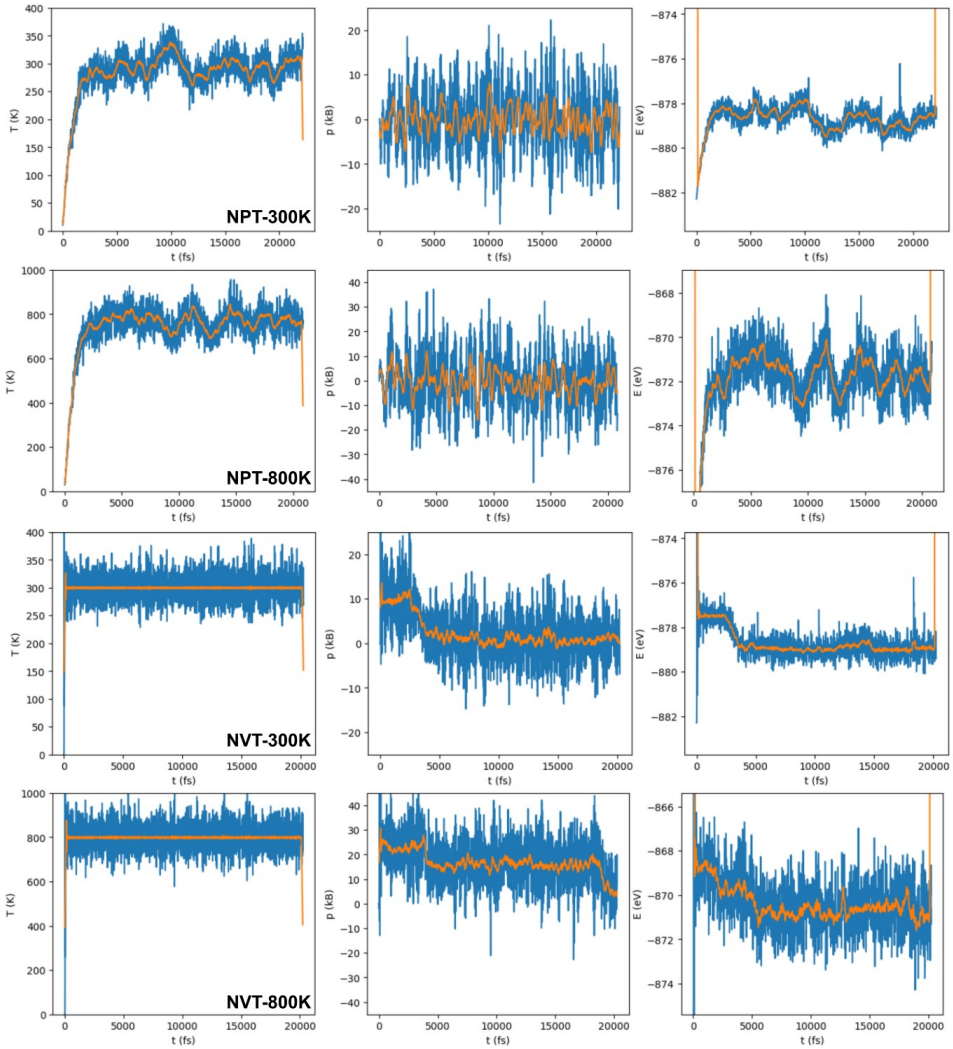

Figure 4.4: Temperature (left), stress/external pressure (middle), and energy (right) for $Na_{0.1}[Mg_{0.15}Ni_{0.15}Mn_{0.7}]O_2$ over the MD runs in NPT at 300 K, NPT at 800 K, NVT at 300 K, and NVT at 800 K (top to bottom). The blue color indicates raw data, and the orange color indicates the running average over 0.25 ps.

to the TM vacant sites in $Na_{0.6}[Mg_{0.15}Ni_{0.15}Mn_{0.7}O_2$. We would expect similar capacity for $Na_x[Mg_{0.3}Mn_{0.7}]O_2$ and $Na_{0.6}[Mg_{0.15}Ni_{0.15}Mn_{0.7}]O_2$ in the long term. This is expected as even though the concentration of TM vacancies (i.e., the Mg concentration) in the latter would likely be half of the former and its O anions

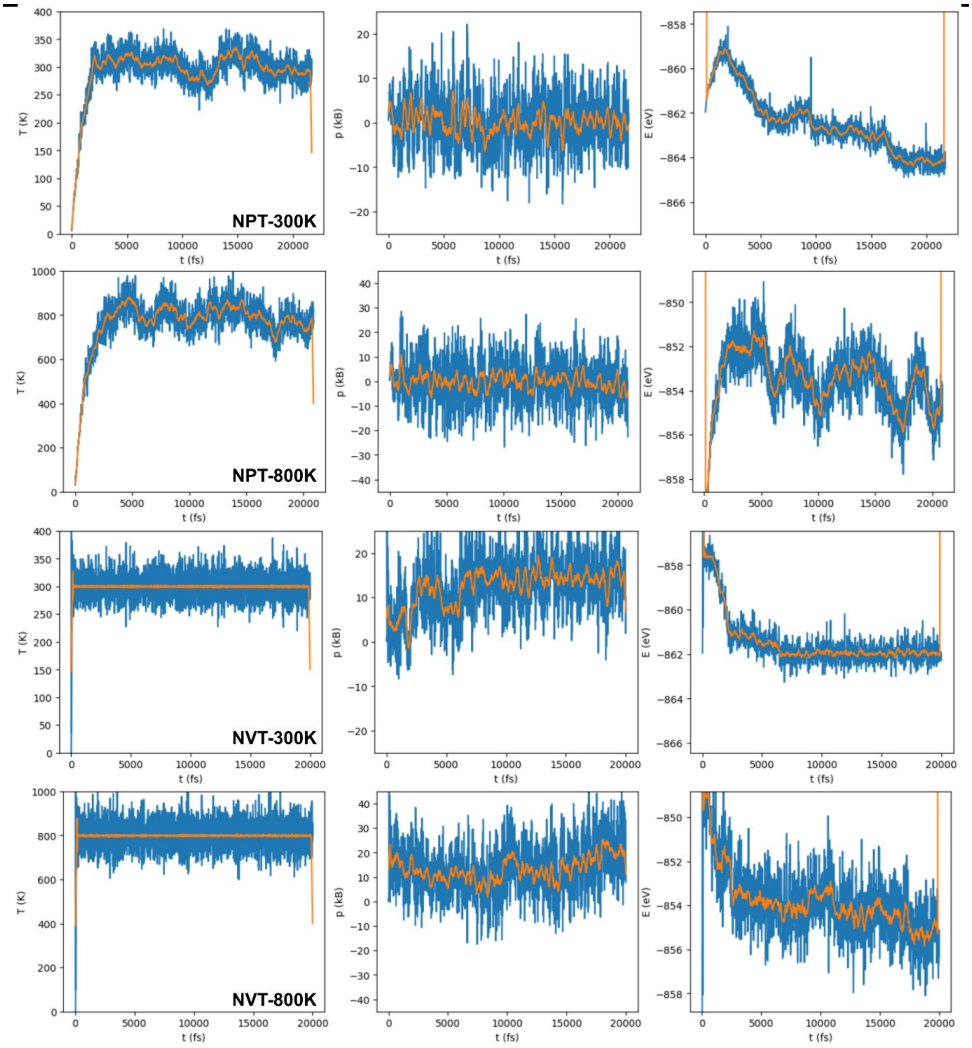

Figure 4.5: Temperature (left), stress/external pressure (middle), and energy (right) for $Na_{0.1}[Mg_{0.15}Li_{0.15}Mn_{0.7}]O_2$ over the MD runs in NPT at 300 K, NPT at 800 K, NVT at 300 K, and NVT at 800 K (top to bottom). The blue color indicates raw data, and the orange color indicates the running average over 0.25 ps.

experience lower oxidation in the presence of Ni, Ni is fully active in the case of $Na_{0.6}[Mg_{0.15}Ni_{0.15}Mn_{0.7}]O_2$. For the $Na_{0.75}[Li_{0.15}Mg_{0.15}Mn_{0.7}]O_2$ system, in which half of Mg is replaced by Li together with some additional amount of Na in the Na layer of $Na_{0.6}[Mg_{0.3}Mn_{0.7}]O_2$ (to maintain the charge neutrality), our

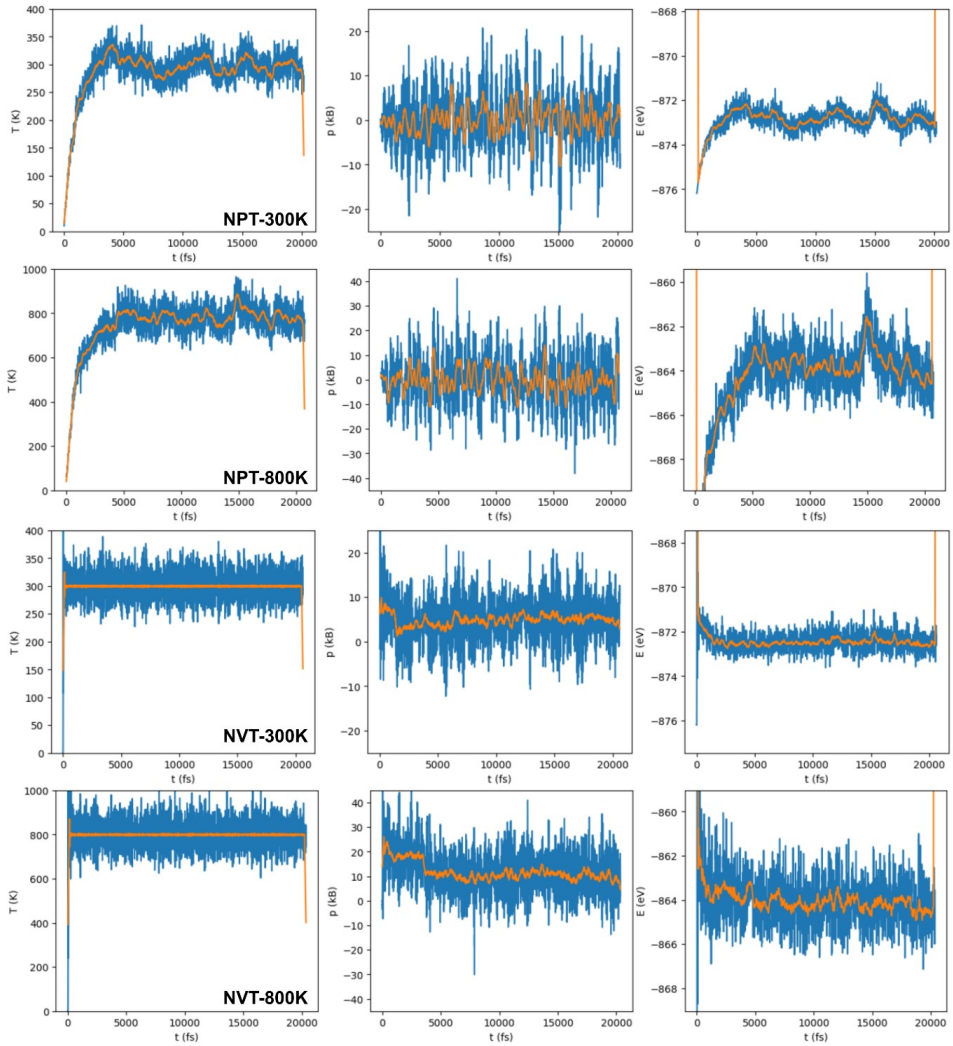

Figure 4.6: Temperature (left), stress/external pressure (middle), and energy (right) for $Na_{0.1}[Mg_{0.05}Li_{0.10}Ni_{0.15}Mn_{0.7}]O_2$ over the MD runs in NPT at 300 K, NPT at 800 K, NVT at 300K, and NVT at 800 K (top to bottom). The blue color indicates the raw data, and the orange color indicates the running average over 0.25 ps.

AIMD simulation showed a large structural distortion for the low Na concentration (charged state), which is driven by Li and Mg as well as Mn migration from the TM to Na layer (cf. Figure 4.1 and Figure 4.3). For the Ni-containing $Na_{0.7}[Li_{0.1}Mg_{0.1}Ni_{0.1}Mn_{0.7}]O_2$ and $Na_{0.7}[Li_{0.1}Mg_{0.05}\ Ni_{0.15}Mn_{0.7}]O_2$ systems with a

lower Li and Mg content compared to $Na_{0.75}[Li_{0.15}Mg_{0.15}Mn_{0.7}]O_2$, a similar trend as for the case of $Na_{0.60}Mg_{0.15}Ni_{0.15}Mn_{0.7}$ O_2 is observed: (i) high activity of Ni, namely Ni^{2+}/Ni^{4+}, and (ii) an increase in the percentage of active O anions with a decrease in the Ni content.

However, Figure 4.2 shows that Mg is more stable at TM sites in $Na_{0.7}[Li_{0.1}Mg_{0.1}Ni_{0.1}Mn_{0.7}]O_2$ and $Na_{0.7}[Li_{0.1}Mg_{0.05}Ni_{0.15}Mn_{0.7}]O_2$ compared to $Na_{0.60}[Mg_{0.15}Ni_{0.15}Mn_{0.7}]O_2$, where Mg migrates to Na sites to occupy octahedral and tetrahedral sites. Moreover, the latter shows two different Na site occupations for Na ions, namely, octahedral and tetrahedral sites. This observation might indicate a higher cyclability of $Na_{0.7}[[Li_{0.1}Mg_{0.1}Ni_{0.1}Mn_{0.7}]O_2$ and $Na_{0.7}[Li_{0.1}Mg_{0.05}Ni_{0.15}Mn_{0.7}]O_2$ with respect to $Na_{0.60}[Mg_{0.15}Ni_{0.15}Mn_{0.7}]O_2$ and $Na_{0.6}[Mg_{0.3}Mn_{0.7}]O_2$. The compound with significant disordering, namely $Na_{0.1}[Li_{0.15}Mg_{0.15}Mn_{0.7}]O_2$, is expected to have the highest capacity fading upon cycling among the studied systems. Based on the calculated atomistic structures, it appears that Li cannot be stabilized completely in the TM layer and that Mg ions are prone to migrate as well, as long as there are no vacancies in the TM layer. Nevertheless, $Na_x[Li_{0.15}Mg_{0.15}Mn_{0.7}]O_2$ in which TM vacancies created by Li migration (Figure 1d) could stabilize Mg at TM sites is shown to be unstable, which may be caused by too few redox active species being available for charge balancing in the desodiated state of the aforementioned compound, leading to an unstable structure including the migration of Mn, Mg, and Li. Introducing Ni in addition to Li and Mg to Mn sites appears to overcome this problem, resulting in stable compounds (i.e., $Na_{0.7}[Li_{0.1}Mg_{0.05}Ni_{0.15}Mn_{0.7}]O_2$ and $Na_{0.7}[Li_{0.1}Mg_{0.1}Ni_{0.1}Mn_{0.7}]O_2$) that can also stabilize Mg in the TM layer at low sodium concentrations.

Verification of theoretical and experimental multi-level optimization

To characterize the redox mechanisms, we performed DFT-HSE06 calculations on the sodiated and desodiated phases for $Na_x[Mg_{0.3}Mn_{0.7}]O_2$, $Na_x[Mg_{0.15}Ni_{0.15}Mn_{0.7}]O_2$, $Na_x[Li_{0.15}Mg_{0.15}Mn_{0.7}]O_2$, $Na_x[Li_{0.1}Mg_{0.1}Ni_{0.1}Mn_{0.7}]O_2$, and $Na_x[Li_{0.1}Mg_{0.05}Ni_{0.15}Mn_{0.7}]O_2$. To assign the charge state to the ions, we computed the magnetic moment (represented by the number of unpaired electrons

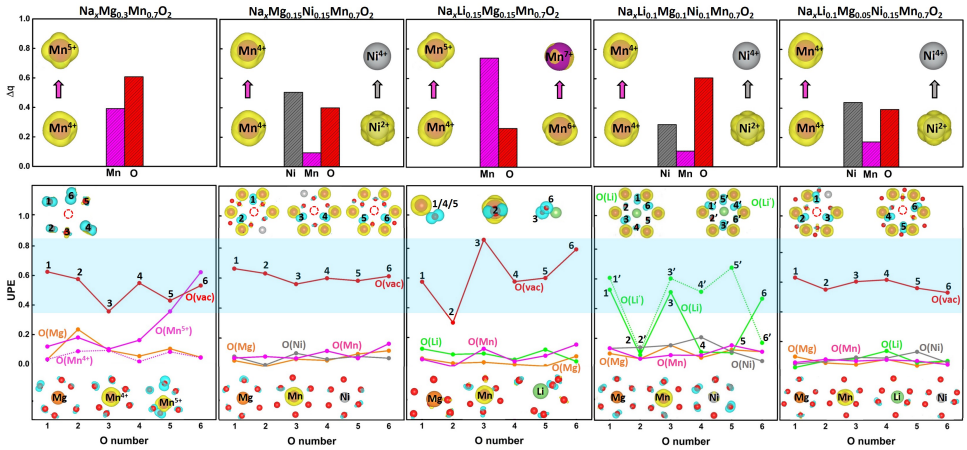

Figure 4.7: (Top) Computed normalized contribution of each active element to total capacity (δq) shown by bars using computed magnetic moments (i.e. number of unpaired electrons UPE) of ions presented in **Figure 4.8**. (Bottom) Computed UPEs of O anions close to the vacant sites (labled by O(vac)) as well as Li (labled by O(Li)), Mg (labled by O(Mg)), Mn (labled by O(LMn)), and Ni (labled by O(Ni)) in the charged systems. As O^{2-}/ has a UPE of 0, non-zero values of UPEs of oxygen anions in the charges systems show their oxidation values. Spin density differences on selected TMs (in top panel) as well as TMO_6 octahedra (in bottom panel) are presented as insets.

(UPEs)) of ions (Figure 4.7) as well as the spin density difference (SDD) to visualize the charging mechanism (Figure 4.7 and Figure 4.8). The computed redox process for the $Na_x[Mg_{0.3}Mn_{0.7}]O_2$ composition shows a large activity of oxygen anions, in particular for those close to the TM vacant sites, which are created after migration of Mg to Na sites (Figure 4.1). Moreover, to maintain the charge neutrality, a partial Mn oxidation from Mn^{4+} to Mn^{5+} occurs in $Na_x[Mg_{0.3}Mn_{0.7}]O_2$, which is most likely not feasible for Mn in an octahedral environment.

For this reason, a slight displacement of Mn from its initial octahedral site is observed in the DFT-optimized atomistic structure. A higher concentration of active O anions is expected for a larger concentration of TM vacant sites that can be created by the migration of Mg (or Li in other systems) from TM to Na sites in $Na_{0.6}[Mg_{0.3}Mn_{0.7}]O_2$. Therefore, we believe that partial unfavorable Mn^{4+}/Mn^{5+} redox can be suppressed by the increase in oxidation of O due to the further Mg migration by cycling. Substitution of half Mg by Ni in pristine $Na_{0.6}[Mg_{0.3}\ Mn_{0.7}]O_2$ does not affect the charge state of Mn (which was 4+) in the resulting system, namely $Na_{0.6}[Mg_{0.15}Ni_{0.15}\ Mn_{0.7}]O_2$; however, it prevents the unrealistic oxidation

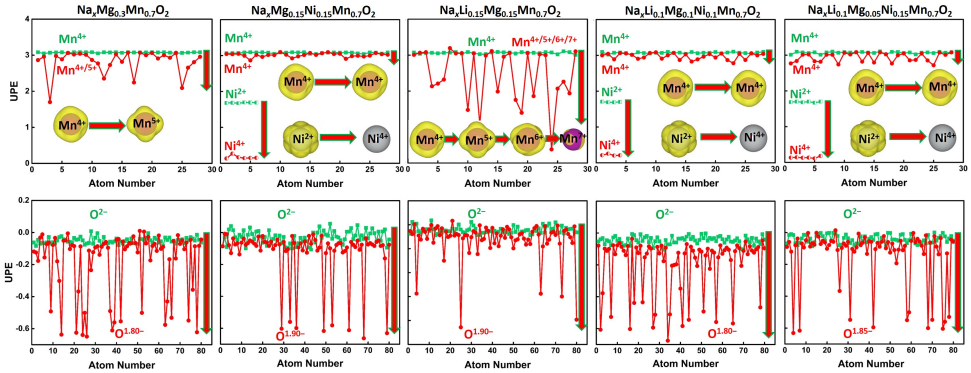

Figure 4.8: Computed UPE of Mn, Ni, and O ions in $Na_xMg_{0.3}Mn_{0.7}O_2$ (x=0.6(green), 0.1(red)), $Na_xMg_{0.15}Ni_{0.15}Mn_{0.7}O_2$ (x=0.6(green), 0.1(red)), $Na_xLi_{0.15}Mg_{0.15}Mn_{0.7}O_2$ (x=0.75(green), 0.1(red)), $Na_xLi_{0.1}Mg_{0.1}Ni_{0.1}Mn_{0.7}O_2$ (x=0.7(green), 0.1(red)), and $Na_xLi_{0.1}Mg_{0.05}Ni_{0.15}Mn_{0.7}O_2$ (x=0.7(green), 0.1(red)). Spin density difference (SDD) plots (at an iso-value of 0.03 unpaired electrons $\mathring{A}^{-3}$) for a few selected Mn and Ni ions are also shown. The arrow represents from the discharged to charged state.

of Mn from 4+ to 5+. Ni was determined to be a highly redox-active element and shows a charge-state change of Ni^{2+}/Ni^{4+} during the discharge/charge process. Migrated Mn cations in $Na_{0.1}[Li_{0.15}Mg_{0.15}Mn_{0.7}]O_2$ experience unrealistic oxidation of Mn^{4+} to Mn^{5+}, Mn^{6+}, and Mn^{7+} upon charging, which is accompanied by occupation of tetrahedral O cages. Oxygen also experiences oxidation with two oxygen-making dimers. According to our DFT results for the pristine case (x = 0.70), the average value of UPE on Mn and Ni cations is 3.07 and 1.70, showing a charge state of 3.93+ and 2.30+, respectively, on these cations (Figure 4.8). The UPE of O is -0.04, showing a charge of $\sim$1.96 -.

The desodiation(charging)-induced oxidation of each ion was then estimated by analyzing the change in its UPE with desodiation of x = 0.7 $\rightarrow$ 0.1. The UPE values of several Mn decreased to $\sim$2.8, showing further oxidation of Mn to 4.2, which as mentioned before is unrealistic and is probably due to the too large desodiation level considered in our simulation. We propose a higher initial and final Na concentration in our models (x = 0.70 and 0.10, respectively), which would likely lead to lower initial and final charges of Mn cations. The UPE of Ni changes dramatically on desodiation and becomes 0.14, showing a charge state of 3.86+. This result can also be observed in the computed SDD plot (Figure 4.6), which shows that

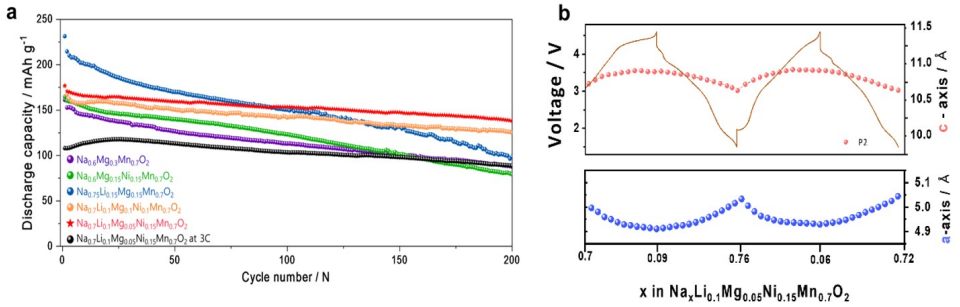

Figure 4.9: **(a)** Cyclability of various compositions at 0.1C and 3C. **(b)** the calculated *c*-axis parameters and *a*-axis parameters from operando XRD

4

the spin density of Ni changes significantly by charging. Figure 4.8 reveals that for x = 0.1, the average number of UPE on oxygen becomes ~ -0.15 with some oxygens having values of ~ -0.60 UPE. Generally, O anions with a lower degree of oxidation are those having Mn and Ni ions as nearest neighbors. However, the strongly oxidized O anions (Figure 4.8) are generally those next to the vacancies (created after Li and/or Mg migration), which can be clearly observed in SDD plots (Figure 4.7). As we already found that mainly Li ions migrate from TM to Na sites during charging, we removed the migrated Li+ ions from Na sites and recalculated UPEs and found that Mn and Ni cations have the same charge state as before; however, O experienced more oxidation as the average number of UPE on oxygen becomes ~ -0.20. Combining the computational results, the following redox mechanism is found: $Na^{1+}{}_{0.7}[Li^{1+}{}_{0.1}Mg^{2+}{}_{0.05}Ni^{2+}{}_{0.15}Mn^{4+}{}_{0.7}]O_2{}^{2-} \rightarrow Na^{1+}{}_{0.1}[Li^{1+}{}_{0.1}Mg^{2+}{}_{0.05}Ni^{4+}{}_{0.15}Mn^{4+}{}_{0.7}]O_2{}^{1.85-} \rightarrow Na^{1+}{}_{0.1}[Mg^{2+}{}_{0.05}Ni^{4+}{}_{0.05}Mn^{4+}{}_{0.7}]O_2{}^{1.80-}$. The AIMD simulations of $Na_{0.7}[Li_{0.1}Mg_{0.05}Ni_{0.15}Mn_{0.7}]O_2$ revealed a high stabilization of Mg cations in the transition metal layer.

Summarizing the above results, we found that a pivotal aspect of this investigation is the employment of a multi-step optimization approach, incorporating DFT-AIMD dynamics simulations to predict and verify the compositional and structural variations. This method theoretically guided our understanding of the migration of Mg and Li ions in $Na_x[A_yTM_{1-y}]O_2$, which significantly affects the stability and performance of materials. Notably, this study bridges the gap between theoretical

predictions and experimental validations, presenting a thorough investigation into the potential of P2-$Na_z[Li_xMg_{0.3-x-y}Ni_yMn_{0.7}]O_2$ (x = 0 — 0.15, y = 0 — 0.15, z = 0.6 — 0.75) compositions as cathode materials.

As predicted by theoretical studies, the introduction of elements with relatively large ionic radii, such as Li^+(0.76 Å), Mg^{2+} (0.72 Å), and Ni^{2+} (0.69 Å), in comparison with Mn^{4+} (0.53 Å), into the TM layer resulted in a more ordered crystal structure through the arrangement of the superstructure. In particular, the structural stability was enhanced by the covalent bonds involving Ni, ensuring that the ordering was maintained after discharge. Consequently, the oxygen redox reaction is retained, which is facilitated by the reversible migration of both Li and Mg ions from the TM to the Na layers during charging and their return to the TM layers during discharging. Benefiting from the structural stability (presence of the P2 phase during charging/discharging), the $Na_{0.7}[Li_{0.1}Mg_{0.05}Ni_{0.15}Mn_{0.7}]O_2$ cathode supports the oxygen redox reaction with good capacity retention over the long term (Figure 4.9a).

To highlight the advancements of the $Na_{0.7}[Li_{0.1}Mg_{0.05}Ni_{0.15}Mn_{0.7}]O_2$ material, we compared the electrochemical performance of oxygen-redox-assisted P2-type cathode materials (Figure 4.9). The $Na_{0.7}[Li_{0.1}Mg_{0.05}Ni_{0.15}Mn_{0.7}]O_2$ (represented by the red star) demonstrated remarkable electrode performance compared to other materials. These findings underscore the value of a multi-level optimization approach, particularly when guided by molecular dynamics simulations, as a crucial tool for identifying optimal atomic structures that promote high performance and stability. Therefore, this research offers a novel approach for the development of more efficient methods to investigate reliable cathode materials for SIBs.

4.4 Conclusions

In this study, we evaluated and optimized P2-type $Na_z[Li_xMg_{0.3-x-y}Ni_yMn_{0.7}]O_2$ (x = 0 — 0.15, y = 0 — 0.15, z = 0.6 — 0.75). Among several compositions, $Na_{0.7}[Li_{0.1}Mg_{0.05}Ni_{0.15}Mn_{0.7}]O_2$ exhibited the best performance in terms of structural stability, capacity, and retention. As designated, each of the elements played pivotal roles in inducing a stable oxygen redox reaction, and stable cycling performance. *o*-XRD analysis confirmed the occurrence of Na^+ de/sodiation within the P2 framework. The associated charge compensation progressed via Ni^{2+}/Ni^{4+}, Mn^{3+}/Mn^{4+}, and $O^{2-}/(O_2)^{n-}$, and migration of Li (not lattice-oxygen evolution) was the main trigger of the redox process of the lattice oxygen, as revealed by AIMD and DFT-studies. Our findings underscore the design of the reliable electrode materials, offering structural stability, enhanced operation voltage, and insights into the intricate mechanisms on cathode materials for SIBs.

4.5 References

1. J. Y. Hwang, S. T. Myung, Y. K. Sun, Chem. Soc. Rev. **2017,** 46, 3529.
2. M. Song, H. Tan, D. Chao, H. J. Fan, *Adv. Funct. Mater.* **2018,** 28, DOI 10.1002/adfm.201802564.
3. J. Y. Hwang, S. T. Myung, Y. K. Sun, *Adv. Funct. Mater.* **2018,** 28, DOI 10.1002/adfm.201802938.
4. A. Mendiboure, C. Delmas, P. Hagenmuller, *J. Solid State Chem.* **1985,** 57, 323.
5. J. Zhang, J. B. Kim, J. Zhang, G. H. Lee, M. Chen, V. W. H. Lau, K. Zhang, S. Lee, C. L. Chen, T. Y. Jeon, Y. W.Kwon, Y. M. Kang, *J. Am. Chem. Soc.* **2022,** 144, 7929.
6. B. Song, M. Tang, E. Hu, O. J. Borkiewicz, K. M. Wiaderek, Y. Zhang, N. D. Phillip, X. Liu, Z. Shadike, C. Li, L.Song, Y.-Y. Hu, M. Chi, G. M. Veith, X.-Q. Yang, J. Liu, J. Nanda, K. Page, A. Huq, Understanding the Low-Voltage Hysteresis of Anionic Redox in Na 2 Mn 3 O 7, n.d.
7. P. Gupta, S. Pushpakanth, M. A. Haider, S. Basu, ACS Omega. **2022,** 7, 5605.
8. J. Zhang, W. Wang, W. Wang, S. Wang, B. Li, *ACS. Appl. Mater. Interfaces.* **2019,** 11, 22051.
9. A. Konarov, J. U. Choi, Z. Bakenov, S. T. Myung, J Mater Chem A Mater 2018, 6, 8558.
10. J. W. Somerville, A. Sobkowiak, N. Tapia-Ruiz, J. Billaud, J. G. Lozano, R. A. House, L. C. Gallington, T.Ericsson, L. Häggström, M. R. Roberts, U. Maitra, P. G. Bruce, *Energy. Environ. Sci.* **2019,** 12, 2223.
11. N. Yabuuchi, M. Kajiyama, J. Iwatate, H. Nishikawa, S. Hitomi, R. Okuyama, R. Usui, Y. Yamada, S. Komaba, *Nat. Mater.* **2012,** 11, 512.
12. H. J. Kim, N. Voronina, K. Köster, A. Y. Kim, H. G. Jung, H. Kim, K. Yazawa, H. Yashiro, P. Kaghazchi, S. T.Myung, *Energy. Storage. Mater.* **2024,** 66, 103224.
13. W. Kang, Z. Zhang, P. K. Lee, T. W. Ng, W. Li, Y. Tang, W. Zhang, C. S. Lee, D. Y. Wai Yu, *J. Mater. Chem. A. Mater.* **2015,** 3, 22846.

14. N. Voronina, J. H. Yu, H. J. Kim, N. Yaqoob, O. Guillon, H. Kim, M. G. Jung, H. G. Jung, K. Yazawa, H. Yashiro,P. Kaghazchi, S. T. Myung, *Adv. Funct. Mater.* **2023,** 33, 202210423.

15. A. Konarov, H. J. Kim, N. Voronina, Z. Bakenov, S. T. Myung, *ACS. Appl. Mater. Interfaces.* **2019,** 11, 28928.

16. N. Voronina, M. Y. Shin, H. J. Kim, N. Yaqoob, O. Guillon, S. H. Song, H. Kim, H. D. Lim, H. G. Jung, Y. Kim, H.K. Lee, K. S. Lee, K. Yazawa, K. Gotoh, P. Kaghazchi, S. T. Myung, *Adv. Energy. Mater.* **2022,** 12, 202103939.

17. C. Zhao, Q. Yang, F. Geng, C. Li, N. Zhang, J. Ma, W. Tong, B. Hu, *ACS. Appl. Mater. Interfaces.* **2021,** 13, 360.

18. N. Yabuuchi, R. Hara, M. Kajiyama, K. Kubota, T. Ishigaki, A. Hoshikawa, S. Komaba, *Adv. Energy. Mater.* **2014,** 4, 201301453.

19. R. J. Clément, J. Billaud, A. Robert Armstrong, G. Singh, T. Rojo, P. G. Bruce, C. P. Grey, *Energy. Environ. Sci.* **2016,** 9, 3240.

20. E. N. Bassey, P. J. Reeves, M. A. Jones, J. Lee, I. D. Seymour, G. Cibin, C. P. Grey, *Chemistry of Materials.* **2021,** 33, 4890.

21. E. Boivin, R. A. House, J. J. Marie, P. G. Bruce, *Adv. Energy. Mater.* **2022,** 12, DOI 10.1002/aenm.202200702.

22. A. Konarov, J. H. Jo, J. U. Choi, Z. Bakenov, H. Yashiro, J. Kim, S. T. Myung, *Nano Energy.* **2019,** 59, 197.

23. X. Bai, M. Sathiya, B. Mendoza-Sánchez, A. Iadecola, J. Vergnet, R. Dedryvère, M. Saubanère, A. M. Abakumov,P. Rozier, J. M. Tarascon, *Adv. Energy. Mater.* **2018,** 8, 201802379.

24. R. A. House, J. J. Marie, M. A. Pérez-Osorio, G. J. Rees, E. Boivin, P. G. Bruce, *Nat. Energy.* **2021,** 6, 781.

25. R. A. House, U. Maitra, M. A. Pérez-Osorio, J. G. Lozano, L. Jin, J. W. Somerville, L. C. Duda, A. Nag, A. Walters,K. J. Zhou, M. R. Roberts, P. G. Bruce, *Nature.* **2020,** 577, 502.

26. N. Yabuuchi, R. Hara, K. Kubota, J. Paulsen, S. Kumakura, S. Komaba, *J. Mater. Chem. A. Mater.* **2014,** 2, 16851.

27. X. Wu, G. L. Xu, G. Zhong, Z. Gong, M. J. McDonald, S. Zheng, R. Fu, Z. Chen, K. Amine, Y. Yang, *ACS. Appl. Mater. Interfaces.* **2016,** 8, 22227.

28. B. Li, Z. Zhuo, L. Zhang, A. Iadecola, X. Gao, J. Guo, W. Yang, A. V. Morozov, A. M. Abakumov, J. M. Tarascon, *Nat. Mater.* **2023,** 22, 1370.

29. K. Okhotnikov, T. Charpentier, S. Cadars, *J. Cheminform.* **2016,** 8, 1-5.

30. P.E. Blöchl, *Physical. Review. B.* **1994,** 50, 17953

31. G. Kresse, *J. Furthmü.* **1996,** 16, 11169.

32. J. P. Perdew, K. Burke, M. Ernzerhof, *Phy. rev. lett.* **1996,** 18, 3865.

33. H. A. Posch, Iliam G. Hoover, F. J. Vesely, *Phys. rev. A.* **1986,** 33, 4253 .

34. M. P. Allen, D. J. Tildesley, Computer Simulation of Liquids, Oxford University Press, 2017.

35. M. Parrinello, A. Rahman, *Phys. Rev. Lett.* **1980,** 45, 1196.

36. M. Parrinello, A. Rahman, *J. Appl. Phys.* **1981,** 52, 7182.

37. A. V. Krukau, O. A. Vydrov, A. F. Izmaylov, G. E. Scuseria, *Journal of Chemical Physics.* **2006,** 125, DOI 10.1063/1.2404663.

38. K. Momma, F. Izumi, *J. Appl. Crystallogr.* **2011,** 44, 1272.

5

On the origin of phase transition suppression of P2-$Na_{0.67}MnO_2$ by substitution of Mn with Li

Abstract: Mn-based layered oxides are promising cathode materials for Na-ion batteries. However, one of the main drawbacks of these materials is their low cyclability, which is mainly due to the phase transition during charge/discharge process. The well-known P2-$Na_{0.67}MnO_2$ compound undergoes a severe phase transition of P2→O2 during charging ($Na_{0.11}MnO_2$). It has been proposed that this behavior is because of the desodiation-induced change in the Jahn-Teller (J-T) activity of Mn after its oxidation from 3+ to 4+. Further studies have shown that replacing a sufficient fraction of Mn^{3+} by low valent metals such as Li^+ and/or Ni^{2+} can suppress the phase transition.

In this work, we show that the driving force of the phase transition is indeed the oxidation of Mn^{3+} to Mn^{4+} but not the suppression of J-T activity with desodiation. Combining density functional theory calculations and electrostatic analyses indicates that the main factor stabilizing the P2 phase is the Na-Mn interaction, which strongly favors this phase over the O2 phase. Desodiation induced-weakening of this interaction leads to the formation of O2-$Na_{0.11}MnO_2$, which is driven by O-O interaction. We explain that the reason of this phase-transition suppression by substitution of Mn by Li is that Li at TM sites of $Na_xLi_{0.22}Mn_{0.78}O_2$ can retain the P2 preference over O2 even after x = 0.67→0.11 desodiation. This is because the Na-Mn interaction is much weaker (more favorable) for the P2 phase, and this energy preference remains almost

unchanged after desodiation. The absorption energy of Na at Na sites close to Li_{TM} is much stronger than that of Na sites close to Mn_{Mn}, and it is considerably more favorable for P2 phase. As the overall Na absorption energy (dictated by Na-Mn repulsion) is mainly determined by the nearest Na-Mn neighbor interaction, which does not change much with desodiation, no phase transition to O2 occurs for $Na_xLi_{0.22}Mn_{0.78}O_2$ at x = 0.11. The results of this work show that the phase stability of Na-based layered oxide materials is driven by electrostatic forces, which can be tuned by substitution of Mn by a metal ion of appropriate charge and concentration.

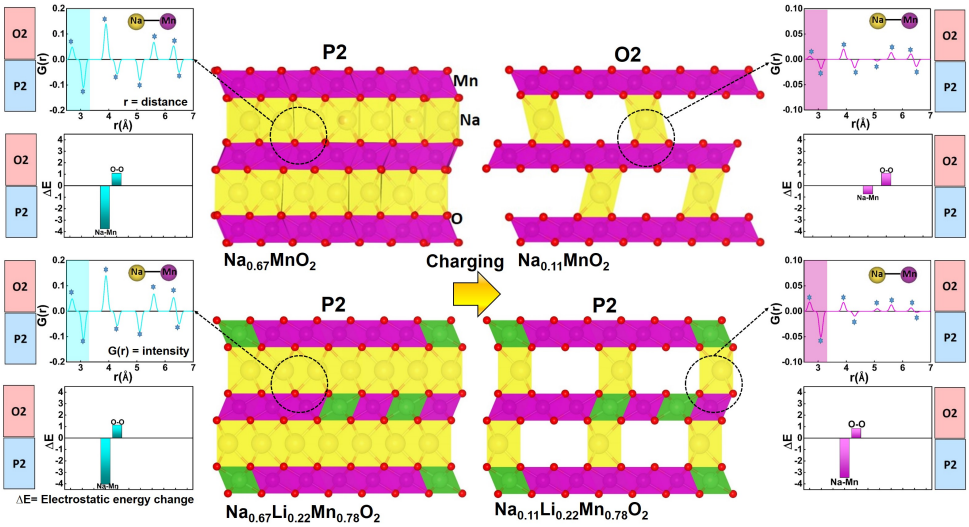

This chapter is based on the publication:
N. Yaqoob, M. Huijben, P. Kaghazchi, (submitted).

5.1 Introduction

After the successful application of Li-ion batteries (LIBs) in portable electronic devices and electric vehicles, significant attention has been directed to sodium-ion batteries (SIBs) because of the low cost and natural abundance of sodium (Na) resources[1−2]. Mn-based layered oxides, $Na_x[M_{1-y}Mn_y]O_2$ (M: metals), are perhaps among the most promising cathode materials because of their low toxicity and high energy density[3−4]. The basic compound Na_xMnO_2 can be classified into P- and O-type depending on the site occupation preference for Na^+, prismatic or octahedral coordination, respectively[5]. The most common layered oxide types are P2 and O3, where the numbers represent the number of distinguishable oxygen layers stacking arrangements per unit cell. Compounds with O3 phases often undergo multiple phase transitions, such as O3-P3-O3′-O1 during charging with a gradual capacity loss during cycling[6]. The P2-type materials generally show a better rate performance and higher initial capacity than O3-type[7−10]. Delmas et al.[5] introduced, to our knowledge, the first work on the structural properties of P2-$Na_{0.7}MnO_2$. They found that there is a P2→O2 phase transition during charging. This behavior decreases the capacity of this compound with cycling and was assigned to the cooperative Jahn–Teller distortion of Mn^{3+}.

To solve this issue, Dahn et al.[11] substituted Mn with Ni and reported P2-$Na_{0.67}Ni_{0.33}Mn_{0.67}O_2$ with a capacity of 173 $mAhg^{-1}$. However, the drastic volume change of ∼23% after desodiation, originating from the P2→O2 phase transition, still decreases the capacity retention of this material. Additionally, Konarav et al.[12] reported a reduction in the volume change (∼13%) in P2-$Na_{0.67}Ni_xMn_{1-x}O_2$ by varying the Ni-content from x = 0.0 to 0.2. They found that the P2-$Na_{0.67}Ni_{0.2}Mn_{0.8}O_2$ material shows the best electrochemical performance compared to other Ni contents. The small volume changes in P2-$Na_{0.67}Ni_{0.2}Mn_{0.8}O_2$ was possible because of $Ni^{2+} \rightarrow Mn^{3+}$ substitution, which can suppress Jahn–Teller distortions. However, suppression of P2→O2 phase transition during charging is still challenging. In order to enhance the electrochemical properties of P2-type materials, Yabuuchi et al.[13] reported that the P2→O2 phase transition in P2-type

$Na_{0.67}Mn_{0.5}Fe_{0.5}O_2$, which showed a reversible capacity of 190 $mAhg^{-1}$ with electrochemically active Mn^{3+}/Mn^{4+} and Fe^{3+}/Fe^{4+} redox processes, is suppressed. However, they found that a reversible P2→P4 phase transition occurs at *x* = 0.13 during charging. Bruce et al.[14] applied Ni besides Fe to partially substitute Mn, and found that their synthesized cathode material, P2-$Na_{0.67}Ni_{0.17}Fe_{0.33}Mn_{0.50}O_2$, also shows the P2→OP4 phase transition during charging and less volume change, as compared to the typical P2→O2 phase transition, which enhances the capacity retention. These previous studies show the importance of doping/substitution to stabilize the P2-Na_xMnO_2 structure by minimizing/reducing the effect of Jahn–Teller distortion in Mn^{3+} and by suppressing the volume change during charging. An improved cycling stability and better capacity retention can be achieved not only by redox-active transition metal substituents such as Ni and Fe but also by electroinactive elements such as Li and Mg in P2-Na_xMnO_2 structure.

Yabuuchi et al.[15] reported that the Li-substitution at Mn-sites can suppress the P2→O2 phase transition in P2-$Na_{0.75}Li_{0.25}Mn_{0.75}O_2$. Density functional theory (DFT) has also been applied to gain further insight into this mechanism. For example, Yang et al.[16] studied P2-$Na_{0.67}Li_{0.2}Ni_{0.2}Mn_{0.6}O_2$ using experimental measurements and DFT calculations. They were able to suppress the P2→O2 phase transition in $Na_{0.67}Li_{0.2}Ni_{0.2}Mn_{0.6}O_2$ upon charging and showed a reversible capacity of 110 $mAhg^{-1}$ over 100 cycles. Their DFT analysis found that the capacity originated from both cationic and anionic redox processes. Further computational studies show that the extraction of sodium ions increases the oxidation state of manganese during charging. This results in a higher concentration of Mn^{3+}, which is prone to Jahn-Teller (J-T) distortions. It has been proposed that these J-T distortions alter the MnO_6 octahedra by changing bond lengths and angles, ultimately destabilizing the P2-structure leading to structural phase transitions[17–18]. Experimental studies have also proposed that the J-T distortion is a driving force of structural instability and phase transition during charging[19]. The fundamental mechanism behind the P2→O2 phase transition in P2-Na_xMnO_2 and the role of low valent substitution (Li^+, Ni^{2+}, and Fe^{2+}) to stabilize the P2 structure during charging/discharging

is, however, to our knowledge still unclear and a more detailed understanding is required. In this work, we study the origin of the P2→O2 phase transition as well as the impact of Li → Mn substitution on the phase stability and transition in P2-Na_xMnO_2. Our DFT-PBE calculation reproduces J-T distortions for $Na_{0.67}MnO_2$ (as also reported earlier by Delmas[15], Langella et al.[17] and Jung et al.[18]) and no J-T distortions for $Na_{0.67}Li_{0.22}Mn_{0.78}O_2$, and confirms phase transition in the former and its suppression in the latter case. Our simple electrostatic model without considering J-T distortions also predicts the same trend as DFT which shows the key role of electrostatic interaction rather than J-T distortion on the phase stability. Moreover, for the first time, we also provided a simple quantitative explanation for the phase stabilization (as-synthesized material) and transition (during operation) of P2-$Na_{0.67}MnO_2$ materials with and without Li→Mn substitution, which is an important phenomenon in Na-ion batteries. The aim of this study is to find a quantitative explanation for this important phenomenon for Na-ion batteries.

5.2 Method

To obtain the most favorable structures of P2-Na_xMnO_2, P2-$Na_xLi_{0.06}Mn_{0.94}O_2$ and P2-$Na_xLi_{0.22}Mn_{0.78}O_2$, with different *x* values, we modeled and calculated the total Coulomb energy (E_C) of a large number of likely structures. Total Coulomb energy (E_C) calculations on possible combinations were carried out using the so-called supercell code[20]. We computed electrostatic energies (E_C) for specific elements using the Pymatgen code[21]. By performing DFT-PBE calculation on the electrostatically most favorable configuration, we determined the lowest total energy structure for each Na concentration and used the optimized geometries for further DFT-PBE-D3 and -HSE06 calculations. The total number of considered configurations for E_C calculation and the charge states of ions are discussed in detail. Spin-polarized DFT calculations were performed using the projector augmented wave (PAW) potential method[22] implemented in the Vienna Ab Initio Simulation Package (VASP) code[23]. The Perdew–Burke–Ernzerhof (PBE)[24] form of generalized gradient approximation (GGA) was used for the exchange and

correlation potential. The dispersion D3 correction by Grimme[25] was applied to calculate atomistic structures. We have not applied the PBE+U[26] functional for geometry optimization as it is known from previous theoretical works that it does not provide a better description for lattice parameters compared to PBE[27–28]. Performing geometry optimizations with Heyd–Scuseria–Ernzerhof (HSE06)[29] functional is not a common approach to compute the atomistic structure either, because HSE06 is often used for calculating electronic properties such as band gaps and magnetic moments. Moreover, it's computationally expensive and usually doesn't change the structure much compared to PBE[30]. Therefore, it is a more common approach to optimize the geometry with PBE first, then use this optimized geometry and perform single-point calculations with HSE06 functional[31–33]. Therefore, we used HSE06 functional to compute the electronic structure (i.e. number of unpaired electrons (N_{unp}) on elements and spin density difference (SDD) plots).

Na_xMnO_2, $Na_xLi_{0.06}Mn_{0.94}O_2$ and $Na_xLi_{0.22}Mn_{0.78}O_2$ were modeled by 3×6×1 supercells with the following number of atoms per supercell: P2-$Na_{0.67}MnO_2$ ($Na_{24}Mn_{36}O_{72}$), P2-$Na_{0.11}MnO_2$ ($Na_{24}Mn_{36}O_{72}$), P2-$Na_{0.67}Li_{0.06}Mn_{0.94}O_2$ ($Na_{24}Li_2Mn_{34}O_{72}$), P2-$Na_{0.11}Li_{0.06}Mn_{0.94}O_2$ ($Na_4Li_2Mn_{34}O_{72}$), P2-$Na_{0.67}Li_{0.22}Mn_{0.78}O_2$ ($Na_{24}Li_8Mn_{28}O_{72}$) and P2-$Na_{0.11}Li_{0.22}Mn_{0.78}O_2$ ($Na_4Li_2Mn_{34}O_{72}$). Afterwards, we also studied the influence of desodiation on the phase stability of ($Na_xLi_yMn_{1-y}O_2$) materials by using a large supercell (3x6x3) to decrease the uncertainty in the energy differences. A Gamma-centered k-point mesh of 2×1×2 and an energy cut off of 500 eV were applied. An electronic and a force convergence criterion of 10^{-4} eV and 2 × 10^{-2} eV/Å, respectively, were used for DFT calculations. Atomistic structures and SDD plots were visualized with the VESTA program[34].

To obtain the most favorable structures in Na_xMnO_2, $Na_xLi_{0.06}Mn_{0.94}O_2$ and $Na_xLi_{0.22}Mn_{0.78}O_2$, we calculated the total Coulomb energy (E_C) of a large number of likely structures. By performing DFT-PBE calculation on the electrostatically most favorable configuration, we determined the lowest total energy structure for each Na concentration and used the optimized geometries for further DFT-PBE-D3

and -HSE06 calculations. The total number of considered configurations for E_C calculation and the charge states of ions are discussed below in detail.

P2-Na$_{0.67}$MnO$_2$ (Na$_{24}$Mn$_{36}$O$_{72}$): $\frac{36!}{24!12!}$ = 1.25E+9, structures with 24 Na ions in 36 Na sites; charges of 1+ for Na, 3.33+ for Mn, 2- for O.

P2-Na$_{0.11}$MnO$_2$ (Na$_4$Mn$_{36}$O$_{72}$): $\frac{24!}{4!20!}$ = 1.06E+4, structures with 4 Na ions in 24 Na sites; charges of 1+ for Na, 3.889+ for Mn, 2- for O.

We used the most favorable structure of high and low Na-concentration from Na$_x$MnO$_2$ to study Li arrangements in Na$_x$Li$_{0.06}$Mn$_{0.94}$O$_2$.

P2-Na$_x$Li$_{0.06}$Mn$_{0.94}$O$_2$ (Na$_{24}$Li$_2$Mn$_{34}$O$_{72}$ or Na$_{24}$Li$_2$Mn$_{34}$O$_{72}$): $\frac{36!}{2!34!}$ = 630 structures with 2 Li and 34 Mn ions in 36 TM sites; charges of 1+ for Li/Na, 3.47+ for discharged Mn and 4+ for charged Mn, and 2- for O in discharged state and 1.972- for O in the charged state.

P2-Na$_{0.67}$Li$_{0.22}$Mn$_{0.78}$O$_2$ (Na$_{24}$Li$_8$Mn$_{28}$O$_{72}$): Modelling of $\frac{36!}{24!12!} \cdot \frac{36!}{28!8!}$ = 3.78E+16 structures with 24 Na ions in 36 Na sites as well as 28 Mn ions and 8 Li ions in 36 TM sites is computationally a formidable task due to the large number of possible configurations. Therefore, we created $\frac{36!}{24!12!}$ = 1.25E+9 structures with 24 Na ions in 36 Na sites and fixed the TM with charge states of 1+ for Na, 3.333+ for Mn and 2- for O. After that we fixed Na-ions and created $\frac{36!}{28!8!}$ = 3.03E+7 structures with 28 Mn ions in 28 TM sites. To find the position of 8 Li ions in (Na$_{36}$Mn$_{36}$O$_{72}$), we fixed 24 Na and 28 Mn ions in their determined Na and Mn sites and studied Li arrangement in the remaining unoccupied Na and Mn sites. We performed E_C on 3 possible configurations: i) all Li-ions in Na-sites, ii) all Li-ions in Mn-sites, and iii) half Li-ions in Na sites and half in Mn sites. Then, based on electrostatic analysis we found the second configuration to be favorable.

P2-Na$_{0.11}$Li$_{0.22}$Mn$_{0.78}$O$_2$ (Na$_4$Li$_8$Mn$_{28}$O$_{72}$): $\frac{24!}{4!20!}$ = 1.06E+4 structures with 4 Na ions in 24 Na sites; charge of 1+ for Na/Li, 4+ for Mn for both Na-concentrations and 2- and 1.72- for O for discharged and charged systems respectively. Charge state of elements in the case of the Li-migration from TM to Na-sites and the one with Li-vacancy (removed Li ions from Na-sites) in our Coulomb calculations are also coming from DFT-calculations. We also considered more oxidation in the

Li-vacancy (removed Li ions from Na-sites) system to keep the charge neutrality of the system because of the removal of Li-ions.

5.3 Results and Discussion

5.3.1 Infleunce of desodiation on phase stability

The most favorable atomistic structure for each compound and Na concentration, as well as their corresponding relative electrostatic energies are presented in Fig. 5.1. We studied the influence of desodiation on the phase stability of P2-$Na_xLi_yMn_{1-y}O_2$ materials, by computing the energy difference of P2, O2, and O3 phases as a function of Na (x = 1.00, 0.67, and 0.11) and Li (y = 0, 0.06, 0.22) concentrations using DFT-PBE (Fig. 5.2). For the fully sodiated case of $Na_{1.00}MnO_2$, the O3 phase is more favorable than the P2 and O2 phases which agrees with the previous experimental study by Xiaohua et al.[35]. With a x = 1.0→0.67 decrease in Na concentration, the P2 phase becomes more stable than O3 and O2 phases for Na_xMnO_2 by 13 meV and 23 meV (per formula unit) respectively. Stabilization of the P2 phase has also been reported by experimental measurements from Delmas et al.[5].

For the desodiation structures, we focused on P2 and O2 phases. After desodiation from x = 0.67→0.50, the P2 phase remains more stable by 15 meV than the O2 phase. However, after further desodiation the Na_xMnO_2 system undergoes a P2→O2 phase transition at x = 0.17, as the O2 phase is 2 meV more stable than the P2 phase. With a further decrease in Na-concentration (x = 0.11), the O2 phase remains more stable than the P2 phase (by 4 meV per formula unit). Our results indicating the P2→O2 phase transition during charging is consistent with experimental results by Delmas et al.[5] and Dahn et al.[11]. DFT calculations show the following phase transitions to occur for x = 1.00→0.67→0.50→0.17→0.11: O3→P2→P2→O2→O2. The DFT calculations indicate that in the case of $Na_{1.00}Li_{0.06}Mn_{0.94}O_2$ (Fig. 5.2), in which 6% of Mn is substituted with Li, the P2 phase is more favorable than the O2 and O3 phases. For the Na concentration of x = 0.67, the P2 phase remains more favorable for Li concentrations of y = 0.06 ($Na_{0.67}Li_yMn_{1-y}O_2$) showing similar behavior to the case

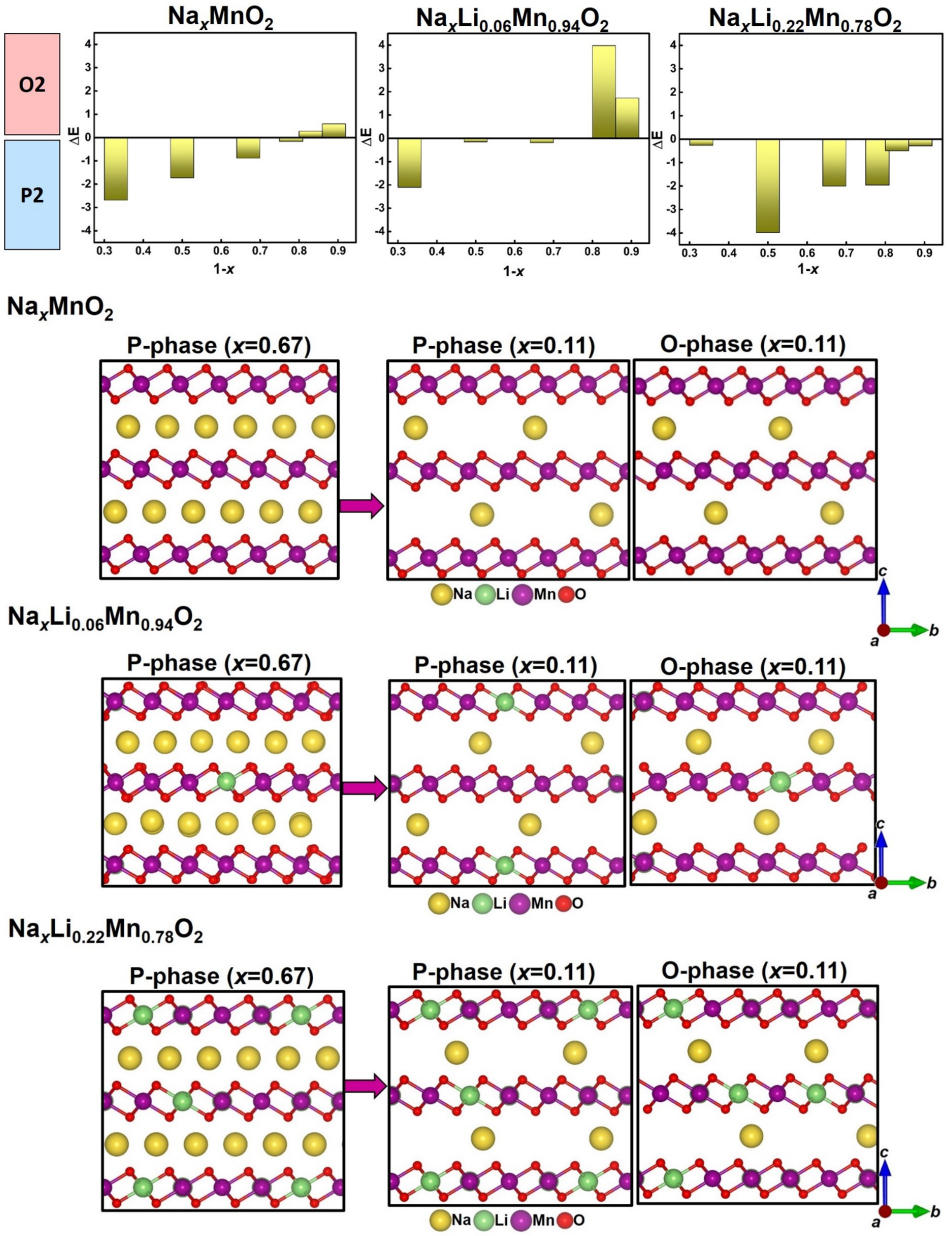

Figure 5.1: (Top) Computed electrostatic energy difference between the P2 and O2 phase ΔE = $E_{\text{tot}}^{\text{P2}}$ - $E_{\text{tot}}^{\text{O2}}$ versus Na-concentration using the Ewald summation (with point charges). (Bottom) Side views of atomistic structures.

of y = 0.0. Furthermore, for $Na_xLi_{0.06}Mn_{0.94}O_2$ (x = 0.67), our DFT-PBE calculation shows that the P2 phase is more stable than the O2 phase by 30 meV (per formula unit) and after desodiation from x = 0.67 to 0.11, a P2→O2 phase transition occurs and the O2 phase becomes more stable than the P2 phase by 20 meV per formula unit. This means that with 6% Li at Mn sites there is only one phase transition occurring: P2→P2→O2 for desodiation of x = 1.00→0.67→0.11. After increasing the substitution of Mn by Li to 22% the P2 phase remains the most favorable in $Na_{1.00}Li_{0.22}Mn_{0.78}O_2$ (Fig. 5.2). For the Na concentration of x = 0.67, the P2 phase forms for Li concentrations of y = 0.22 ($Na_{0.67}Li_yMn_{1-y}O_2$) similar to the cases of y = 0.0 and y = 0.06, which agrees well with experimental measurements by Myung et al.[36]. However, with such large amount of Li on the Mn sites $Na_xLi_{0.22}Mn_{0.78}O_2$ there is no phase transition occurring, and the P2 phase is always more stable than the O2 phase by 11 meV and 4 meV (per formula unit) for high (x = 0.67) and low (x = 0.11) Na-concentrations respectively. Experimental studies by Myung et al.[36] also show that 22% of Li-doping in $Na_{1.00}MnO_2$ (x = 0.67, 0.11) can suppress the phase transition during charging. The absence of a desodiation-induced phase transition

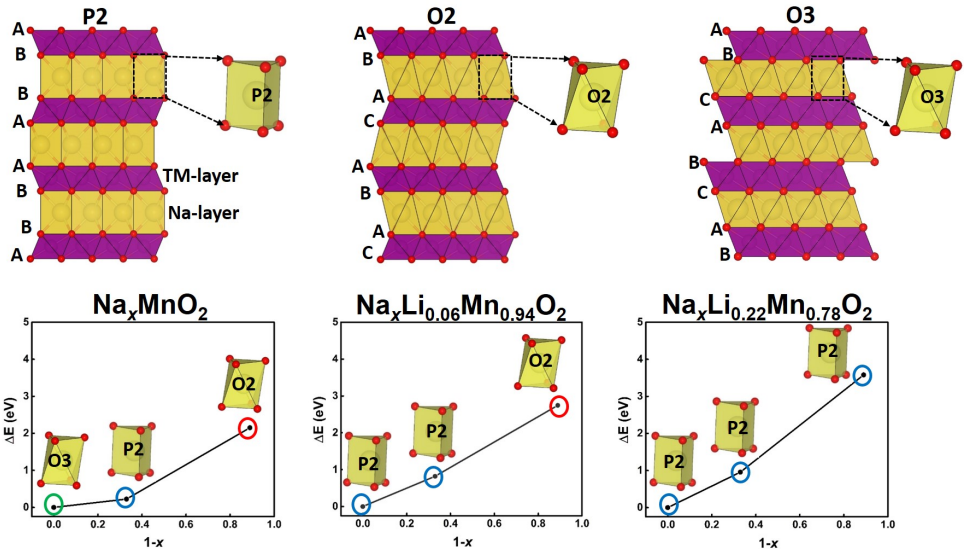

Figure 5.2: Calculated energy difference ΔE (per formula unit) between the O3, P2 and O2 phase versus Na-concentration using DFT-PBE for the most favorable phases for each Li-concentration.

has also been reported by Tarascon et al. for ($Na_xLi_yMn_{1-y}O_2$) with larger values of y = 0.33[37]. These results indicate a strong influence of Li on the phase stability of $Na_xLi_yMn_{1-y}O_2$.

5.3.2 lattice parameters change

Our DFT calculations show that the lattice parameter *a* decreases with a reduction of the Na-concentration from 0.67 to 0.11 for all studied systems (Table 5.1) due to the oxidation of Mn and O, which will be discussed later. The lattice parameter *c* contracts strongly after desodiation from 0.67 to 0.11 for the cases in which either no Li or a small amount of Li exist at the TM sites ($Na_xLi_yMn_{1-y}O_2$ y$\leq$0.06), which is because of the phase transition as well as migration of half of the Li cations from TM to Na sites after desodiation. However, the decrease in *c* parameter in the compound with a high amount of Li at TM sites, namely $Na_xLi_{0.22}Mn_{0.78}O_2$, in which no P2$\rightarrow$O2 phase transition occurs, is very small. The small decrease in *c* parameter is most likely due to the Li-migration from TM to Na-sites during charging. An experimental study by Tarascon et al.[37] on O3-$NaLi_{0.33}Mn_{0.67}O_2$ also indicates Li migration from TM to Na-site during charging and the presence

Table 5.1: Calculated lattice parameters in Å of NaMO, NaL0.06MO and NaL0.22NMO using DFT-PBE and DFT-PBE-D3 for discharged and charged states.

	PBE		**PBE-D3**	
System	***a*** **[Å]**	***c*** **[Å]**	***a*** **[Å]**	***c*** **[Å]**
P2-$Na_{0.67}MnO_2$	2.88	11.08	2.86	10.94
O2-$Na_{0.11}MnO_2$	2.87	10.38	2.857	10.10
P2-$Na_{0.67}Li_{0.06}Mn_{0.94}O_2$	2.870	11.07	2.86	10.93
O2-$Na_{0.11}Li_{0.06}Mn_{0.94}O_2$	2.869	10.31	2.85	10.28
O2-$Na_{0.11}Li_{0.03}Mn_{0.94}O_2$	2.87	10.82	-	-
P2-$Na_{0.67}Li_{0.22}Mn_{0.78}O_2$	2.89	10.99	2.86	10.83
P2-$Na_{0.11}Li_{0.22}Mn_{0.78}O_2$	2.84	10.83	2.83	10.34
P2-$Na_{0.11}Li_{0.11}Mn_{0.78}O_2$	2.85	11.08	-	-

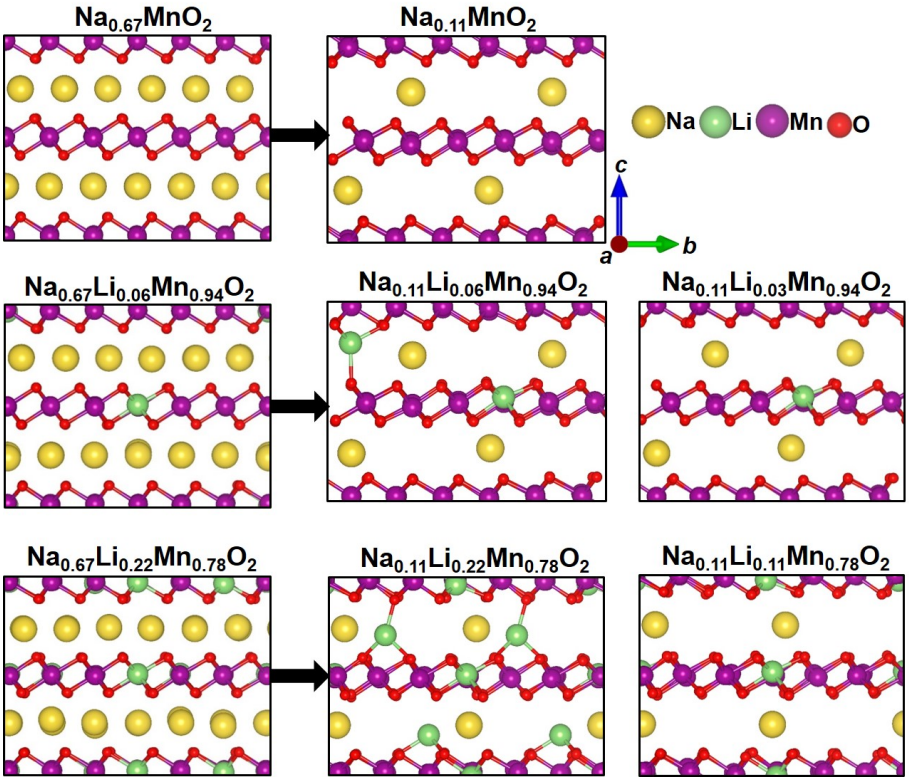

Figure 5.3: Side views of computed atomistic structures of Na_xMnO_2, $Na_xLi_{0.06}Mn_{0.94}O_2$ and $Na_xLi_{0.22}Mn_{0.78}O_2$ systems with x = 0.67 and 0.11 using DFT-PBE. Arrow represents from discharged to charged state.

of Li in the Na-layer leads to a decrease in the *c* parameter with respect to a discharged system which is consistent with our findings. In the discharged state of Li-doped compounds, Li ions occupy TM sites, but upon charging they migrate from TM to Na sites (see Fig. 5.3). To determine whether the migrated Li ions from TM to Na sites stay at the Na sites or move to the surface of the cathode during charging, we removed the Li-ions from Na-site in $Na_{0.11}Li_{0.06}Mn_{0.94}O_2$ and $Na_{0.11}Li_{0.22}Mn_{0.78}O_2$ and optimized both structures and lattice parameters. An expansion in the *c*-value was found for this model, which agrees with the *o*-XRD measurement by Myung et al.[36]. This result indicates a spontaneous migration of fractional Li ions from TM to Na sites and subsequent segregation to the surface of $Na_{0.11}Li_{0.22}Mn_{0.78}O_2$. Therefore, we conclude that most of the

migrated Li-ions from TM to Na sites do not stay in those Na sites, but segregate to the surface of the cathode consistent with previous study[36]. Therefore, we used $Na_{0.11}Li_{0.03}Mn_{0.94}O_2$ and $Na_{0.11}Li_{0.11}Mn_{0.78}O_2$ to calculate the electronic structure. However, it is important to mention that we calculated electrostatic calculations for both models instead of $Na_{0.11}Li_{0.06}Mn_{0.94}O_2$ and $Na_{0.11}Li_{0.22}Mn_{0.78}O_2$.

5.3.3 Electronic structure calculations

Furthermore, the redox mechanism of $Na_xLi_yMn_{1-y}O_2$ were investigated to determine charge states of elements for further electrostatic analysis on phase transition, which will be discussed later. To achieve this aim, magnetic moments (represented as number of unpaired electrons (N_{unp})) on elements as well as spin density difference (SDD) plots (Fig. 5.4 and Fig. 5.5) were computed using DFT-HSE06. The calculated average value of unpaired electrons $(\overline{N_{\text{unp}}})$ on Mn in $Na_{0.67}MnO_2$ (Fig. 5.4) indicates that 36.11% of Mn exhibit a charge state of 3.8+ (($t_{2g}{}^3e_g{}^0$, $\overline{N_{\text{unp}}}$ = 3.24), and the rest have a charge state of 3.0+–3.3+, from which 44.44% are in the low spin ($t_{2g}{}^4e_g{}^0$, $\overline{N_{\text{unp}}}$ = 2.02), and 19.44% in high spin ($t_{2g}{}^3e_g{}^1$, $\overline{N_{\text{unp}}}$ = 3.70). With the desodiation of *x* = 0.67 to 0.11, Mn cations that had charge states between 3.0+

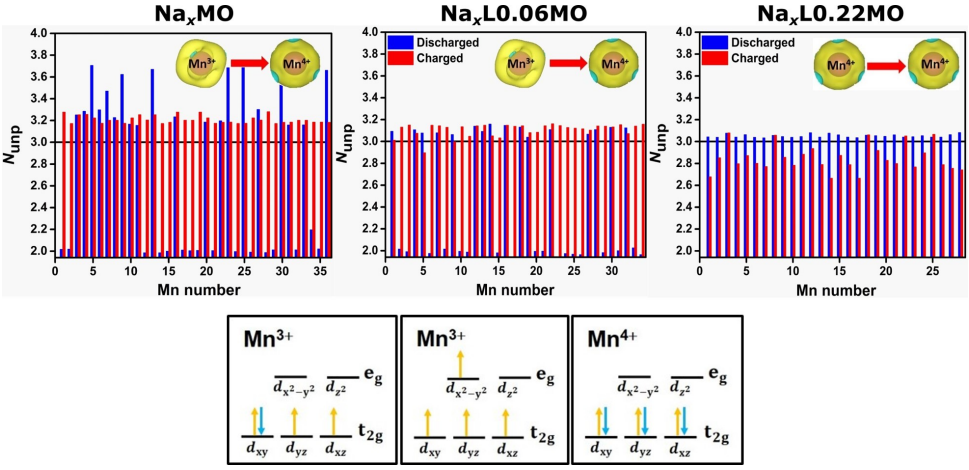

Figure 5.4: Calculated number of unpaired electrons N_{unp} on Mn in P2-Na_xMnO_2 (Na_xMO), P2-$Na_xLi_{0.06}Mn_{0.94}O_2$ (Na_xL0.06MO), and P2-$Na_xLi_{0.22}Mn_{0.78}O_2$ (Na_xL0.22MO) using DFT-HSE06.

and 3.3+ are oxidized and the average charge state of Mn cations becomes 3.8+ ($\overline{N_{\text{unp}}}$ = 3.21).

For $Na_{0.67}Li_{0.06}Mn_{0.94}O_2$, the computed $\overline{N_{\text{unp}}}$ for 53% of Mn ($t_{2g}{}^4e_g{}^0$, $\overline{N_{\text{unp}}}$ = 1.98, low spin) and 47% of Mn ($t_{2g}{}^3e_g{}^0$, $\overline{N_{\text{unp}}}$ = 3.10) indicates that Mn cations have an oxidation state of 3+ and 4+, respectively. After desodiation of *x* = 0.67 to 0.11, 53% of Mn cations that had an initial charge state of 3+ experiences oxidation and exhibits a charge state of 4+($\overline{N_{\text{unp}}}$ = 3.11), which can be clearly seen in the SDD plots (Fig. 5.5) where the Mn features shrink after desodiation. In comparison to the $Na_{0.67}MnO_2$ compound, the $Na_{0.67}Li_{0.06}Mn_{0.94}O_2$ system also shows a P2→O2 phase transition during charging of *x* = 0.67 to 0.11. The com-

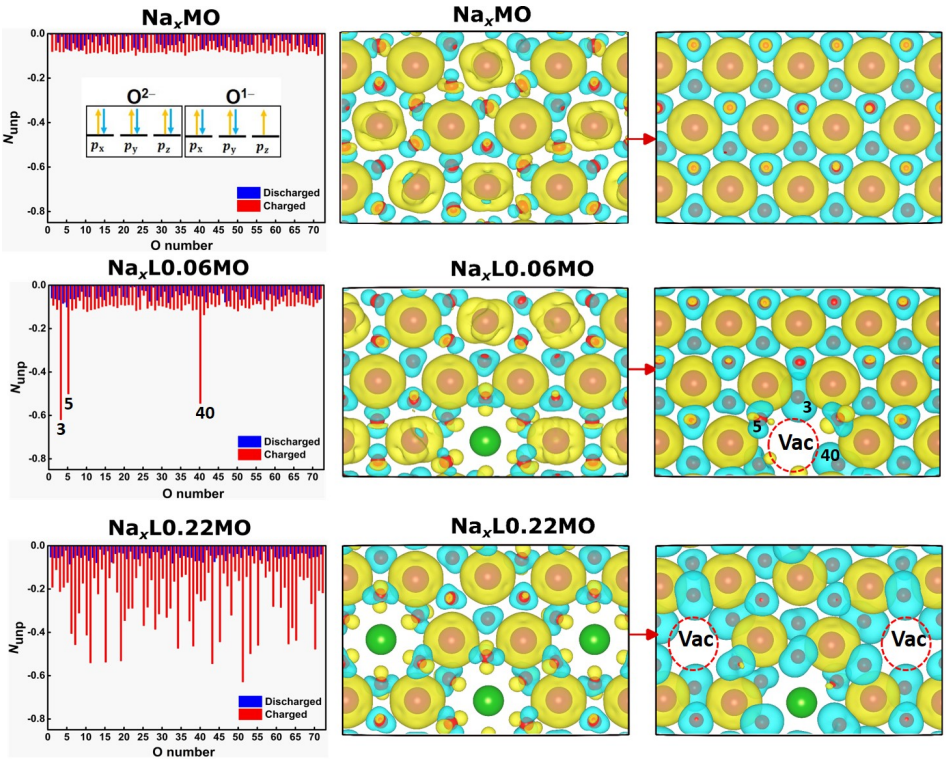

Figure 5.5: Calculated number of unpaired electrons (N_{unp}) of O ions (left figure) and Spin density difference (SDD) plots (with an isosurface of $0.006\text{eV}/\text{Å}^3$) of chosen O-TM-O layers of P2-Na_xMnO_2 (Na_xMO), P2-$Na_xLi_{0.06}Mn_{0.94}O_2$ (Na_xL0.06MO), and P2-$Na_xLi_{0.22}Mn_{0.78}O_2$ (Na_xL0.22MO) with **x** = 0.67 (middle figure) and *x* = 0.11 (right figure) using DFT-HSE06. Yellow and blue colors represent the up- and down-spin electrons respectively. The red arrow represents from discharged to charged state.

puted $\overline{N_{\text{unp}}}$ of all Mn cations is 3.05 for $Na_{0.67}Li_{0.22}Mn_{0.78}O_2$ indicating the oxidation state of Mn cations to be 4+ ($t_{2g}{}^3e_g{}^0$, $\overline{N_{\text{unp}}}$ = 3.05). This can also be seen in the SDD plot (Fig. 5.5) where small features exist on Mn. Upon desodiation from *x* = 0.67 → 0.11, the calculated $\overline{N_{\text{unp}}}$ for Mn remains almost the same, indicating an oxidation state of 4+. Compared to $Na_{0.67}MnO_2$, there is no phase transition from P2→O2 for the $Na_xLi_{0.22}Mn_{0.78}O_2$ (for *x* = 0.67→0.11) system as all of Mn shows an oxidation state of 4+ before and after desodiation. Therefore, it seems that this amount of Li acts as a structure stabilizer for $Na_{0.67}Li_{0.22}Mn_{0.78}O_2$ as well as $Na_{0.11}Li_{0.11}Mn_{0.78}O_2$. The calculated values of $\overline{N_{\text{unp}}}$ on O for Na_xMnO_2, $Na_xLi_{0.06}Mn_{0.94}O_2$, and $Na_xLi_{0.22}Mn_{0.78}O_2$ in the discharge state (*x* = 0.67) are equal to or smaller than -0.05 indicating that the average charge state on O is between 2- and 1.95- (Fig. 5.5). The small features on O anions in the SDD plot confirm that the charge state of O is close to 2- in the discharge state. Computed $\overline{N_{\text{unp}}}$ = -0.08 of O in Na_xMnO_2 for *x* = 0.11 shows only a small charging-induced oxidation of oxygen. Similarly, the O anions in $Na_{0.11}Li_{0.03}Mn_{0.94}O_2$ do not experience much oxidation as the calculated value of $\overline{N_{\text{unp}}}$ is -0.12. The oxidation of O in this composition is, however, slightly higher than $Na_{0.11}MnO_2$, which is because of Li for Mn substitution. In particular, some of O anions (e.g. O3, O5, and O40) close to the vacant site, which are created after Li migration, undergo the highest oxidations $\overline{N_{\text{unp}}}$ = -0.56. The larger blue feature on O3, O5, and O40 in the SDD plot of $Na_{0.11}Li_{0.03}Mn_{0.94}O_2$ compared to all O anions in $Na_{0.11}MnO_2$ (Fig. 5.5) visualize this result.

As we discussed earlier, Mn is inactive for $Na_{0.11}Li_{0.11}Mn_{0.78}O_2$, and, therefore, the ion that contributes to the redox mechanism is oxygen. This result is in agreement with previous DFT studies by De la Llave et al.[38] and Kim et al.[39] who studied P2-$Na_{0.6}Li_{0.2}Mn_{0.8}O_2$ and P2-$Na_{0.67}Li_{0.33}Mn_{0.67}O_2$, respectively, and found extra oxygen states appearing near the Fermi level (in the computed projected density of states) indicating an oxygen anion redox to compensate the charge imbalance. After desodiation of *x* = 0.67→0.11, higher N_{unp} ($\overline{N_{\text{unp}}}$ = -0.27) and larger SDD (more blue features) of O anions close to the vacant site (e.g. O6, O7, O10,

Table 5.2: Computed averaged number of unpaired electrons N_{unp} on cations and anions of studied cathode materials in their charged and discharged states using DFT-HSE06

System	Mn	O
$Na_{0.67}MnO_2$	$Mn_{16/36}$=2.02 $Mn_{7/36}$=3.70 $Mn_{13/36}$=3.24	-0.03
$Na_{0.11}MnO_2$	3.21	-0.08
$Na_{0.67}Li_{0.06}Mn_{0.94}O_2$	$Mn_{9/17}$=1.98 $Mn_{8/17}$=3.10	-0.05
$Na_{0.11}Li_{0.03}Mn_{0.94}O_2$	3.11	-0.12
$Na_{0.67}Li_{0.22}Mn_{0.78}O_2$	3.05	-0.05
$Na_{0.11}Li_{0.11}Mn_{0.78}O_2$	2.85	-0.27

O11) show that they experience strong oxidation. Higher oxygen redox activity in $Na_{0.11}Li_{0.11}Mn_{0.78}O_2$, as compared to $Na_{0.11}MnO_2$ and $Na_{0.11}Li_{0.03}Mn_{0.94}O_2$, is most likely due to the formation of more 8% TM vacancies in the crystal structure. This triggers oxygen redox reaction as the oxygen anions that have lost their binding to removed Li ions undergo significant oxidation ($\overline{N_{\text{unp}}}$ = -0.55). The sequence of oxygen redox activity in our studied systems from lower to higher is as follows: $Na_{0.11}MnO_2$→$Na_{0.11}Li_{0.03}Mn_{0.94}O_2$→$Na_{0.11}Li_{0.11}Mn_{0.78}O_2$. The electrostatic interaction between different cations as well as between them and the oxygen anions might explain the phase stability/transition.

5.3.4 Phase stability/transition

To study this, the differences in total electrostatic energies were calculated using Coulomb energy analysis by using elementary charge states, which balance the system, as well as by applying computed charge states from Fig. 5.4 and 5.5 between the P2 and O2 phases ΔE = $E_{\text{tot}}^{\text{P2}}$ - $E_{\text{tot}}^{\text{O2}}$ for $Na_xLi_yMn_{1-y}O_2$ with different Na (x = 0.67, 0.11) and Li (y = 0, 0.22) concentrations (Fig. 5.6). The P2 phase is found to be electrostatically more stable than the O2 counterpart for x = 0.67 in all com-

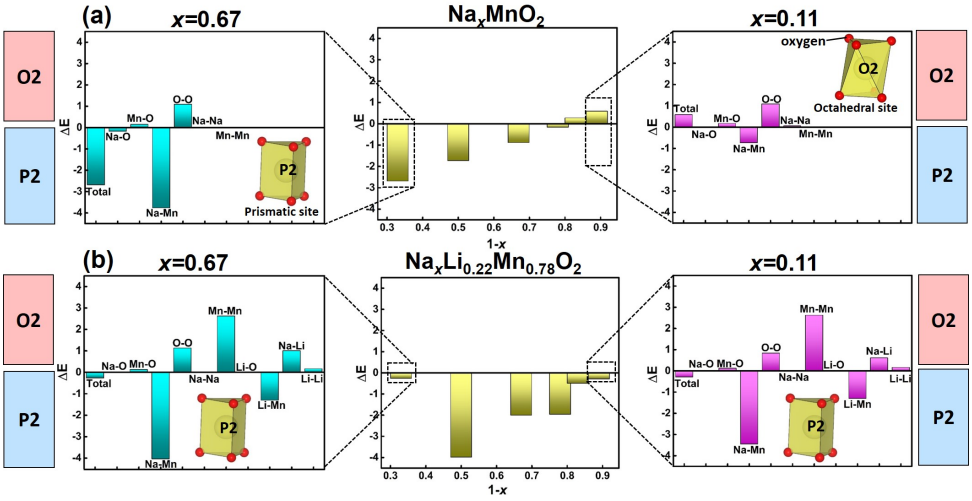

Figure 5.6: Computed ΔE which is the electrostatic energy difference for (a) $Na_{1-x}MnO_2$ (b) $Na_{1-x}Li_{0.22}Mn_{0.78}O_2$ between the P2 and O2 phase versus Na-concentration represented in yellow color. Aqua and Magenta color represents the discharged and charged state respectively that shows an individual contribution of each element in total electrostatic energy.

5

positions, namely $Na_{0.67}MnO_2$ and $Na_{0.67}Li_{0.22}Mn_{0.78}O_2$. This finding is in line with both our DFT results (Fig. 5.2) as well as experimental studies on $Na_{0.67}MnO_2$ and $Na_{0.67}Li_{0.22}Mn_{0.78}O_2$ by Delmas et al.[5] and Myung et al.[36] respectively. Our electrostatic calculation (Fig. 5.6) for low Na concentrations (charged state) shows that the O2 phase becomes more favorable in the case of Li free, namely $Na_{0.11}MnO_2$ and consistent with DFT calculations and with experimental studies by Delmas et al.[5] and Dahn et al.[11]. However, for the case of high concentrations of Li, namely $Na_{0.11}Li_{0.22}Mn_{0.78}O_2$, the P2 phase remains stable after desodiation, in agreement with DFT and experimental study by Myung et al.[36]. Furthermore, we analyzed the pairwise ion-ion interaction by computing their corresponding electrostatic energy differences between P2 and O2 phases for two compounds with the largest difference in Li and Na concentrations, namely $Na_{0.67}MnO_2$, $Na_{0.11}MnO_2$, $Na_{0.67}Li_{0.22}Mn_{0.78}O_2$, and $Na_{0.11}Li_{0.22}Mn_{0.78}O_2$ (Fig. 5.6). Moreover, we analyzed pair distribution function (pdf) of ions to determine the underlying mechanism for the phase stability and transition in these materials (Fig. 5.7 and Fig. 5.8). In all cases, the $O-O$ interaction favors the O2 phase, i.e E_{O-O} is lower for the O2 phase. This

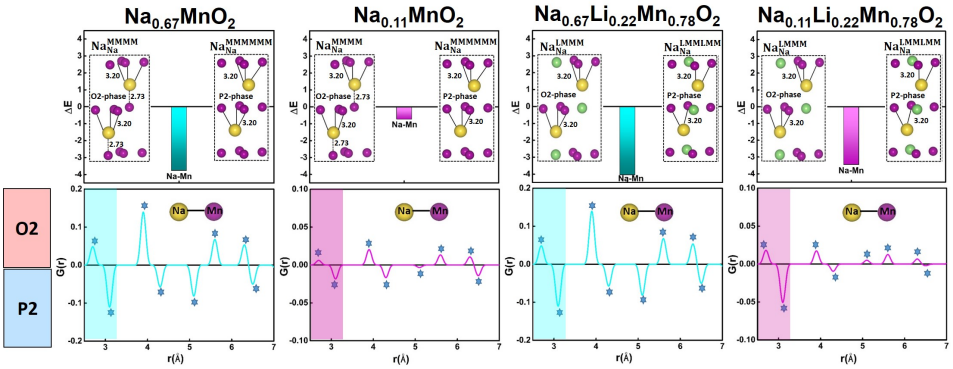

Figure 5.7: Calculated pair distribution function which is the difference of O-P ($G_O(r)$-$G_P(r)$ corresponding to atomic pairs of Na-Mn (b) Top view of the layer and bond length in Angstrom (Å) of (a) Na_xMnO_2 and (b) $Na_xLi_{0.22}Mn_{0.78}O_2$ (x = 0.11) during charging and shaded area represent the nearest neighbors.

5

is most likely due to the shorter distances ($r_{O\text{-}O}$) of nearest neighbors in P2: e.g. $r_{peak}(P2)$ = 3.40 Å < $r_{peak}(O2)$ = 3.80 Å and $r_{peak}(P2)$ = 4.40 Å < $r_{peak}(O2)$ = 4.84 Å. With desodiation, the values of ΔE_{O-O} remain unchanged for $Na_{0.11}MnO_2$ (Fig.5.8) because of the same oxidation state of O before and after desodiation.

However, the O−O interaction changes slightly for $Na_xLi_{0.22}Mn_{0.78}O_2$ (x = 0.11) after desodiation because of a very small oxidation of O (1.95- → 1.92-). The Cation−O interactions (cation: Mn, Na, and Li) do not stabilize significantly any of the P2 or O2 phases in both studied systems (ΔE_{cat-O} < 0.18 eV from Fig. 5.6). Although the Mn-Mn interaction does not stabilize any of these phases for Na_xMnO_2 as ΔE_{Mn-Mn} = 0.02 eV, it does prefer O2 phase over P2 phase (ΔE_{Mn-Mn} = 2.62 eV) for $Na_xLi_{0.22}Mn_{0.78}O_2$, which is probably due to the stronger interlayer Mn−Mn repulsion (as all of Mn become 4+) in the P2 phase after replacing partial Mn by Li cations. Figure 5.6 indicates that the Na-Mn interaction is the determining factor controlling the phase stability of the studied materials.

This can be due to the high charge of the Mn cations (from 3.34+ to 4+ depending on the Li and Na concentrations) as well as the distinct phase-dependent Na-Mn separations as discussed later. Since the other pairwise interactions do not change much with desodiation, we will focus on Na-Mn pairs. The Na-Mn interaction favors the P2 phase in all cases due to the shorter Na-Mn distances for the O2 phase.

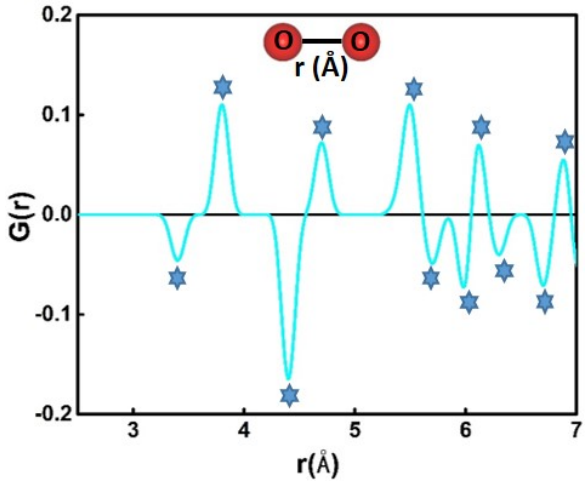

Figure 5.8: Calculated O-O pair distribution function difference between O and P ($G_O(r)$-$G_P(r)$ phases.

This can be clearly observed from the pdf plots in Fig. 5.7. The decrease in the phase stability of the P2 phase over the O2 phase after desodiation in the case of Na_xMnO_2 is probably because of oxidation of Mn from 3.34+ to 4+ (Fig. 5.4) as well as a decrease in the number of nearest neighbors Na-Mn pairs $r_{peak}(O2)$ = 2.73 Å and $r_{peak}(P2)$ = 3.20 Å. However, in the case of $Na_xLi_{0.22}Mn_{0.78}O_2$, the charge states of Mn cations do not change much. Moreover, the intensities of nearest neighbor Na-Mn pairs do not decrease significantly in contrast to the case for Na_xMnO_2. This is because Na ions prefer occupying the Na sites that are closest to the Li ions to reduce the Na^{+}-Mn^{4+} repulsion. Our DFT calculation shows that these Na sites (shown by Na_{Na}^{LMMM} and Na_{Na}^{LMMLMM} for the O2 and P2 phases, respectively, in Fig. 5.7) are much more favorable (by 2.82 eV) for Na occupation than the other Na sites that are next to Mn^{4+}(shown by Na_{Na}^{MMMM} and Na_{Na}^{MMMMMM} for the O2 and P2 phases, respectively, in Fig. 5.7). Therefore, they are the determining sites for the electrostatic energy difference between the P2 and O2 phases. For the aforementioned reasons, the phase stability of the P2 phase over the O2 phase does not change much after desodiation. The similar energy difference between P2 and O2 phases for high and low Na concentrations of the Li-doped case (in spite of their different PDF intensities of next nearest neighbors) confirm our assump-

tion that the interactions between the first nearest Na-Mn neighbors determine the phase stabilities.

As mentioned earlier, there is a Li migration from TM- to Na-sites for $Na_{0.11}Li_{0.06}Mn_{0.94}O_2$ and $Na_{0.11}Li_{0.22}Mn_{0.78}O_2$ structures. Probably, Li is not even stable in the octahedral Na sites due to its small size (compared to Na). Our previous theoretical/experimental study has shown that partially migrated Li to TM sites migrate further to the surface of electrode forming a CEI layer[36]. Therefore, we removed the Li-ions from the Na-sites and studied the phase transition. However, a similar result to the case without Li migration was found: the O2 phase is more favorable than the P2 phase in $Na_{0.11}Li_{0.03}Mn_{0.94}O_2$, while the P2 phase is more favorable than the O2 phase in $Na_{0.11}Li_{0.11}Mn_{0.78}O_2$. Moreover, in these models containing TM vacancies (due to Li migration), Na ions prefer to occupy Na sites next to a TM vacancy to lower the electrostatic energy. A mechanism, similar to $Na_{0.11}Li_{0.22}Mn_{0.78}O_2$ containing Li ions at TM sites, is expected for $Na_{0.11}Li_{0.11}Mn_{0.78}O_2$ containing TM vacancies (created by Li migration) to explain why the P2→O2 phase transition is prevented.

5.4 Conclusions

We investigated the origin behind the phase transition in the P2-$Na_{0.67}MnO_2$ cathode by performing DFT calculations and electrostatic energy analyses. We also simulated the effect of substitution of Mn by Li on the stability of P2-$Na_{0.67}MnO_2$. It is found that the Na-Mn interaction is the most determining factor controlling the phase stability of $Na_{0.67}MnO_2$, which is strongly Na concentration (x) dependent. This pairwise interaction prefers the P2 phase over the O2 phase independent of x value, but this preference weakens with decreasing x. The O-O interaction, which is the second most important parameter determining the phase stability, favours the O2 phase with a very weak Na concentration dependency. For the aforementioned reasons, the preference of the P2 phase due to the Na-Mn interaction becomes weaker than that of the O2 phase due to the O-O interaction leading to the P2→O2 phase transition in Na_xMnO_2 at low x values (e.g. x = 0.11). Decrease in the num-

ber of nearest neighbor Na-Mn pairs and the oxidation of $Mn^{3.34+}$ to Mn^{4+} after charging are probably responsible for the phase transition. We also explained the reason behind the suppression of the phase transition through the substitution of Mn by low-charge state elements such as Li. It was found that the 22% doping with Li retains the P2 phase during charging. The higher stability of the P2 phase as compared to O2-$Na_xLi_{0.11}Mn_{0.78}O_2$ even after desodiation (x = 0.67→0.11) is dictated by Na-Mn interaction, which is much weaker (more favorable) for Na absorption close to Li at TM sites for the P2 phase. This preference is determined mainly by nearest Na-Mn neighbours which does not change with Na concentration. This work not only quantitatively proves the phase preference in the as-synthesized and desodiated P2-Na_xMnO_2 and P2-$Na_xLi_{0.11}Mn_{0.78}O_2$but also the corresponding driving force behind the phase stabilities.

5.5 References

1. HS. Hirsh, Y. Li, DHS. Tan, M. Zhang, E. Zhao, YS. Meng, Advance Energy Material, 2020, 10, 2001274.
2. A. Rudola, R. Sayers, C.J. Wright, J. Barker, Nature Energy, 2023, 8, 215-218.
3. W. Zuo, A. Innocenti, M. Zarrabeitia, D. Bresser, Y. Yang, S. Passerini, Accounts of chemical research, 2023, 3, 284-296.
4. X. Liang, X. Song, H. Sun, H. Kim, M. C. Kim, Y.K. Sun, Nature Communications, 2025, 1, 3505.
5. A. Mendiboure, C. Delmas, P. Hagenmuller, Journal of Solid State Chemistry, 1985, 57, 323-331.
6. M. H. Han, E. Gonzalo, M. C. Cabanas, T. Rojo, Journal of Power Sources, 2014, 258, 266-271.
7. X. Ma, H. Chen, G. Ceder, Journal of Electrochemical Society, 2011, 12, 158, A1307.
8. N. Voronina, H. J. Kim, H. M. Shin, S.T. Myung, Journal of Power Sources, 2021, 514, 230581.
9. L. Zhang, T. Yuan, L. Soule, H. Sun, Y. Pang, J. Yang, S. Zheng, ACS Applied Energy Material, 2020, 3, 3770-3778.
10. N. Voronina, H. J. Kim, A. Konarov, N. Yaqoob, K.S. Lee, P. Kaghazchi, S.T. Myung, Advance Energy Material, 2021, 11, 2003399.
11. Z. Lu, J.R. Dahn, Journal of Electrochemical Society, 2001, 148, A1225.
12. A. Konarov, J.U. Choi, Z. Bakenov, S.T. Myung, 2018, 6, 8558-8567.
13. N. Yabuuchi, M. Kajiyama, J. Iwatate, H. Nishikawa, S. Hitomi, R. Okuyama, S. Komaba, Nature materials, 2012, 11, 512-517.
14. J.W. Somerville, A. Sobkowiak, N. Tapia-Ruiz, J. Billaud, J.G. Lozano, R.A. House, P.G. Bruce, Energy & Environmental Science, 2019, 12, 2223-2232.
15. N. Yabuuchi, R. Hara, M. Kajiyama, K. Kubota, T. Ishi-gaki, A. Hoshikawa, S. Komaba, Advance Energy Material, 2014, 4, 1301453.

16. L. Yang, L.Y. Kuo, J.M. López del Amo, P.K. Nayak, K. A. Mazzio, S. Maletti, D. Mikhailova, L. Giebeler, P. Kaghazchi, T. Rojo, P. Adelhelm, Advance functional Material, 2021, 31, 2102939.

17. A. Langella, A., Massaro, A.B. Muñoz-García, M. Pavone, ACS Energy Letters, 2025, 10, 1089-1098.

18. H. Jung, J. Kim, S. Kim, Journal of Applied Physics, 2022, 5, 132.

19. C. Wang, L. Liu, S. Zhao, Y. Liu, Y. Yang, H. Yu, ... & J.C hen, Nature communications, 2021, 1, 2256.

20. K. Okhotnikov, T. Charpentier, S. Cadars, Journal of cheminformatics, 2016, 8, 17.

21. S.P. Ong, W.D. Richards, A. Jain, G. Hautier, M. Kocher, S. Cholia, D. Gunter, V. L. Chevrier, K. A. Persson, G. Ceder, Computational Material Science, 2013, 68, 314-319.

22. P.E. Blöchl, Physical Review. B, 1994, 50, 17953.

23. G. Kresse, J. Furthmüller, Physical Review. B, 1996, 54, 11169.

24. J. P. Perdew, K. Burke, M. Ernzerhof, Physical Review Letter, 1996, 77, 3865.

25. S. Grimme, J. Antony, S. Ehrlich, H. Krieg, 2010, The Journal of Chemical Physics, 2010, 15, 132.

26. S.L. Dudarev, G.A. Botton, S.Y. Savrasov, C.J. Humphreys, and A.P. Sutton, Phys. Rev. B, 1998, 57, 1505.

27. S. Pakdel, T. Olsen, K.S. Thygesen, npj Computational Materials, 2025, 1, 18.

28. C. Franchini, R. Podloucky, J. Paier, M. Marsman, & G. Kresse, Physical Review B—Condensed Matter and Materials Physics, 2007, 19, 195128.

29. A. V. Kruka u, O.A. Vydrov, A.F. Izmaylov, G.E. Scuseria, The Journal of Chemical Physics, 2006, 22, 224106.

30. R. Ramprasad, H. Zhu, P. Rinke, M. Scheffler, Physical review letters, 2012, 6, 066404.

31. J. Paier, M. Marsman, K. Hummer, G. Kresse, I.C. Gerber, & J.G. Ángyán, The Journal of chemical physics, 2006, 15, 124.

32. J. Heyd, G.E. Scuseria, & M. Ernzerhof, The Journal of chemical physics, 2003, 18, 8207-8215.

33. M. Shishkin, M. Marsman, & G. Kresse, Physical review letters, 2007, 24, 246403.

34. K. Momma, F. Izumi, Journal of Applied crystallography, 2011, 44, 1272-1276.

35. X. Ma, H. Chen, G. Ceder, Journal of Electrochemical Society, 2011, 158, A1307.

36. N. Voronina, M.Y. Shin, H.J. Kim, N. Yaqoob, O. Guillon, S.H. Song, P. Kaghazchi, S.T. Myung, Advance Energy Material, 2022, 12, 2103939.

37. Q. Wang, S. Mariyappan, G. Rousse, A.V. Morozov, B. Porcheron, R. Dedryvère, J.M. Tarascon, Nature materials, 2021, 20, 353-361

38. E. de la Llave, E. Talaie, E. Levi, P. K. Nayak, M. Dixit, P.T. Rao, L.F. Nazar, Chemistry of Materials, 2016, 28, 9064-9076.

39. D. Kim, M. Cho, K. Cho, Advanced Materials, 2017, 29, 1701788.

A

Summary

Layered oxides have gained significant attention as promising cathode materials for both LIBs and SIBs. LIBs generally show better structural stability due to the smaller size of Li^+ and its stronger electrostatic interactions within the host lattice. In contrast, SIBs, although more prone to larger volume changes and structural instability due to the larger Na^+ radius, but offer a more sustainable and cost-effective alternative because of their high natural abundance and low cost of sodium.

They experience capacity fade due to structural and mechanical instability during the charging/discharging process. Identifying the origin of capacity fade and instability is essential for understanding material degradation. Therefore, in this thesis, the origin of the structural changes upon delithiation/lithiation and desodiation/sodiation has been investigated. These structural changes lead to a irreversible phase transition resulting in significant changes to lattice parameters, particularly along the *c*-axis, due to anisotropic expansion and contraction. These lattice changes generate internal mechanical stresses, leading to the formation of microcracks and capacity fading during cycling.

The impact of lattice doping on cathode materials for SIBs, with specific focus on Li, Mg, Co and Ni-doping in P2-$Na_{0.67}MnO_2$, is also explored. We also found the reason behind the phase stabilization (as-synthesized material) and transition (during operation) of P2-$Na_{0.67}MnO_2$ materials. The primary method used in this thesis is a combination of electrostatic analysis, density functional theory calculations as well as ab initio molecular dynamics simulation.

The fundamental cause behind the microcracking of $LiCoO_2$ (LCO) cathode is related to chapter 2. LCO is the most studied cathode material for LIBs. One of the main drawbacks of this system is its capacity fading due to the cracking of its microstructures during cycling. Initially, it is believed that this problem arises by the

delithiation/lithiation-induced changes in lattice parameters of primary particles in the microstructure. To our knowledge, a realistic combined atomistic and micro-scale simulation to prove this hypothesis was still lacking. Therefore, in this work, we modelled effect of delithiation/lithiation (charge/discharge) on the structural and mechanical properties of LCO on the atomistic- and micro-scale. It is found that the maximum arising lattice strain (during charging) in a typical LCO microstructure is smaller than +2%, which is the critical strain above which LCO experiences restructuring. Local lattice strain due to the space charge has also no significant effect on the atomistic structure. However, delithiation-induced oxygen vacancy formation leads to a large local lattice strain and thereby displacement of Li ions between O-Co-O layers. This is most likely the initial stage of microcracking in the LCO cathode.

In Chapter 3, the effect of doping on the structural stability of P2-Na_xMnO_2 cathodes materials was successfully studied. We successfully investigated the theoretical design of oxygen-redox-active cathode materials for SIBs, focused on challenges like structural instability and Li migration (which is one of the possible reasons for capacity fade in Na-based cathodes) during the charging/discharging process. We also found that the Li doping suppressed the phase transition from P2$\rightarrow$O2 during charging/discharging. DFT calculations revealed that co-doping of Li and Co/Ni on P2-type manganese-rich oxides e.g., $Na_{0.75}[Li_{0.156}Co_{0.156}Mn_{0.689}]O_2$ and $Na_{0.75}[Li_{0.14}Ni_{0.17}Mn_{0.69}]O_2$ enhances structural stability and redox mechanism which is an important parameter controlling capacity. Both cations and anions participated in the redox process, which might offer extra capacity. Overall, the study highlighted how electronic structure engineering and doping can enable stable cathodes for next-generation SIBs.

In chapter 4, theoretical investigation focused on structural stability of P2-type sodium-ion battery cathodes through strategic co-doping of Li, Mg, and Ni into the transition metal (TM) layer of P2-Na_xMnO_2 was successfully carried out. Using density functional theory (DFT) and ab initio molecular dynamics (AIMD), a systematic multi-level optimization approach was employed to evaluate structural stability and

redox behavior across a range of TM compositions: $Na_x[Li_xMg_{0.3-x-y}Ni_yMn_{0.7}]O_2$ (x, $y \leq 0.15$). Initial DFT calculations did not capture the realistic ion migrations at high charge states. Thus, AIMD simulations at elevated temperatures (300–800 K) were used to model the migration of Li and Mg ions from TM to Na layers, revealing significant reductions in system energy and stress, which are critical for structural stabilization. After AIMD simulations, again DFT calculations were performed to identified low-energy configurations that included favorable Li and Mg positions and oxygen dimer formations.

Among the other compositions, we found $Na_{0.7}[Li_{0.1}Mg_{0.05}Ni_{0.15}Mn_{0.7}]O_2$ to be most promising cathode, maintaining the P2 phase during deep desodiation without phase collapse or transition to the less stable O2 phase. The migration behavior of doping elements played a key role: Li showed a strong tendency to migrate, while Mg exhibited partial stability in TM layers, especially when vacancies were present due to Li migration. Manganese remained in the oxidation state of Mn^{4+}, while Ni not only provide full redox activity from Ni^{2+} / Ni^{4+} but also helps stabilize the TM layer structure, minimizing Li migration and oxygen loss. DFT calculations further showed that oxygen anions close to TM vacancies experienced more oxidation particularly through the formation of oxidized O anions (O_2^{n-}).

Chapter 5 presents the reason behind the phase stabilization and transition of P2-Na_xMnO_2 materials for SIBs. Previous experimental and computational studies proposed that the Jahn-Teller (J-T) distortion in $Mn^{3+}O_6$ is the driving force of phase transitions and structural instability in P2-Na_xMnO_2, during charging. In this work, we show that the driving force of desodiation-induced phase transition is the oxidation of Mn^{3+} to Mn^{4+} but not the change in J-T distortion. The latter is a short-range local intralayer phenomenon and cannot strongly affect the long-range interlayer interaction which determines the phase stability. This is proven by our electrostatic calculation for atomistic structures without any J-T distortion.

Our study further provides a quantitative explanation for the phase stability and transition of Na-based layered manganese oxide materials based on electrostatic forces for the first time.

Long-range Na-Mn and O-O interactions are found to be the most determining factors controlling the phase stability and transition of P2-Na_xMnO_2 and $Na_xLi_{0.22}Mn_{0.78}O_2$. Desodiation-induced weakening of Na-Mn interaction leads to the formation of O2-$Na_{0.11}MnO_2$, which is driven by O-O interaction. Decrease in the density of nearest neighbor Na-Mn pairs and the oxidation of $Mn^{3.34+}$ to Mn^{4+} after charging are responsible for the phase transition. We also explained that the reason of phase-transition suppression by substitution of Mn by Li is that Li at TM sites of P2-$Na_x[Li_{0.22}Mn_{0.78}]O_2$ can retain the P2 preference over O2 even after desodiation. This is because the presence of Li at TM sites decreases the dependence of Na-Mn interaction, which is the most important parameter stabilizing the P2 phase, on Na concentration. Overall, this study not only reproduces experimental results on the phase stability and transition in the prototype Mn-based layered oxide cathode material but also provides a quantitative explanation for this behaviour. We believe that our theoretical study provides important new understanding of stability of Na-based layered oxide materials.

B

Samenvatting

Gelaagde oxiden hebben veel aandacht gekregen als veelbelovende kathodematerialen voor zowel LIB's als SIB's. LIB's vertonen over het algemeen een betere structurele stabiliteit vanwege de kleinere omvang van Li^+ en de sterkere elektrostatische interacties binnen het gastrooster. SIB's daarentegen zijn weliswaar gevoeliger voor grotere volumeveranderingen en structurele instabiliteit vanwege de grotere straal van Na^+, maar bieden een duurzamer en kosteneffectiever alternatief vanwege de grote natuurlijke abundantie en lage kosten van natrium.

Ze ondervinden capaciteitsverlies als gevolg van structurele en mechanische instabiliteit tijdens het laad-/ontlaadproces. Het identificeren van de oorzaak van capaciteitsverlies en instabiliteit is essentieel voor het begrijpen van materiaaldegradatie. Daarom is in dit proefschrift de oorzaak van de structurele veranderingen bij delithiëring/lithiëring en desodiering/sodiering onderzocht. Deze structurele veranderingen leiden tot een onomkeerbare faseovergang, wat resulteert in aanzienlijke veranderingen in de roosterparameters, met name langs de *c*-as, als gevolg van anisotrope uitzetting en krimp. Deze roosterveranderingen genereren interne mechanische spanningen, wat leidt tot de vorming van microscheurtjes en capaciteitsverlies tijdens het cycleren.

De invloed van roosterdotering op kathodematerialen voor SIB's, met specifieke aandacht voor Li-, Mg-, Co- en Ni-dotering in P2-$Na_{0,67}MnO_2$, wordt ook onderzocht. We hebben ook de reden achter de fasestabilisatie (zoals gesynthetiseerd materiaal) en transitie (tijdens gebruik) van P2-$Na_{0,67}MnO_2$-materialen gevonden. De belangrijkste methode die in dit proefschrift wordt gebruikt, is een combinatie van elektrostatische analyse, berekeningen op basis van de dichtheidsfunctionaaltheorie en ab initio moleculaire dynamicasimulatie.

De fundamentele oorzaak van de microscheurtjes in de $LiCoO_2$ (LCO)-kathode

houdt verband met hoofdstuk 2. LCO is het meest bestudeerde kathodemateriaal voor LIB's. Een van de belangrijkste nadelen van dit systeem is het verlies aan capaciteit als gevolg van het barsten van de microstructuren tijdens het cyclisch laden en ontladen. Aanvankelijk werd aangenomen dat dit probleem ontstaat door de door delithiëring/lithiëring veroorzaakte veranderingen in de roosterparameters van primaire deeltjes in de microstructuur. Voor zover wij weten, ontbrak nog een realistische gecombineerde atomaire en microschaalsimulatie om deze hypothese te bewijzen. Daarom hebben we in dit werk het effect van delithiëring/lithiëring (laden/ontladen) op de structurele en mechanische eigenschappen van LCO op atomair en microschaal gemodelleerd. Er is vastgesteld dat de maximale roostervervorming (tijdens het laden) in een typische LCO-microstructuur kleiner is dan +2%, wat de kritische vervorming is waarboven LCO een herstructurering ondergaat. Lokale roostervervorming als gevolg van de ruimtelading heeft ook geen significant effect op de atomistische structuur. Delithiatie-geïnduceerde zuurstofvacaturevorming leidt echter tot een grote lokale roostervervorming en daarmee tot verplaatsing van Li-ionen tussen O-Co-O-lagen. Dit is hoogstwaarschijnlijk het beginstadium van microscheurtjes in de LCO-kathode.

In hoofdstuk 3 werd het effect van doping op de structurele stabiliteit van P2-Na_xMnO_2-kathodematerialen onderzocht. We hebben met succes het theoretische ontwerp onderzocht van zuurstof-redox-actieve kathodematerialen voor SIB's, waarbij we ons hebben gericht op uitdagingen zoals structurele instabiliteit en Li-migratie (een van de mogelijke oorzaken van capaciteitsverlies in Na-gebaseerde kathodes) tijdens het laad-/ontlaadproces. We hebben ook vastgesteld dat Li-doping de faseovergang van P2$\rightarrow$O2 tijdens het laden/ontladen onderdrukte. DFT-berekeningen hebben aangetoond dat co-dotering van Li en Co/Ni op P2-type mangaanrijke oxiden, bijvoorbeeld $Na_{0,75}[Li_{0,156}Co_{0,156}Mn_{0,689}]O_2$ en $Na_{0,75}[Li_{0,14}Ni_{0,17}Mn_{0,69}]O_2$ de structurele stabiliteit en het redoxmechanisme verbetert, wat een belangrijke parameter is voor het regelen van de capaciteit. Zowel kationen als anionen namen deel aan het redoxproces, wat extra capaciteit zou kunnen opleveren. Over het algemeen benadrukte de studie hoe elektronische

structuurtechniek en dotering stabiele kathodes voor de volgende generatie SIB's mogelijk kunnen maken.

In hoofdstuk 4 werd theoretisch onderzoek uitgevoerd naar de structurele stabiliteit van P2-type natrium-ionbatterijkathodes door middel van strategische co-dotering van Li, Mg en Ni in de overgangsmetaallaag (TM) van P2-Na_xMnO_2. Met behulp van dichtheidsfunctionaaltheorie (DFT) en ab initio moleculaire dynamica (AIMD) werd een systematische multi-level optimalisatiebenadering toegepast om de structurele stabiliteit en het redoxgedrag te evalueren voor een reeks TM-samenstellingen: $Na_x[Li_xMg_{0.3-x-y}Ni_yMn_{0.7}]O_2$ (x, $y \leq 0.15$). De eerste DFT-berekeningen gaven geen realistisch beeld van de ionenmigraties bij hoge ladingsniveaus. Daarom werden AIMD-simulaties bij verhoogde temperaturen (300–800 K) gebruikt om de migratie van Li- en Mg-ionen van TM- naar Na-lagen te modelleren, wat een aanzienlijke vermindering van de systeemenergie en -spanning aan het licht bracht, wat cruciaal is voor structurele stabilisatie. Na de AIMD-simulaties werden opnieuw DFT-berekeningen uitgevoerd om configuraties met lage energie te identificeren die gunstige Li- en Mg-posities en zuurstofdimeervormingen omvatten.

Van de andere samenstellingen bleek $Na_{0,7}[Li_{0,1}Mg_{0,05}Ni_{0,15}Mn_{0,7}]O_2$ de meest veelbelovende kathode te zijn, omdat deze tijdens diepe desodatie de P2-fase behield zonder fase-instorting of overgang naar de minder stabiele O2-fase. Het migratiegedrag van doteringelementen speelde een belangrijke rol: Li vertoonde een sterke neiging tot migratie, terwijl Mg gedeeltelijke stabiliteit vertoonde in TM-lagen, vooral wanneer er vacatures aanwezig waren als gevolg van Li-migratie. Mangaan bleef in de oxidatietoestand van Mn^{4+}, terwijl Ni niet alleen volledige redoxactiviteit biedt van Ni^{2+} / Ni^{4+}, maar ook helpt de TM-laagstructuur te stabiliseren, waardoor Li-migratie en zuurstofverlies tot een minimum worden beperkt. DFT-berekeningen toonden verder aan dat zuurstofanionen in de buurt van TM-vacatures meer oxidatie ondergingen, met name door de vorming van geoxideerde O-anionen (O_2^{n-}).

Hoofdstuk 5 presenteert de reden achter de fasestabilisatie en -overgang van P2-Na_xMnO_2-materialen voor SIB's. Eerdere experimentele en computationele studies

suggereerden dat de Jahn-Teller (J-T) vervorming in $Mn^{3+}O_6$ de drijvende kracht is achter faseovergangen en structurele instabiliteit in P2-Na_xMnO_2 tijdens het opladen. In dit werk laten we zien dat de drijvende kracht achter de door desodatie geïnduceerde faseovergang de oxidatie van Mn^{3+} tot Mn^{4+} is, en niet de verandering in J-T-vervorming. Dit laatste is een lokaal intralayer-fenomeen op korte afstand en kan geen sterke invloed uitoefenen op de interlayer-interactie op lange afstand, die bepalend is voor de fasestabiliteit. Dit wordt bewezen door onze elektrostatische berekening voor atomaire structuren zonder enige J-T-vervorming.

Onze studie biedt bovendien voor het eerst een kwantitatieve verklaring voor de fasestabiliteit en -overgang van op elektrostatische krachten gebaseerde gelaagde mangaanoxidematerialen op basis van natrium.

Langafstandsinteracties tussen Na-Mn en O-O blijken de meest bepalende factoren te zijn voor de fasestabiliteit en -overgang van P2-Na_xMnO_2 en $Na_xLi_{0.22}Mn_{0.78}O_2$. Door desodatie veroorzaakte verzwakking van de Na-Mn-interactie leidt tot de vorming van O2-$Na_{0,11}MnO_2$, wat wordt aangedreven door O-O-interactie. De afname van de dichtheid van de dichtstbijzijnde Na-Mn-paren en de oxidatie van $Mn^{3,34+}$ tot Mn^{4+} na het opladen zijn verantwoordelijk voor de faseovergang. We hebben ook uitgelegd dat de reden voor de onderdrukking van de faseovergang door substitutie van Mn door Li is dat Li op TM-plaatsen van P2-$Na_x[Li_{0,22}Mn_{0,78}]O_2$ de P2-voorkeur boven O2 kan behouden, zelfs na desodatie. Dit komt doordat de aanwezigheid van Li op TM-plaatsen de afhankelijkheid van de Na-Mn-interactie, de belangrijkste parameter voor het stabiliseren van de P2-fase, van de Na-concentratie vermindert. Over het geheel genomen reproduceert deze studie niet alleen de experimentele resultaten over de fasestabiliteit en -overgang in het prototype Mn-gebaseerde gelaagde oxidekathodemateriaal, maar biedt het ook een kwantitatieve verklaring voor dit gedrag. Wij zijn van mening dat onze theoretische studie nieuw inzicht biedt in de stabiliteit van Na-gebaseerde gelaagde oxidematerialen.

C

List of Publications

Published

First author:

- **N. Yaqoob**, M. Huijben, P. Kaghazchi*, On the origin of phase transition suppression of P2-$Na_{0.67}MnO_2$ by substitution of Mn with Li. (Manuscript submitted)

- **N. Yaqoob**, R. Mücke, O. Guillon, P. Kaghazchi, Delithiation-induced oxygen vacancy formation increases microcracking of $LiCoO_2$ cathodes, Journal of Power Sources, 2022, 533, 231316.

- M.J. Cho*, **N. Yaqoob***, J.H. Yu, K. Köster, A.Y. Kim, ... & P. Kaghazchi, S.T. Myung, Theoretical and experimental optimization of P2-type sodium-ion battery cathodes via Li, Mg, and Ni Co-doping: A path to enhanced capacity and stability, Advanced Energy Materials, 2025. 15, 2405112.

  M.J. Cho*, **N. Yaqoob*** contributed equally to this work.

Co-author:

- N. Voronina, **N. Yaqoob,** H.J. Kim, K.S. Lee, H.D. Lim, H.G. Jung, ... P. Kaghazchi & S.T. Myung, A new approach to stable cationic and anionic redox activity in O3-layered cathode for sodium-ion batteries, Advanced Energy Materials, 2021, 25, 2100901.

- R. Mücke, **N. Yaqoob,** M. Finsterbusch, F. Al-Jaljouli, P. Kaghazchi, D. Fattakhova-Rohlfing, & O. Guillon, Modelling electro-chemically induced stresses in all-solid-state batteries: screening electrolyte and cathode materials in composite cathodes. Journal of Materials Chemistry A, 2023, 35, 18801-18810.

- M. Hadouchi, **N. Yaqoob,** P. Kaghazchi, M. Tang, J. Liu, P. Sang,... & J. Ma, Fast sodium intercalation in Na3.41£0.59FeV(PO4) 3: a novel sodium-deficient NASICON cathode for sodium-ion batteries, Energy storage materials, 2021, 35, 192-202.

- J. Zheng, R. Xia, **N. Yaqoob,** P. Kaghazchi, J.E. Ten Elshof,.. & M. Huijben, Simultaneous enhancement of lithium transfer kinetics and structural stability in dual-phase Ti_2 electrodes by ruthenium doping, ACS Applied Materials & Interfaces, 2024, 7, 8616-8626.

- Y. Li, K.A. Mazzio, **N. Yaqoob,** Y. Sun, A.I. Freytag, D. Wong, ... P. Kaghazchi & P. Adelhelm, Competing Mechanisms Determine Oxygen Redox in Doped Ni–Mn Based Layered Oxides for Na□Ion Batteries, Advanced Materials, 2024, 18, 2309842.

- J.H. Yu, N. Voronina, **N. Yaqoob,** S. Kim, A.K. Paidi, D. Ahn, ... P. Kaghazchi & S.T. Myung, Migration of Mg in Na–O–Mg configuration for oxygen redox of sodium cathode, ACS Energy Letters, 2023, 1, 145-152.

- J.H. Jo, H.J. Kim, **N. Yaqoob,** K. Ihm, O. Guillon, K.S. Sohn, ... P. Kaghazchi & S.T. Myung, Hollandite-type potassium titanium oxide with exceptionally stable cycling performance as a new cathode material for potassium-ion batteries, Energy storage materials, 2023, 54, 680-688.

- H.J. Kim, J. Ahn, N. Voronina, **N. Yaqoob,** M. Bokdam, J. Jeong, ... P. Kaghazchi & S.T. Myung, Impact of water on structure stabilization in layered manganese-oxide for high-voltage zinc storage in non-aqueous electrolyte:

Experimental and theoretical aspects, Energy Storage Materials, 2023, 63, 103028.

- J. Zheng, R. Xia, C. Sun, **N. Yaqoob,** Q. Qiu, L. Zhong, ... & M. Huijben, Fast and durable lithium storage enabled by tuning entropy in wadsley–roth phase titanium niobium oxides, Small, 2023, 30, 2301967.

- N. Voronina, J.H. Yu, H.J. Kim, **N. Yaqoob,** O. Guillon, H. Kim, ... P. Kaghazchi & S.T. Myung, Engineering transition metal layers for long lasting anionic redox in layered sodium manganese oxide, Advanced Functional Materials, 2023, 5, 2210423.

- N. Voronina, M.Y. Shin, H.J. Kim, **N. Yaqoob**, O. Guillon, S.H. Song, ... P. Kaghazchi, & S.T. Myung, Hysteresis-suppressed reversible oxygen-redox cathodes for sodium-ion batteries, Advanced energy materials, 2022, 21, 2103939.

- N. Voronina, H.J. Kim, A. Konarov, **N. Yaqoob,** K.S. Lee, P. Kaghazchi, ... & S.T. Myung, Electronic Structure Engineering of Honeycomb Layered Cathode Material for Sodium-Ion Batteries. Advanced energy materials, 2021, 14, 2003399.

- C.H. Jo, N. Voronina, H.J. Kim, H. Yashiro, **N. Yaqoob,** O. Guillon, P. Kaghazchi, & S.T. Myung, Bio-Derived Surface Layer Suitable for Long Term Cycling Ni-Rich Cathode for Lithium-Ion Batteries, Small, 2021, 47, 2104532.

- F. Al-Jaljouli, R. Mücke, C. Roitzheim, Y.J. Sohn, **N. Yaqoob,** M. Finsterbusch, P. Kaghazchi & O. Guillon, Chemo-Thermal Stress in All-Solid-State Batteries: Impact of Cathode Active Materials and Microstructure, Journal of Power Sources, 2025, 237136.

- M. Zhang, L. Zhao, J. Xie, Q. Zhang, X. Wang, **N. Yaqoob,**... & J. Xing, Molecular engineering towards efficientwhite-light-emitting perovskite, Nature Communications, 2021, 1, 4890.

Master's Publication:

- **N. Yaqoob,** B. Sabir, G. Murtaza, R.M.A. Khalil, N. Muhammad, & A. Laref, Structural, electronic, magnetic, optical and thermoelectric response of half-metallic $AMnTe_2$ (A= Li, Na, K): an ab-initio calculations, Physica B: Condensed Matter, 2019, 574, 311656.

- **N. Yaqoob**, G. Murtaza, M.W. Iqbal, N.A. Noor, A. Mahmood, S.M. Ramay, ... & N.Y. Al-Garadi, Study of half metallic nature and transport properties of $XMnSe_2$ (X= Ca, Sr and Ba) compounds via ab-initio calculations, Journal of Materials Research and Technology, 2020, 5, 10511-10519.

- A. Wahab, B. Sabir, N.A. Kattan, **N. Yaqoob,** E. Algrafy, G. Murtaza, ... & I. Jamil, Ab initio study of electronic, optical and thermoelectric character of intermetallic compounds XGa_3 (X= Fe, Ru, Os), Optical and Quantum Electronics, 2020, 52, 1-15.

D

Acknowledgments

Reaching the end of my PhD has been both challenging and rewarding. This journey came with many ups and downs, and I would never have made it through without the help of many wonderful people. I'm truly grateful to all of you. I would like to begin by thanking my supervisor, **Prof. Dr. Payam Kaghazchi**, for giving me the opportunity to work on these interesting topics and for your constant encouragement and thoughtful guidance. Your belief in my work and your advice at key moments gave me the confidence to keep moving forward. I also want to thank my co-supervisor, **Prof. Dr. Mark Huijben**, for his willingness to be my second supervisor, for reviewing the thesis, for your honest feedback, and helpful suggestions.

I am grateful to **Prof. Dr. Seung-Taek Myung** and his research group at Sejong University in Seoul for their experimental expertise and collaboration. I would like to thank other Collaborators, especially **Prof. Dr. Philipp Adelhelm, Prof. Dr. Mark Huijben, Prof. Dr. Menno Bokdam**, and their group members, for their collaboration. In addition, I want to acknowledge **Melissa**—your past work on cathode materials helped shape my ideas in important ways. I appreciate your help in the beginning of my PhD.

To my officemates at IMD-2 Forschungzentrum Jülich, especially **Deema Abubaker, Konstantin Koster**, **Lars Winkler** and **Millica** for their nice working environment in the office. In addition, I want to thanks all my colleagues in IMD-2 Forschungszentrum Jülich, especially all the members in the **modelling group**. I am also grateful to **Dr. Tuba Iftikhar** and **Dr. Sidra Sarwar** for their help and encouragement, especially when I moved to Germany.

Finally, I would like to dedicate my work with love to my family, especially **my parents, husband** and my **son**. To my **parents**, thank you for your love and the sacrifices you made so I could reach this goal. I'll always be thankful for everything

you've done, and without your support, I would never have enjoyed so many opportunities. Though my **father** is no longer here to witness this moment, his unwavering belief in me continues to guide and inspire every step I take. To my husband, **Abdul Ahad**, your patience, care, and support during the tough times helped me more than words can say. To my son, **Muhammad Ibrahim Ahad**, who was born near the end of this PhD journey, your arrival brought me new strength and motivation to finish this work.

Band / Volume 667
Reactive Field Assisted Sintering of Novel Rare Earth Garnets for Plasma Etching Applications
C. Stern (2025), VII, 101, XXVIII pp
ISBN: 978-3-95806-833-9

Band / Volume 668
Effects of mucilage and extracellular polymeric substances on soil gas diffusion
A. Haupenthal (2025), v, 99 pp
ISBN: 978-3-95806-834-6

Band / Volume 669
Quantifying Recombination Losses and Charge Extraction in Halide Perovskite Solar Cells
L. Krückemeier (2025), vi, 286 pp
ISBN: 978-3-95806-835-3

Band / Volume 670
Investigation of Dynamic Material Changes During the Preparation of ZnPd Nanoparticles Supported on ZnO and their Catalytic Application in Methanol Steam Reforming on the Atomic Level
A. Meise (2025), xviii, 175 pp
ISBN: 978-3-95806-838-4

Band / Volume 671
Improving Energy Efficiency of Public Buildings by Influencing Occupant Behaviour using Dashboards and Gamification
E. Ubachukwu (2025), xxi, 191 pp
ISBN: 978-3-95806-840-7

Band / Volume 672
Exploring Plant Responses to Changing Environments: Integrating Phenotyping and Modeling Across Scales
F. M. Bauer (2025), xxix, 188 pp
ISBN: 978-3-95806-845-2

Band / Volume 673
A constitutive theory to represent non-idealities in contacting of SOC interconnect contacts
R. M. Pinto (2025), xii, 139 pp
ISBN: 978-3-95806-846-9

Band / Volume 674
Strontium titanate based materials for use as oxygen transport membranes in membrane reactors
Y. Tang (2025), XIV, 132 pp
ISBN: 978-3-95806-849-0

Band / Volume 675
Scaling Methods for the Production of Tungsten Fiber-Reinforced Composites via Chemical Vapor Deposition
A. Lau (2025), untersch. Pag.
ISBN: 978-3-95806-851-3

Band / Volume 676
Nanoscale analysis of high-temperature oxidation mechanisms of Cr_2AlC MAX phase and W-Cr-Y self-passivating tungsten alloy
A.J. S. Reuban (2025), ix, 142 pp
ISBN: 978-3-95806-855-1

Band / Volume 677
First principles simulations of high-entropy materials for energy storage
Y. Ting (2025), xviii, 169 pp
ISBN: 978-3-95806-858-2

Band / Volume 678
Deployment of Fuel Cell Vehicles in Road Transport and the Expansion of the Hydrogen Refueling Station Network
T. Grube, M. Sander (2025), iv, 61 pp
ISBN: 978-3-95806-859-9

Band / Volume 679
Entwicklung von nickelbasierten katalysatorbeschichteten Diaphragmen für die alkalische Wasserelektrolyse
C. B. Karacan (2025), 146 pp
ISBN: 978-3-95806-860-5

Band / Volume 680
Bewertung lokaler Eigenspannungsverteilungen bei der lokalen Bauteilreparatur durch Kaltgasspritzen
J.-C. Schmitt (2025), 154, xxvii pp
ISBN: 978-3-95806-861-2

Band / Volume 681
First principles study of the effect of substitution\doping on the performance of layered oxide cathode materials for secondary batteries
N. Yaqoob (2025), iii, 126 pp
ISBN: 978-3-95806-864-3

Energie & Umwelt / Energy & Environment
Band / Volume 681
ISBN 978-3-95806-864-3

Mitglied der Helmholtz-Gemeinschaft

JÜLICH
Forschungszentrum